On Multivariate Overlapping Grid Spectral Quasilinearization Methods for Problems in Cavity Flow

A DISSERTATION SUBMITTED TO THE UNIVERSITY OF KWAZULU-NATAL

FOR MASTER OF SCIENCE
IN THE COLLEGE OF AGRICULTURE, ENGINEERING AND SCIENCE

School of Mathematics, Statistics and Computer Science

by

Sibonelo Nzama

July 2022

Contents

Abstract

We investigate fluid flow in cavities with different boundary conditions. Three cavity flow problems of varying complexity are investigated in this study. In the first problem, a flow filled with a porous medium, and with adiabatic and impermeable walls is considered. The left wall is heated. For the second problem, we investigate free convection in an enclosed square with porous medium and nanofluid. We assume that the side walls have a high fixed temperature and a lower fixed temperature for the horizontal walls. The third problem is more complex, and it involves investigating a square enclosure with porous medium, a top moving wall, and the side walls heated with a sinusoidally varying temperature. We analyze the effect of fluid parameters on the fluid flow characteristics such as the streamline distribution, isoconcentration, isotherms, local Nusselt number, skin friction, and the local Sherwood number. The flow equations are solved using two recent numerical techniques, namely the multivariate overlapping grid spectral quasilinearization method (MOGSQLM) and the multivariate spectral quasilinearization method (MSQLM). The MOGSQLM is an extension of the MSQLM with improved accuracy. Using the two methods we determine the solution, the residual solution errors and the computational time to achieve a converged solution. The MOGSQLM is found to be more accurate, and for this reason, only the MOGSQLM is used to numerically solve the third problem. The MOGSQLM was found to be the better method in terms of convergence, accuracy, and CPU time. The changes in the Rayleigh number alter the flow pattern from circular to elliptic with stronger circulation in the core region.

Declaration-Plagiarism

This work was carried out at the University of KwaZulu-Natal, Pietermaritzburg campus, School of Mathematics, Statistics, and Computer Science under the supervision of Professor P. Sibanda and Doctor S.P. Goqo from February 2020 to July 2022.

I, Sibonelo Nzama declare that except where indicated, the work reported in this dissertation, represents my original research work. This dissertation was not submitted as part of any university qualification or examination. Unless otherwise noted, this dissertation contains no other person's graphs, data, pictures, or other information. Unless otherwise noted, this dissertation contains no other person's pictures, graphs, data, or other information. Unless specifically stated, this dissertation contains no other person's writing unless it is sourced from other researchers. When other written sources were quoted, their words were rephrased, but they were referred to by the general information attributed to them; and where exact words from outher/s used, their writing was enclosed in quotation marks and fully referenced. No copied and pasted text, tables, or graphics from the internet unless proper attribution is given and the source is detailed in this dissertation and the References section.

signature: ████ _____ Date: 11 September 2022 _____

Mr S. Nzama

signature: ███████ _____ Date: 11-Sept-2022 _____

Prof. P. Sibanda

signature: █████ _____ Date: 13/09/2022 _____

Dr S.P. Goqo

Acknowledgements

I thank the almighty God for the strength to complete this qualification. I acknowledge my late mother, my late grandfather and my family who raised and supported me in very difficult times. I cannot single out the role each person played in raising me to be who I am today but they all have a very special place in my heart. I thank every prayer for me, it gave me strength and helped me persevere in difficult circumstances. The kind lecturers at the University of KwaZulu-Natal, especially my supervisors Prof. P Sibanda and Dr S.P. Goqo. The support they gave was more than supervision, because most of the time I used their funding for my postgraduate studies. Without them I would not have completed this qualification. They always gave useful advice even though they make me sweat. I would not turn a blind eye to the kindness given by the UKZN applied mathematics postgraduates especially Dr S.D. Oluniiju, the help and ideas they provided. Lastly a special thanks Mrs Dimakatso Moloi; without this kind woman I would not even have my first qualification. When we exhausted possibilities to get my registration fee this kind lady decided to take it out of her pocket. I choose to limit my list here, not that I did not notice the important roles other people played in my life or in my studies, but the list would be to long. As the saying goes "it takes a community to raise a child". I believe everyone I met played an important role in my life and studies.

Dedication

I dedicate this dissertation to my family, friends, and everyone who knows me, and everyone who has a Nzama DNA in their blood. I also specially dedicate this dissertation to every teacher who once stood in front of me, especially Makhapha Combined School teachers, and more particularly Mr E.M Khumalo, Mr M.B.K. Mdletshe, Ms Z.D Gumede, Mr L.S Msani, Mr E.T Busani, the late Mr S Shange, Mr L Dludla and Ms T.R Mdladla.

List of Figures

List of Tables

Chapter 1

Introduction

In this work, we study the flow, heat, and mass transport in cavities with various boundary conditions. The effect of parameters such as the Hartmann number, Brownian motion parameter, chemical reaction parameter, thermophoresis, Eckert number, radiation parameter, Lewis number, and Rayleigh number on the flow structure, is investigated. In terms of numerical accuracy, convergence, and ease of application, we investigate the performance of recent spectral quasilinearization methods in finding numerical solutions to the equations that model cavity flows. We examine the convergence properties and accuracy of the methods using residual and iterative error norm errors.

1.1 Cavity flow

The study of cavity flows has its origins in the sixteenth century in the work of the Bernoulli brothers [1]. The Bernoullis first proposed the relationship between pressure and velocity in a fluid. Later, Euler worked on related problems and his work suggested that liquids moving at high velocity are subjected to stresses that could lead to the formation of cavities. This led to the formulation of the well-known Bernoulli relationship, which, in reality, was first derived by Euler [1]. In the nineteenth century experimental studies provided proof of formation of cavities at low air pressure [1, 2, 3]. Subsequently, cavitation has been investigated in different flow geometries, shapes and subject to different fluid and surface properties [4].

In the early years, experts in the field did not have a standard definition of cavitation. The question of what cavitation is remained unresolved for decades. The current understanding is that cavitation arises when the pressure at any location in the fluid system is below the pressure that may vaporise the liquid at the standard operating temperature [3, 5]. A simpler and more precise definition is that cavitation occurs due to sudden changes in the operating pressure leading to the formation of bubbles in a liquid [3]. Cavitation leads to two-phase flow, composed of a liquid and its vapour. Reynolds was among the first to formally study cavitation [1, 6]. There are four types of cavitation, namely, bubble cavitation, attached cavity, vortex cavitation and shear cavitation [4].

Cavity flow may arise in a fluid contained between plates when one or more of the plates is impulsively moved. A special case of cavity flow is where there is only one moving wall, which is lid-driven cavity flow [7]. A lid-driven cavity is traditionally used to model confined shear-driven flow [8]. Systems that generate cavity flow are of great scientific interest as cavities arise in many fluid mechanical flows such as corner eddies, rotating vortices, turbulent flows, etc. Industrial applications where cavity flow is relevant include the coating of materials, and in melt spinning processes used for manufacturing micro-crystalline materials [9]. An important area of study is the study of heat and mass transport in cavities. The flow behaviour, heat and mass transfer coefficients are strongly influenced by the Eckert, Lewis, and Rayleigh numbers [7].

From the 1960s, many studies on cavity flows focussed on the characteristics of two-dimensional cavity flows. The Reynolds number's effect on the size of the principal vortex and the development of secondary eddies have been studied extensively in the literature [10]. Even though cavity flow is one of the most widely studied problems, there are still gaps in our understanding of the physical nature of the flow. For example, it is not well understood if such flows are steady, turbulent or periodic in time. Additionally, it is not a settled question whether the flow is two or three dimensional, the mechanisms for transition from steady to unsteady flow are not known, etc. [11]. Although the cavity flow problem appears simple, it retains all the features of complex physics where counter-rotating vortices appear at the corners of the cavity [11]. In numerical computations, the lid-driven cavity flow is regarded as one of the standard problems for testing numerical algorithms, their accuracy, efficiency and stability. The studies on driven cavity flow can be grouped into three categories. The first category is where the steady-state is studied, the second is when the bifurcation regime from steady to unsteady is investigated, and the third is the study of the transition from steady to unsteady flow [11].

The driven cavity flow has eddy structures whose understanding is important in diverse applications such as in drag-reducing riblets and in mixing flows used to synthesize fine polymeric composites. Driven cavity flow offers an ideal framework where meaningful and detailed comparisons can be made between experimental, theoretical and computational studies. In addition, for cavity flows, an increase in the Reynolds number does not affect the domain of the flow. This allows for the investigation of the flow for a wide range of Reynolds numbers. Another advantage of the driven cavity flow is that it encapsulates almost every motion that can occur in incompressible flows including eddies, secondary flow, complex three-dimensional patterns, chaotic particle motion, instabilities, transition, and turbulence [9].

1.2 Important fluid parameters

A number of parameters in fluid flow aid in determining the nature and structure of the flow, as well as heat and mass transfer characteristics. We provide an overview of some key parameters raised in this study. The Hartmann, Grashof, Prandtl, Rayleigh, Lewis numbers, and others are important parameters. The Hartmann number H_a is a dimensionless number named after Julius Hartmann, who introduced it in his study of velocity and current density distributions in a fully developed flow of an electrically conducting fluid between two parallel solid walls [12, 13]. The Hartmann number quantifies

the importance of drag forces ranging from electromagnetic to viscous. The effect of increasing the Hartmann number is to reduce fluid movement. The Hartmann number [13, 14] influences streamlines, velocities, and heat transfer. The Grashof number is a dimensionless number that occurs as a result of natural convection motion. The Grashof number compares buoyancy to the viscous force acting on a fluid [15]. The relationship of momentum diffusivity divided by the thermal diffusivity is denoted by the Prandtl number. This can be physically interpreted as the efficiency with which momentum and energy are transferred by velocity diffusion and thermal boundary layers, respectively [15]. The Richardson number is a dimensionless fluid dynamics parameter used to calculate the relationship between the buoyancy term and the flow shear term [16].

The Rayleigh number R_a can be calculated by multiplying the Grashof and the Prandtl numbers. It is the product of the buoyancy and viscous forces, momentum and thermal diffuseness ratios [13]. The Lewis number L_e is a non-dimensional fluid dynamic number that characterizes flow with simultaneous heat and mass transfer. It is the product of thermal and mass diffusivity. The Lewis number can be thought of as a measure of the thermal and concentration boundary-layer thicknesses [13]. The Eckert number E_c is a non-dimensional fluid dynamic number that measures the kinetic energy of the flow in relation to the enthalpy difference across the thermal boundary-layer. It is important in high-speed flow, where viscous dissipation is significant [17, 18]. The buoyancy ratio parameter N_r is a non-dimensional constant that predicts the resistance of the lower compositionally dense but hot layer to mixing while being unaffected by system behavior. It describes the dynamics of thermochemical convection in the Earth's mantle [19, 20]. The Schmidt number is a dimensionless parameter that measures the effectiveness of momentum and mass transfer in the velocity and concentration boundary layers, respectively [15].

1.3 Heat and mass transfer in cavity flows

Heat and mass transfer in fluids occurs via convection, conduction, and thermal radiation. Many studies have been conducted to investigate convection in cavity flows, and we provide a brief review of some recent relevant studies. Sivasankaran and Kandaswamy [21] conducted research on double-diffusion convective, heat, and mass transfer in a water saturated porous cavity. The fluid in the cavity had a nonlinear density-temperature relationship, and the temperature of two walls was kept constant. The right vertical wall was cooled while the left vertical wall was heated. The Gauss-Seidel and successive over relaxation methods were used to solve the governing equations. They came to the conclusion that high porosity resulted in high heat and mass transfer rates. The Darcy number increased, as did the rates of heat and mass transfer.

Garoosi et al. [22] investigated heat and mass transfer in a differentially heated cavity using natural and mixed convection flow. This was one of the first studies to investigate heat and mass transfer in a square cavity filled with nanoparticles using thermophoresis and Brownian diffusion at the same time. In the study, the flow equations were solved using the finite volume method on a staggered grid. For natural convection, particle diameter affected the heat transfer rate; for example, reducing the diameter

size from 145 nm to 85 nm kept the rate constant, whereas reducing the diameter size from 58 nm to 25 nm increased the rate. When the Rayleigh number was increased and the diameter of the nanoparticles was reduced, the rate of heat transfer increased. The rate of heat transfer for mixed convection was increased by increasing the Grashof number while decreasing the Richardson number. Increasing the nanoparticle concentration increased the heat transfer rate regardless of the Richardson number for a Grashof number $G_r = 104$. For each Richardson number R_i value, the particle distribution was mostly uniform for $G_r \geq 10^4$.

Sheremet et al. [23] investigated free convection, heat, and mass transfer in a porous square cavity filled with a nanofluid. The left vertical wall was heated, while the right vertical wall was cooled at a height-dependent temperature. The Navier-Stokes equations were solved using the finite difference method with appropriate boundary conditions. Only the Rayleigh number increased the average Nusselt number and the intensity of the convective flow. The increase in the thermal stratification parameter reduced the vortex core sizes, displacement of the core close to the lower left corner, and rotation of this vortex along the horizontal axis.

Ghalambaz et al. [24] used the Garlerkin finite element scheme to solve the flow equations to study natural convection, heat, and mass transfer in a cavity flow. The researchers wanted to know how viscous dissipation and heat radiation affect heat and mass transfer in a heated square cavity filled with a nanofluid. They concluded that viscous dissipation has a significant impact on the concentration distribution of nanoparticles. The temperature gradient is reduced while heat diffusion is increased due to viscous dissipation. It was also discovered that viscous dissipation raises the average Nusselt number, which boosts heat transfer. The buoyancy ratio parameter and the Lewis number lowered and raised and the average Nusselt number, respectively.

Khadiri et al. [25] investigated the cavity flow problem with double-diffusive convection. The study looked at how the Soret parameter and buoyancy ratio affected solutions obtained through pure thermal convection. The cavity's bottom and top walls were heated and cooled in turn. The governing equations were numerically solved by combining the central finite-difference method with the alternate direction implicit method. They discovered that the Soret effect may have an impact on the onset of the oscillatory instability regime.

Kadri et al. [26] investigated the effect of a vertical magnetic field on a square cavity filled with nanofluid. The effect of the Hartmann number on streamlines, isotherms, and heat transfer in a cavity with heated and cooled bottom and top walls was investigated. The finite element method was used to solve the equations numerically. Heat transfer in nanofluids increased as the Hartmann number and magnetic field orientation were optimized.

Karimi-Fard et al. [27] looked at how the Prandtl, Schmidt, and Lewis numbers affected a double-diffusive convection in square enclosure filled with porous media. The emphasis was on an enclosure with vertical right and left walls that were heated and cooled at constant temperatures. The control volume method was used to solve the governing equations. The study found that the Darcy number increases heat and mass transport rates while the inertial parameter decreases the Nusselt and Sherwood

numbers. When dealing with double-diffusive natural convection, inertial effects are negligible. For non-Darcian flows with high Prandtl and Schmidt numbers, boundary effects are significant. Heat transfer was at its maximum for a critical value of the Schmidt number and a given value of the Prandtl number.

Bhuvaneswari et al. [28] investigated flow in an enclosure filled with a nanofluid and a linear height dependent temperature. The goal was to see how different effective viscosity and thermal conductivity models affected heat and mass transfer. The left vertical wall was heated, while the right vertical wall was cooled. The equations were solved numerically, using the control volume method. Two of the models studied showed an increase in heat transfer rate with increasing nanoparticle concentration, while one model showed a decrease in heat transfer rate. The increase in the Rayleigh number increased the heat transfer rate for all viscosity and thermal conductivity models.

Kandaswamy et al. [29] investigated the cavity flow problem using the Brinkmann-Forcheimer extended Darcy model and a linearly varying wall temperature instead of the most commonly used Darcy flow model with uniform heating. The Gauss-Seidel method was used to numerically solve the equations .

Sheremet et al. [30] investigated the square cavity flow problem with sinusoidally heated and cooled vertical left and right walls. Natural convection, entropy generation and water-based nanofluid were investigated in a square enclosure using the finite difference method. Wang et al. [31] investigated a rectangular enclosure with natural convection, nanofluid particles and heated on the right vertical wall with a sinusoidal temperature using the Boltzmann method. The ability of the lattice Boltzmann method on the natural convection MHD in a right vertical wall sinusoidal heated cavity filled with nanofluid particles was investigated by Kefayati [32]. The lattice Boltzmann method produced results that were in excellent agreement with previously published results. It was discovered that the rate of heat transfer was reduced by increasing the Hartmann number [32]. Sajjadi et al. [33] proposed the double multi relaxation time lattice Boltzmann method for natural convection heated on the right vertical wall cavity filled with porous medium and copper/water nanofluid particles. When the method's accuracy was compared to the results in the literature, it showed excellent agreement. It was discovered that the volume fraction of nanoparticles, Rayleigh number, Darcy number, and phase deviation all increase the heat transfer rate.

Parvin et al. [34] investigated double-diffusive natural convection, heat and mass transfer in a cavity. The study looked at the effect of the Soret and Dufour coefficients. A water-based nanofluid containing Al_2O_2 nanoparticles was used to fill the cavity. The flow equations were solved using the Galerkin finite element method. The flow streamlines, isotherms, and isoconcentrations are all affected by the Soret-Dufour coefficients. When the Soret coefficient was changed, the velocity profiles changed significantly more than when the Dufour coefficient was changed.

Mondal and Sibanda [35] investigated natural convection with double diffusion, heat and mass transfer in a cavity with two heated walls. The purpose of the study was to look into the effect of the Rayleigh number and buoyancy ratio on flow structures like streamlines, isoconcentrations, isotherms, Nusselt numbers, and Sherwood numbers. The control-volume finite-difference and stagged grid methods were used in this study. As the buoyancy ratio increases, the thickness of the boundary layer decreases. As

the flow structure changes, a high buoyancy ratio has a significant impact on concentration, resulting in vertical stratification in the enclosure. When compared to solutal buoyancy, thermal buoyancy has the opposite effect.

In a square cavity filled with a nanofluid and with heated vertical walls, Sivasankaran and Pan [36] numerically studied natural convection, heat, and mass transfer. The flow equations were numerically solved with the finite volume method. Among other things, they discovered that phase deviation increases heat transfer. Malomar et al. [37] investigated heat and mass transfer in natural convection in a porous square cavity with sinusoidally heated vertical walls. When compared to constant heating, the oscillating heating provided better thermal transfer performance [36]. Mejri et al. [38] investigated laminar natural convection and entropy generation in a square cavity filled with water AL_2O_3 nanofluid and vertical walls heated with a sinusoidal temperature using the lattice Boltzmann method and the finite difference method, respectively. It was discovered that as concentration increased, heat transfer rate increased while entropy generation decreased. Javaherdeh and Najjarnezami [39] used the lattice Boltzmann method to investigate sinusoidal temperature distribution on two walls and porous media on an MHD natural convection. The effect of the Hartmann number, Darcy number, phase deviation, and porosity on fluid flow and heat transfer was numerically investigated. The temperature distribution on the vertical walls was found to affect heat transfer. Heat transfer increased as the Darcy number and porosity increased, while the Hartmann number decreased. Using the finite volume method, Bhuvaneswari et al. [40] investigated the heat transfer of a convective flow in a cavity with vertical walls heated sinusoidally and a magnetic field inside. The obtained results demonstrated that increasing the amplitude ratio increased the heat transfer rate.

Sivasankaran and Bhuvaneswari [41] investigated flow in a square porous cavity with buoyancy induced convection, sinusoidally heated vertical walls, and the Brinkman Forchheimer extended Darcy model using the finite volume method. The numerical results revealed that the heat transfer rate was greater for both heated vertical walls than for one sinusoidally heated vertical wall. Deng and Chang [42] investigated a two-dimensional rectangular cavity with steady laminar natural convection. The cavity vertical walls were heated sinusoidally with varying amplitudes and phases. The finite volume method was used to discretize the governing equations, which were then solved using the SIMPLE algorithm. Wu et al. [43] investigated the heat transfer of a non-Darcian natural convective flow in a rectangular cavity. The cavity was filled with a porous medium and heated on both vertical walls with sinusoidal temperature variations. The model used was a local thermal non-equilibrium model. The governing equations were solved using the finite volume method, and the SIMPLE algorithm was used to couple the velocities and pressure. Sheremet and Pop [44] investigated natural convection in a square cavity filled with porous media and nanofluid using the finite difference method. Buongiorno's mathematical model with sinusoidally heated vertical walls was used in the study. Arani et al. [45] looked into a cavity flow with double-diffusive natural convection. The cavity was filled with a Al_2O_2-water nanofluid and the left vertical wall was partially heated and the vertical right wall was partially cooled or cooled with a sink. The study looked at how parameters like the source or sink location, buoyancy ratio, and

Rayleigh number affected fluid flow, heat, and mass transfer inside the cavity. The flow equations were solved using the finite volume method in this study. According to the findings, a buoyancy ratio close to zero results in the lowest heat transfer rate. The Rayleigh number and the buoyancy ratio, respectively, increase and decrease the average Nusselt number and average Sherwood.

Nik-Ghazali et al. [46] investigated cavity flow in a square annulus. They looked into the effects of Soret and Dufour on heat and mass transfer in a porous square annulus. The square annulus was heated from the outside and cooled from the inside. The finite element method was used to solve the flow equations. The two-peak values of the Nusselt number at the bottom moved to the center as the Dufour parameter increased, resulting in maximum heat transfer. The Sherwood number fluctuated along the bottom wall as the width ratio increased. Botella and Peyret [47] applied the Chebyshev collocation method to equations describing fluid motion inside a lid-driven cavity. Erturk et al. [48] investigated a steady incompressible flow in a moving top wall enclosure. A fine grid numerical method and Reynolds numbers up to 21000 were used in the study. The method was useful for resolving steady-state problems as well as vortices that appeared at cavity corners as the Reynolds number increased. The method achieved a residual error of less than 10^{-10}.

Bruneau and Saad [49] conducted research on two-dimensional lid-driven cavity flow. The numerical scheme of third order upwind was used in this study. A wide range of Reynolds numbers were simulated numerically. To compare the results to those in the literature, steady state and periodic solutions near the critical Reynolds number were presented. The linearized problem used to localize the first high Reynolds number turbulent solution was described, and the presence of an attractor was confirmed. Martinez and Esperança [50] conducted research on viscous incompressible two-dimensional fluid flows in a lid-driven cavity. The governing equations and boundary conditions were solved by combining the projection method with a Chebyshev collocation spectral method and a second order explicit-implicit time scheme. The method was shown to be stable, and the solution predicted the flow inside the cavity for Reynolds numbers up to 10000. Bognár and Csáti [51] conducted research on lid-driven cavity flow with incompressible Newtonian fluids. The study's goal was to solve time-dependent equations using spectral methods.

Poochinapan [52] validated the efficiency and accuracy of a finite difference scheme for solving the Navier-Stokes equations using lid-driven cavity flow. The numerical investigation revealed that the finite difference scheme with nonlinearity was effective for high Reynolds number flows. Erturk [11] investigated incompressible flow in a two-dimensional lid-driven cavity flow problem, focusing on physical, mathematical, and numerical aspects. For high Reynolds numbers, the investigation made use of a very fine computational grid.

Goqo et al. [7] investigated flow in a square lid-driven cavity filled with a porous medium saturated with a nanofluid and with a constant bottom wall temperature. An applied magnetic field was applied to the cavity. The multivariate spectral quasilinearization method was used to investigate the entropy generated by fluid friction, heat, and mass transfer. The accuracy of the method for nonlinear partial differential equations over a large time domain and in two space variables was confirmed by solving cavity

flow equations. The numerical results revealed that flow parameters like the Rayleigh, Eckert, and Lewis numbers have a significant impact on flow behavior, heat, and mass transfer rates. The generation of entropy was affected by the Rayleigh number and was discovered to be strongly dependent on Brownian motion parameter.

Basak et al. [53] used the Galerkin finite element method to investigate cavity flow with vertical left and right walls cooled. Heat is mostly transferred by convection due to the isotherms along the side walls and high Prandtl numbers. Jafari at el. [54] investigated cavity flow with an oscillating lid. The temperature of the vertical walls was kept constant, with the left heated and the right cooled. A control volume approach and the SIMPLE algorithm with a staggered grid were used to solve the equations. The direction of the sliding lid influences the effect of Reynolds and Grashof numbers on the flow and heat transfer field. When the lid moves in the negative direction, the average Nusselt number rises due to thermal boundary disturbance caused by a secondary vortex. As the Grashof and Reynolds nummbers rise, so does the average Nusselt number.

Esfe et al. [55] studied mixed convection inside a cavity filled with a water-copper nanofluid. In four different cases, the movement of the walls was investigated. In Case 1, the top wall shifted to the right, while the left vertical wall shifted downward. In Case 2, the top wall shifted to the left, while the left vertical wall rose. Case 3 presents, the top wall shifted to the right, while the left vertical wall rose. Case 4 presents, the top wall shifted to the left, while the left vertical wall shifted downward. The studies looked at the effects of parameters like wall movement and nanoparticle concentration on the structure of streamlines and isotherms in convection-dominated flow. The equations were numerically solved using a staggered grid system and the finite volume method. The streamlines were shown to be uniformly distributed. The addition of nanoparticles to the base fluid increased the strength of the vortices in all cases. Heat transfer increased as the concentration of nanoparticles increased.

Bhuvaneswari et al. [56] investigated the Soret effect on heat and mass transfer in a two-sided driven cavity filled with air using double-diffusive mixed convection. The vertical walls moved at a constant speed, and the right and left walls were heated and cooled separately. The finite volume method was utilized to solve the governing equations. When both walls moved upwards, the Richardson numbers produced a multicellular flow pattern. Heat and mass transfer were reduced when both walls moved upwards, and there was a higher mass transfer rate than heat transfer rate when the right wall moved upwards and the left wall moved downwards. High Richardson numbers had no effect on the local Nusselt and Sherwood numbers. With changes in Soret numbers, mass transfer was affected more than heat transfer for certain Richardson numbers. The rate of heat and mass transfer was increased for walls moving in opposite directions. Even though the direction of movement of the walls had an effect, increasing the Richardson number reduced the heat and mass transfer rate in all cases.

Nithyadevi and Yang [57] studied double-diffusive natural convection as well as the Soret and Dufour effects in a square cavity filled with water. The two vertical walls were heated to varying but consistent temperatures. The control volume method with the SIMPLE algorithm and the QUICK scheme was used to solve the governing equations. An increase in the Rayleigh number resulted in an increase

in heat and mass transfer rate regardless of the location of the heat source. High Dufour coefficient values resulted in increased fluid velocity and heat transfer. For partially heated walls with a high Soret coefficient, velocity was reduced while mass transfer was high.

Elshehabey and Ahmed [58] used the Buongiorno's nanofluid model to investigate the MHD mixed convection of a lid-driven cavity with both vertical walls heated with sinusoidal temperature. They also looked into the impact of an inclined uniform magnetic field, Brownian motion, and the thermophoresis parameter. The governing equations were solved using the finite volume method. The findings were compared to the literature and found to be in perfect agreement. The results of the study were presented in terms of streamlines, isotherms, isoconcentration, and local Nusselt number. The presence of an inclined magnetic field was reported to cause a loss of fluid movement.

Mixed convection in a two-dimensional cavity was studied by Ducasse and Sibanda [59]. Their research assumed linear and sinusoidal heating of various walls in lid-driven cavity flow. They looked at two scenarios: one in which both vertical walls were heated linearly, and another in which both vertical walls were cooled at a constant rate while the top wall was heated with a sinusoidal temperature variation. The penalty-Galerkin finite element method was used to solve the flow equations numerically. They demonstrated that linear heating and uniform cooling of the walls have an effect on circulation and local average Nusselt numbers. The circulation strength for cooled walls was significantly stronger for the clockwise circulation and only moderately strong for the anticlockwise circulation. The strength difference is reduced as the Reynolds and Grashof numbers increase [59].

Aydin and Yang [60] investigated shear and buoyancy induced flow and heat transfer in a two-dimensional square cavity filled with air, with the bottom wall locally heated and moving side walls, using the finite difference method. The heat source was located in the bottom wall's center. The influence of parameters on streamline patterns, isotherms, and the local Nusselt number was studied. The main focus of the research was the effect of the Richardson parameter. They discovered that as the parameter is increased, three flow regimes emerge: forced, mixed, and natural convection. Guo and Sharif [61] extended Aydin and Yang's study to include an investigation of the effect of the aspect ratio for a series of Richardson numbers and the ratio of heat source length to enclosure width. They discovered two counter-rotating vortices in the flow. For the dominant mechanism of heat transfer and low values of the Richardson number, the temperature was evenly distributed within the enclosure. The heat source affects a large portion of the enclosure. Increasing the length of the heat source raises the temperature in the affected area. As the source of heat moves toward the side wall, the maximum temperature drops while the average Nusselt number rises. Heat transfer improves rapidly as the aspect ratio approaches unity in thin rectangular cavities, but not significantly in larger cavities. Shankar and Deshpande [9] reviewed the literature on the cavity flow problem and highlighted key milestones. They concluded that significant progress in understanding three-dimensional flow had been made.

1.4 Coefficients of heat and mass transfer

The Nusselt number and the Sherwood number are parameters that provide information about heat and mass transfer in fluid flows. Skin friction is another parameter of engineering interest.

1.4.1 The Nusselt number

The Nusselt number is a measure of heat transfer at a wall and is the ratio of conductive to convective heat transfer. The Nusselt number is affected by the geometry and thermal properties. Heat transfer between a solid and its surroundings occurs via a combination of convection and conduction. If the temperature of the cavity wall is higher than the temperature of the fluid surrounding it, heat is transferred by conduction to the fluid particles adjacent to the wall and transported by the flowing fluid to areas of the cavity with lower temperatures [62].

The heat transfer is described by Newton's law of cooling, which is given as

$$h(T_h - T_c) = -k\frac{\partial T}{\partial \bar{n}}\bigg|_{\bar{n}=\zeta}, \tag{1.1}$$

where h is the heat transfer coefficient, $\bar{n}$ is the normal direction to the plane and ζ is a constant. Note that $\bar{n} = \zeta$ indicates which surface or boundary the law is calculated for. When equation (1.1) is multiplied by the length L, it gives the following

$$\frac{hL}{k} = -\frac{L}{(T_h - T_c)}\frac{\partial T}{\partial \bar{n}}\bigg|_{\bar{n}=\zeta}. \tag{1.2}$$

The local Nusselt number Nu is equal to hL/k, hence

$$Nu = -\frac{L}{(T_h - T_c)}\frac{\partial T}{\partial \bar{n}}\bigg|_{\bar{n}=\zeta}. \tag{1.3}$$

In non-dimensional form this can be re-written as

$$Nu = -\frac{\partial \theta}{\partial n}\bigg|_{n=\zeta}, \tag{1.4}$$

where $\theta = (T - T_c)/(T_h - T_c)$ and $n = (\bar{n})/(L)$. The average Nusselt number is defined as

$$\overline{Nu} = \frac{1}{L}\int_0^L Nu. \tag{1.5}$$

The difference between the local and the average Nusselt number is that the local Nusselt number measures the heat transfer at local points across the cavity, while the average Nusselt number measures the net energy transfer across the length of the cavity wall [15, 62, 63].

For natural convection, the fluid remains stationary with Nusselt number less than unit. The motion of the fluid begins as the Nusselt number increases above one. For mixed convection, a value below unit means that the heat is transfered by conduction only and a greater value means the primary heat transfer is by convection [62].

1.4.2   The Sherwood number

The Sherwood number Sh is a nondimension fluid parameter that is used to characterize mass transport and is approximated as the ratio of the convective mass transport and the rate of diffusive mass [15, 64, 65].

Fick's law of diffusion which describes diffusion is given as

$$N_A{''} = -D_{AB} \frac{\partial C}{\partial \bar{n}}\bigg|_{\bar{n}=\zeta}, \tag{1.6}$$

where D_{AB} is a property of the binary mixture called the binary diffusion coefficient and C is the nanoparticle volume fraction. Fick's law of diffusion in a broader sense is

$$N_A{''} = h_m C_0, \tag{1.7}$$

where C_0 is the initial concentration and h_m is the mass transfer coefficient. Equating the two equation leads to

$$h_m = -\frac{D_{AB}}{C_0} \frac{\partial C}{\partial \bar{n}}\bigg|_{\bar{n}=\zeta}. \tag{1.8}$$

Using dimensionless parameters $\phi = C/C_0$ the convection mass transfer coefficient becomes

$$h_m = -\frac{D_{AB}}{L} \frac{\partial \phi}{\partial n}\bigg|_{n=\zeta}. \tag{1.9}$$

The Sherwood number Sh in dimensionless parameter is defined as

$$Sh = \frac{h_m L}{D_{AB}} = -\frac{\partial \phi}{\partial n}\bigg|_{n=\zeta}. \tag{1.10}$$

1.4.3   Skin friction

Skin friction is a drag force exerted on a flowing fluid in opposition to the fluid flow. It can also be said that it is the viscous drag between a flowing fluid and the solid surface of an object moving through it. The drag force is a combination of the wall shear and the pressure drag. For a Newtonian fluid, skin friction can be evaluated from the velocity gradient at the surface as [66]

$$\tau_s = \mu \frac{\partial u}{\partial y}\bigg|_{y=\zeta}, \tag{1.11}$$

where μ is the coefficient of dynamic viscosity. The local skin friction coefficient is evaluated as

$$C_f = \frac{2T_s}{\rho \alpha_m^2} = \frac{2\mu}{\rho \alpha_m^2} \frac{\partial u}{\partial y}\bigg|_{y=\zeta}. \tag{1.12}$$

We introduce the stream function Ψ to ensure that the continuity equation is satisfied identically [62]. The stream function is defined through the relations

$$u = \frac{\partial \Psi}{\partial \bar{y}}, \quad v = -\frac{\partial \Psi}{\partial \bar{x}}. \tag{1.13}$$

In terms of the stream function equation (1.12) becomes

$$C_f = \frac{2\mu}{\rho \alpha_m^2} \frac{\partial^2 \psi}{\partial y^2}\bigg|_{y=\zeta}. \tag{1.14}$$

1.5 Numerical methods

We find nonlinear differential equations in every field of study in science, engineering, finance, and biological systems. Nonlinear differential equations describe complex phenomena including wave propagation, chemical kinetics, population dynamics, and many other areas. Many methods have been proposed and used to obtain analytical and approximate solutions to nonlinear equations [67]. Analytical solutions give better insights into the behaviour of a physical model. However, it is often difficult, complicated, or impossible to find analytic solutions of highly nonlinear and or coupled systems [68]. Some solutions may be found experimentally. However, for differential equations modelling complex fluid flows, this could be time consuming and costly [69].

Computational fluid dynamics is important for finding solutions to problems whose exact analytical solutions are difficult to find. Scientists are constantly developing new computational techniques with improved properties and accuracy. There are, however, difficulties with storing large amounts of data. Although parallel computing systems are available, many only run on a single processor and therefore have memory limitations [68, 69]. The study of numerical algorithms has its origins in the works of Newton, Euler, Gauss, Jacobi, Lagrange, Adams, etc. [70]. The first problems solved numerically were related to the measurement of fields and continued fractions. Computers have had a great impact on the development of numerical analysis [70]. There are many numerical and semi-analytic methods in the literature. The popular numerical approaches for solving nonlinear differential equations include the finite difference, finite element and spectral collocation methods.

1.5.1 The finite difference method

The finite difference method (FDM) is among the oldest and simplest methods for solving differential equations. Euler developed this method circa 1768, and Runge made improvements to the method circa 1908. Since the early 1950s applications of the FDM have become wide spread, and the availability of computers added to the wide use of the method. There have been many theoretical studies of the accuracy, stability and convergence properties of the FDM. Currently, there are many different versions of the FDM, although the fundamental idea is the same. Examples include explicit methods, implicit methods, the Crank–Nicolson scheme, nonstandard finite difference method, etc. In general, the difference between these FDMs is the form of the discretization used [71]. The main principle is to approximate derivatives using a differential quotient. The domain is discretized in space and in time and an approximate solution computed. A discretization error is caused by replacing the differential operator with the differential quotient. A truncation error may arise from taking the finite part of the Taylor series used in the approximation [71, 72].

Wang and Lin [73] studied an inverse problem using the finite-difference scheme. They reported that the implicit method requires more work than the explicit method in computing a solution. However, the additional work is rewarded by better accuracy and stable results compared to the explicit method. Tayakout et al. [74] investigated different control volumes of a catalytic membrane reactor using finite differences as one of the methods. It was reported that the finite difference method could be used on

optimization problems. Singer and Turkel [75] investigated the Helmholtz equation in one and two dimensions using the finite difference method. The study aimed to develop higher order finite difference methods. Kalis [76] developed an efficient difference method for solving heat transfer problems. Yuste and Acedo [77] investigated fractional diffusion equations using the explicit finite difference. They report that the method can be extended to higher dimensions. The method produced results that were in agreement with the exact solutions. Meerschaert and Tadjeran [78] investigated a class of initial-boundary value fractional PDEs with a finite domain. The study used the finite difference method which was reported to produce accurate results. Martino et al. [79] solved the Fisher equation using the finite difference method. Chen et al. [80] solved the fractional reaction-subdiffusion equation using the implicit finite difference method. It was found that the method gives accurate results that agree with exact solution. Zhuang et al. [81] used the implicit finite difference method to solve the anomulous subdiffusion equation. They reported that the method can be used to solve fractional integro-differential and higher order problems. Cui [82] solved a fractional diffusion equation using the compact finite difference method. It was found that the method is accurate with a tridiagonal coefficient matrix making the linear system of equations easy to solve. Wong and Li [83] introduced a novel finite difference scheme in solving the Hemholtz equation. The method was reported to be capable of solving high frequency cases such as the Helmoholtz equation at any wavenumber without the use of a fine step size. Moreover, the method produced accurate numerical results while the sparse structure for linear systems are simple when compared to one of the standard second order central difference schemes. Hickson [84] introduced a finite difference scheme to solve equations for multilayered materials that have a range of conditions such as a jump matching condition between layers. The study reported that the method is flexible, easy to implement and shows multilayered diffusion behaviour. Sweilam et al. [85] used the finite difference method to solve two-sided space-fractional wave equations. The study reported that the FDM gives good results when compared to the exact solution. Sousa [86] introduced a second order explicite finite difference method to solve fractional advection diffusion problems with source terms in the domains and homogeneous boundary conditions. Nowamooz et al. [87] investigated heat distribution of an unsaturated multilayered soil and thermal diffusivity that varies with time and depth using the FDM. Wang et al. [88] introduced the finite difference lattice Boltzmann model to solve an asisotropic convection diffusion equation. The model was found to give second order convergence and to be more accurate than the standard lattice Boltzmann model.

1.5.2 The finite element method

The finite element method (FEM) is used for solving partial differential equations [89, 90]. It has been used to solve engineering problems in heat transfer, fluid flow, stress analysis, and other areas [89]. The problem domain is represented as an assembly of finite elements. The equation is discretized from the continuous physical problem with unknown nodal values. Linear problems are solved as a system of linear algebraic equations [90]. The FEM has two important features. The first is approximating the physical field on a finite element in a piece-wise manner. Increasing the number of elements reduces the error in the approximated solution. The second feature is approximating locally the discretized

problems, which leads to a sparse system. This is very useful for solving large systems [90]. The FEM has been used to solve complex problems, for instance problems with a complex geometry, complex restraints and complex loading. However, for some problems it has been shown that other methods may be more efficient than the FEM [89].

Goldstein [91] solved a Helmholtz type boundary value problem in an unbounded region and with infinite boundaries using finite element methods. Ludwig and Lord [92] solved the ultrasonic nondestructive testing system using the finite element method. Hiltunen [93] introduced the finite element method to solutions of isothermal steady state particulate two-phase flow equations. The study verified the accuracy and robustness of the method. Chowdhury and Narasimhan [94] introduced the cohesive finite element method to solve equations for fracture and delamination in solids. Tezduyar [95] reviewed the finite element method for moving boundaries and interfaces. Boncut [96] analyzed the finite element method using the Navier-Stokes equations flow problems. They considered a stationary flow of a viscous fluid inside a pipe. Nagrath et al. [97] studied incompressible bubble dynamics in three dimensions using the finite element method. Marchandise and Remacle [98] combined the implicit pressure stabilized finite element method for solving incompressible two-phase flow problems with a quadrature free discontinuous Galerkin method. The method was used in the simulation of three-dimensional incompressible two-phase flow. The method was found to give second order accuracy in space and time. Ammar et al. [99] investigated a field model for alloys with a general framework of continuum thermodynamics in conjunction with generalized stresses using finite element methods. Mantari and Canales [100] used the Hermite-Lagrangian finite element method for laminated beams with several boundary conditions to solve a 6 degree of freedom hybrid type quasi-3D higher order shear deformation theory in a study of a static analysis of laminated beams. The numerical results were compared and validated using the finite element method. The results were found to be in excellent agreement with literature. Roy et al. [101] investigated the heat transfer in the melting, consolidation and re-solidification process that occurs in selective laser additive manufacturing using the finite element method.

1.5.3   Spectral methods

Spectral methods were proposed in the 1940s as a tool for large-scale computations in fluid dynamics. They were later extended to a broader class of problems and their accuracy and efficiency has been tested in many studies in the last few decades [102]. Spectral methods may be viewed as an improvement of the methods of weighted residual (MWR) which is a class of discretization schemes for differential equations. The MWR has two main elements namely, a trial or approximating function and a test or weighting function [103].

The trial function is one of the features that distinguishes spectral methods from finite-difference and finite-element methods. Spectral methods have infinitely differentiable trial functions. Finite-elements methods divide the domain into small elements and a trial function is specified in each element. Thus the trial functions are local in character and suited for handling complex geometry [103]. Finite-difference trial functions are likewise local. The nature of test functions distinguish types of spectral schemes,

namely, the collocation, Galerkin, and tau methods. The test functions in the Galerkin approach are the same as the trial functions. There are infinitely many smooth functions that individually satisfy the boundary conditions. The integral of the residual multiplied by each test function is required to be zero [103]. The test functions for the collocation approach are translated Dirac delta functions. The differential equation must be satisfied exactly at the collocation points. Spectral tau methods and Galerkin methods are similar in that satisfying the differential equation is enforced. The test function does not need to satisfy the boundary conditions. Therefore, an additional equation is used to apply the boundary conditions [103].

The simplest spectral scheme is the collocation approach. It was developed as a general method for solving ordinary differential equations. The first application of spectral collocation method to partial differential equations was made in the 1970s and this approach was called the pseudospectral method [103]. The Galerkin approach is regarded as the most aesthetically pleasing of the methods of weighted residuals because the test and trial functions are the same and the physical problem can be discretized in terms of the variational principle. The first application of spectral methods using the Galerkin approach to solve partial differential equations was in meteorological modelling. The Galerkin spectral methods are impractical for problems with complicated nonlinear terms [103]. A modification of the Galerkin method is the tau approach, which is useful for non-periodic boundary conditions. This method is difficult to apply to nonlinear problems but is very useful for constant coefficient problems or sub-problems [103].

1.5.4 The spectral quasilinearization method

The spectral quasilinearization method (SQLM) uses the Newton-Raphson based quasilinearization method and the Chebyshev spectral collocation method to respectively linearize and integrate the governing equation. There are now a number of papers where this method appears. Motsa et al. [104] applied the SQLM to nonlinear PDEs that model unsteady boundary-layer flow problems. The SQLM was found to be efficient in terms of computational accuracy and speed. RamReddy et al. [105] used the SQLM to study the mixed convective flow of a micropolar fluid along a permeable vertical plate under the convective boundary conditions. The study showed dual solutions for some parameter values. The influence of parameters like the Biot number, micropolar parameter was studied. Muzara et al. [106] solved the nonlinear Bratu problem using the SQLM and compared the result with the B-Spline and iterative finite difference methods. They concluded that better accuracy could be achieved by increasing the number of collocation points although at the cost of more time to execute the code as the number of collocation points increased. They concluded that the method is accurate, easy to implement and more computationally efficient than the other methods. Mondal and Sibanda [107] used the SQLM to study Sikiadas nanofluid flow using a Cattaneo-Christov heat flux model with a moving plate and inclined magnetic field. The method was found to converge rapidly and gave an accurate solution. The influence of physical parameters was studied and the Reynolds number was found to increase the rate of entropy generation. Alharbey et al. [108] investigated the boundary-layer micropolar fluid over a horizontal plate embedded in a non-Darcy porous medium using the SQLM. Fluid behaviour was

investigated in terms of changes in the angular velocity, temperature and entropy generation. Increasing the material parameter increased the fluid angular velocity. The increase in Reynolds and Binkmann numbers reduced the rate of entropy generation. Ibrahim [109] studied convective heating and compared the SQLM with the in-built MATLAB bvp4c method. They investigated the impact of the second order slip and convective heating on boundary-layer flow and heat transfer in a nanofluid over an extensible surface. The variables of interest were the local Nusselt number, the skin friction coefficient, and Sherwood number. These were affected by the particle Brownian motion and thermophoresis. An increase in both the thermophoresis and Brownian motion parameter reduced both the local Nusselt and Sherwood numbers. The slip parameter reduced the skin friction coefficient. The results from the SRM and SQLM were found to be in excellent agreement.

1.5.5 The bivariate spectral quasilinearization method

The bivariate spectral quasilinearization method (BSQLM) was introduced by Motsa et al. [67] as an improvement to the SQLM. This method combines three techniques, namely the bivariate Lagrange interpolation method, the Chebyshev spectral collocation method, and the quasilinearization method. The Chebyshev spectral collocation method with Lagrange interpolation polynomials is applied independently in space and time variables of the linearized system. The BSQLM achieves uniformly accuracy, uses fewer grid points, converges fast to the solution and the results are valid in large space and time domains. This method is more efficient in finding solutions of higher order nonlinear evolution partial differential equations. Oyelakin et al. [110] investigated heat transfer and unsteady mixed convection in a porous medium filled with a nanofluid using the BSQLM. Muzara et al. [111] investigated highly nonlinear two-dimensional Bratu problem using the BSQLM and Chebyshev spectral collocation method. The BSQLM and Chebyshev spectral collocation methods were compared and both were found to converge to the lower branch solution. The BSQLM performs better than the Chebyshev spectral collocation method in terms of speed and computational efficiency. Goqo et al. [112] studied entropy generation in MHD flow using the BSQLM. The influence of the flow parameters was studied with only two parameters namely the Reynolds number thermal radiation found to have any major effect on the rate of entropy generation. Goqo et al. [113] applied the BSQLM to flow with oxytactic microorganisms in rotational nanofluid flows with convective boundary conditions. The denser microorganisms swim to the top following the oxygen gradient within the fluid. An increase in the bioconvection Rayleigh number was shown to reduce the primary velocity while increasing the secondary velocity. The secondary velocity could be positive or negative depending on the velocity ration. Below a ration of 0.5 it was positive while for a ration greater than 0.5 it was negative. Magagula et al. [114] solved the non-similar boundary-layer equations that govern the MHD problem of forced convection flow along a nonisothermal wedge using the BSQLM. The method was validated through residual error analysis, convergence analysis, grid independence test and against published results. The method was found to be efficient, accurate and converged quadratically using only a few grid points.

1.5.6 The multi-domain bivariate spectral quasilinearization method

The multi-domain bivariate spectral quasilinearization method (MDBSQLM) was introduced by Magagula et al. [115] as an improvement to the BSQLM. To improve accuracy in large time intervals, the MDBSQLM employs Legendre-Gauss-Lobatto grid points rather than Chebyshev-Gauss-Lobatto grid points. The method linearizes nonlinear terms using quasilinearization. The pseudospectral collocation method is independently applied in time and space. The multi-domain approach divides the domain into non-overlapping subintervals. The method uses the continuity condition to match solutions across the subintervals. The method was tested on several equations and was found to be better than the BSQLM in terms of convergence, accuracy and computational time [115]. There have been several studies using this method. Oyelakin et al. [116] used the MDBSQLM to investigate heat and mass transfer in a non-Darcian and non-Newtonian power-law fluid flow for a porous medium with an embedded flat plate. The effect of source terms, such as thermal radiation, internal heat generation, and partial velocity slip, on the skin friction and heat and mass coefficients were considered. The slip parameter was found to increase the fluid velocity. The Biot and Dufour numbers increased the temperature of the fluid. The chemical reaction and solutal slip parameters reduced the concentration. Goqo et al. [117] applied the MDBSQLM to heat and mass transfer in steady laminar flow of MHD viscous incompressible boundary-layer flow on a permeable flat plate. The method overcame the weakness of the failure on other methods to capture solutions for large transpiration parameter values. The transpiration parameter reduced the momentum and thermal boundary-layers. Oyelakin et al. [118] used the MDBSQLM to investigate mixed convection in a Casson nanofluid with heat generation. The study concerned a fluid flow past a permeable moving flat plate in the presence of a chemical reaction and viscous dissipation. The influence of various fluid parameter on the velocity, temperature, nanoparticle concentration profiles, local skin friction and mass transfer coefficients was investigated. Ayano et al. [119] used the MDBSQLM to study natural convection in MHD flow with radiation on a sphere with Ohmic heat dissipation. The method was found to be efficient for solving fluid flow dynamics problems. Samuel and Motsa [120] extended the multidomain bivariate spectral collocation method to solutions of hyperbolic PDEs defined on large time domains. The PDEs are solved independently on small non-overlapping subintervals of the time domain. The method uses bivariate Lagrange interpolating polynomials to approximate solutions of the PDEs. The solutions along common boundaries were matched to approximate the solution. The method was found to be effective, accurate and fast in computational convergence.

1.5.7 The multivariate spectral quasilinearization method

The multivariate spectral quasilinearization method (MSQLM) first appeared in Goqo et al. [7] . This method is also an improvement on the BSQLM. Dlamini and Magagula [121] further improved the method to allow discretization in both space and time variables using the spectral collocation method. The solutions were compared with the exact solution of the problem and found to be accurate and efficient for self-similar boundary-layer problems. The method requires only a few grid points to achieve highly accurate results.

1.5.8 Overlapping spectral quasilinearization method

Mkhwatshwa [122] modified the SQLM to use the overlapping grid strategy by dividing the main domain into several subdomains. The modification overcame the limitations associated with the SQLM whose accuracy deteriorates with an increase in the computational domain. The method was used to solve the equations of the three dimensional MHD flow of a Casson nanofluid along a stretching surface. With the overlapping grid the coefficient matrix is sparse which improves accuracy. The method was found to give highly accurate results using a few iterations and grid points in each subdomain. Several studies using the overlapping method now exist in the literature.

1.5.9 The multidomain overlapping bivariate spectral quasilinearization method

Mkhwatshwa et al. [123] improved the MDBSQLM for use in both space and time and used overlapping subdomains in solving non-similar boundary equations. The overlapping intervals were introduced in the space domain while time domain remained nonoverlapping. The method was validated in a series of studies in the literature. Mkhwatshwa et al. [124] investigated free convection in an enclosure filled with copper water and silver water nanofluid particles. The results were found to be in good agreement with those in the literature. The effect of the parameters on the surface temperature, skin friction coefficient, and the rate of heat were investigated. Mkhwatshwa et al. [125] investigated the effects of diffusion-thermal, chemical reaction, thermo-diffusion, and Hall effect on heat and mass transfer on MHD flow over a vertical slender cylinder filled with a silver water nanofluid using the overlapping multidomain bivariate spectral quasilinearization method. Mkhwatshwa et al. [126] used the MDOBSQLM in their investigation of the effect of thermal convective boundary conditions, partial slip flow, and non-uniform heat source on MHD. The method was found to require a few grid points to achieve accurate results with a few iterations. Minimum grid points on each subinterval minimizes the effect of round-off errors that can lead to instabilities. Maximizing the overlapping subintervals maximizes the accuracy of the method. Mkhwatshwa et al. [127] modified the method to apply the overlapping domain decomposition in both space and time and applied it to solve Emden-Fowler equations. The method was tested on several examples and compared with the exact solution. The method was found to be efficient and accurate using a few grid points in each subinterval. Mkhwatshwa et al. [128] investigated unsteady MHD flow, temperature-dependant fluid properties, heat and mass transfer in an Eyring-Powell fluid over a stretching oscillatory surface in porous media. The equations were solved using MDOBSQLM which was found to be accurate, stable, computationally efficient and gave results after few iterations with a few grid points in each subdomain. Mkhwatshwa et al. [129] used the MDOBSQLM to investigate the combined effects of nonlinear thermal radiation, exponentially varying viscosity and thermal conductivity in a three dimensional MHD bioconvective flow of Casson nanofluid with gyrotactic microorganisms. The results were in excellent agreement with the results in literature.

Samuel [130] introduced the concept of overlapping grid points to the multidomain spectral collocation method for parabolic PDEs defined on large domains. The study sought to show that decomposing large space and time computational intervals into small subintervals gives better accuracy than increasing the

number of grid points in a single domain. The multidomain spectral collocation approach was applied in both space and time with the domain decomposed into small, equal overlapping and non-overlapping subdomains in space and time respectively. The method was found to be effective and accurate.

Samuel and Motsa [131] introduced the trivariate Lagrange interpolating polynomials instead of the Lagrange interpolating polynomials to the overlapping grid multidomain spectral collocation method, and solved nonlinear initial boundary value problems over large time intervals. The method employed the spectral collocation based discretization in both space and time. The continuity condition was applied to obtain initial conditions in subsequent time subintervals. The method was tested on several single or systems of two dimension nonlinear parabolic PDEs. The results were in agreement with literature.

1.5.10 The multivariate overlapping grid spectral quasilinearization method

Samuel and Motsa [132]combined the overlapping grid method with the MSQLM to produce a numerical method for nonlinear boundary-layer flow problems defined on semi-infinite domains. This method modifies MSQLM to divide the domain into overlapping subintervals. The method solves a single or system of ODEs. The method was tested against the exact solutions where these existed, and residual errors evaluated where exact solutions did not exist. The method was found to be highly accurate, stable and computational efficient.

Samuel [130] further applied the method to nonlinear elliptic PDEs defined on large rectangular domains. The method addresses the limitations of spectral collocation methods which are not efficient on large domain problems. The Chebyshev-Gauss-Lobbato nodes were used on each subinterval. Mburu et al. [133] used the MOGSQLM in investigating entropy generation on an inclined cylinder unsteady nanofluid flow with thermal radiation, chemical reaction and a magnetic field. The impact of viscous dissipation, velocity slip conditions, thermal slip conditions, and Brownian motion were investigated. Mburu et al. [134] used the MOGSQLM to analyze the effect of the principal parameters on flow over a Riga plate, namely Hartman, Eckert, Brinkman, Reynolds numbers and the Brownian motion parameter. The method was analyzed for sensitivity and convergence and confirmed to be a stable and convergence of the method. The entropy generation increased with an increase in the width of the Riga plate, Brinkmann, Prandtl numbers and the Brownian motion parameter, and decreased with an increase in the Eckert and Deborah numbers.

There are many numerical methods that may be used to solve cavity flow problems; in this project we only explained the three most popular methods, namely the spectral, finite element and finite difference methods. The spectral methods are known to be the most accurate of the three. In this study we focus on the use of spectral schemes to solve a variety of cavity flow problems.

1.6   Aims and objectives

In this study we investigate fluid flows in cavities and solve the flow equations using the multivariate overlapping grid spectral quasilinearization method and the multivariate spectral quasilinearization method. The multivariate overlapping grid spectral quasilinearization method has not been used before to solve cavity flow problems. We compare the results to determine accuracy and the rate of convergence of the methods. We investigate how fluid parameters affect the distribution of streamlines, isotherms and isoconcentrations.

This study consists of five chapters, namely, the introduction, three chapters that focus on investigating cavity problems of varying complexity, and the conclusion. In this chapter we have provided a background to the study. In Chapter 2 we investigate natural convection in a square porous cavity. In Chapter 3 we study the flow in a cavity filled with porous medium that is saturated with a nanofluid. In Chapter 4 we investigate the flow of a nanofluid in a porous cavity with a magnetic field inside. We provide our conclusions in Chapter 5.

Chapter 2

On natural convection in a porous square cavity

In this chapter, we use the multivariate spectral quasilinearization and multivariate overlapping grid spectral quasilinearization methods to solve the problem of natural convection in a porous square cavity [37]. We investigate the effect of the Rayleigh number on a cavity with stationary walls and with the left and right vertical walls heated and cooled, respectively. There are few studies in the literature where spectral methods are used to solve cavity flow problems. In this investigation we came across Martinez and Esperanca [49] who used Chebyshev collocationspectral method and Goqo et al. [7] who used the MSQLM. The MSQLM is the most recent spectral method applied to cavity flow. However, a recent improvement of the MSQLM is the MOGSQLM [132]. The current existing literature on spectral methods suggests that the MOGSQLM is an improvement of the MSQLM with better accuracy and convergence rate overlap4. The problem of natural convection in a square cavity filled with a porous medium is used to study the utility of these methods.

2.1 Mathematical formulation

Consider a square porous cavity of length L. The cavity walls are impermeable, adiabatic and stationary. The vertical left wall is heated to a temperature T_h and the right wall is cooled to a temperature T_c. The physical model and the coordinate system is shown in Figure 2.1. The flow is assumed to be steady, isotropic, homogeneous and in local thermal equilibrium with the porous medium. Using the Darcy-Boussinesq approximation the flow is described using the following continuity, momentum and

energy equations, respectively [23, 37, 48, 52]:

$$\frac{\partial u}{\partial \bar{x}} + \frac{\partial v}{\partial \bar{y}} = 0, \tag{2.1}$$

$$\frac{\partial v}{\partial \bar{x}} - \frac{\partial u}{\partial \bar{y}} = \frac{kg\rho_0\beta_T}{\mu} \frac{\partial T}{\partial \bar{x}}, \tag{2.2}$$

$$u\frac{\partial T}{\partial \bar{x}} + v\frac{\partial T}{\partial \bar{y}} = \alpha\left(\frac{\partial^2 T}{\partial \bar{x}^2} + \frac{\partial^2 T}{\partial \bar{y}^2}\right), \tag{2.3}$$

where, the velocity components along the x and y directions are respectively u and v, the fluid temperature is T, the thermal expansion's coefficient is $\beta_T = \frac{1}{\rho(\frac{\partial \rho}{\partial T})_p}$ and $\alpha = \frac{k_m}{(\rho c)_F}$ where k_m is the thermal conductivity of the solid phase or the fluid phase, k is the permeability, μ is the fluid viscosity, ρ_0 is the fluid density and g is the gravitational acceleration. The boundary conditions at the top, bottom, left and right walls are given in Figure 2.1.
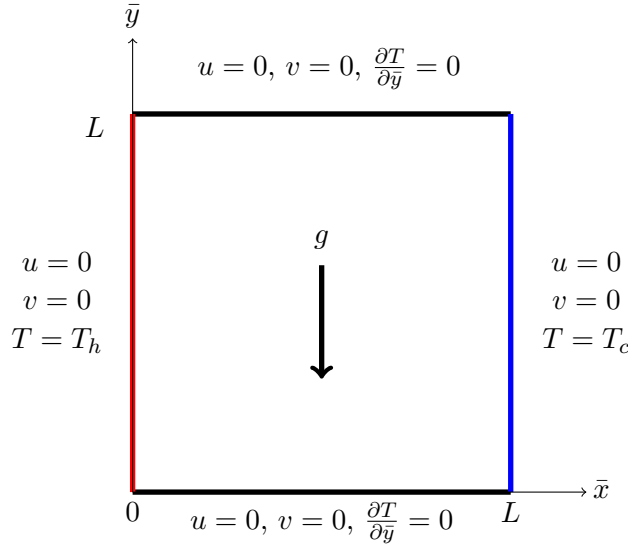
Figure 2.1: The geometry of the problem

Substituting the stream function equations (1.13) in equations (2.2) and (2.3), we obtain the following equations

$$\frac{\partial^2 \Psi}{\partial \bar{x}^2} + \frac{\partial^2 \Psi}{\partial \bar{y}^2} = -\frac{kg\rho_0\beta_T}{\mu} \frac{\partial T}{\partial \bar{x}}, \tag{2.4}$$

$$\frac{\partial \Psi}{\partial \bar{y}} \frac{\partial T}{\partial \bar{x}} - \frac{\partial \Psi}{\partial \bar{x}} \frac{\partial T}{\partial \bar{y}} = \alpha\left(\frac{\partial^2 T}{\partial \bar{x}^2} + \frac{\partial^2 T}{\partial \bar{y}^2}\right). \tag{2.5}$$

To non-dimensionalize equations (2.4) and (2.5), we introduce the variables,

$$x = \frac{\bar{x}}{l}, \; y = \frac{\bar{y}}{l}, \; \psi = \frac{\Psi}{\alpha}, \; \theta = \frac{T-T_c}{\Delta T}, \tag{2.6}$$

to obtain the following equations

$$\frac{\partial^2 \psi}{\partial x^2} + \frac{\partial^2 \psi}{\partial y^2} = -R_a \frac{\partial \theta}{\partial x}, \tag{2.7}$$

$$\frac{\partial \psi}{\partial y} \frac{\partial \theta}{\partial x} - \frac{\partial \psi}{\partial x} \frac{\partial \theta}{\partial y} = \frac{\partial^2 \theta}{\partial x^2} + \frac{\partial^2 \theta}{\partial y^2}, \tag{2.8}$$

where $R_a = (k\rho_0 g\beta_T \Delta Tl)/(\mu\alpha)$ is the Rayleigh number. The boundary conditions for the system of equations (2.7) - (2.8) are:

$$\psi(0,y) = 0, \quad \theta(0,y) = 1, \quad \psi(1,y) = 0, \quad \theta(1,y) = 0,$$

$$\psi(x,0) = 0, \quad \frac{\partial\theta}{\partial y}(x,0) = 0, \quad \psi(x,1) = 0, \quad \frac{\partial\theta}{\partial y}(x,1) = 0. \tag{2.9}$$

2.2 Numerical solution

Here we solve the non-dimensional equations (2.7) - (2.8) using the MSQLM and MOGSQLM. The MSQLM and MOGSQLM as described in this section will be used in Chapters 3 and 4. In Section 2.2.1 we describe the MSQLM. The MOGSQLM is described fully in Section 2.2.2.

2.2.1 The multivariate spectral quasilinearization solution

The basic idea when using the multivariate spectral quasilinearization method to solve nonlinear PDEs is to first, use the quasilinearization method to linearize the nonlinear terms and then find the solution at collocation points by approximating the unknown functions using Lagrange basis functions. The collocation points defined in the rectangular domain $[-1,1]\times[-1,1]$ used Gauss-Lobatto points $x_i = \cos\left(\frac{i\pi}{N_x}\right)$, and $y_j = \cos\left(\frac{j\pi}{N_y}\right)$ to approximate. Consider a two dimensional problem that describes a system of nonlinear elliptic PDEs.

$$F_1(v_1, v_2, ..., v_n) = h_1(x,y), \tag{2.10}$$

$$F_2(v_1, v_2, ..., v_n) = h_3(x,y), \tag{2.11}$$

$$\vdots$$

$$F_n(v_1, v_2, ..., v_n) = h_n(x,y) \tag{2.12}$$

where $h_1, h_2, \ldots, h_n$ are known functions, $F_1, F_2, \ldots, F_n$ are nonlinear operators operating on $v_1, v_2, \ldots, v_n$, and $v_1 = \left\{\frac{\partial^2 u_1}{\partial x^2}, \frac{\partial^2 u_1}{\partial y^2}, \frac{\partial^2 u_1}{\partial x\partial y}, \frac{\partial u_1}{\partial x}, \frac{\partial u_1}{\partial y}, u_1\right\}, v_2 = \left\{\frac{\partial^2 u_2}{\partial x^2}, \frac{\partial^2 u_2}{\partial y^2}, \frac{\partial^2 u_2}{\partial x\partial y}, \frac{\partial u_2}{\partial x}, \frac{\partial u_2}{\partial y}, u_2\right\}, \ldots v_n = \left\{\frac{\partial^2 u_n}{\partial x^2}, \frac{\partial^2 u_n}{\partial y^2}, \frac{\partial^2 u_n}{\partial x\partial y}, \frac{\partial u_n}{\partial x}, \frac{\partial u_n}{\partial y}, u_n\right\}$. Equations (2.10-2.12) are to be solved under the Robin boundary conditions

$$\alpha_{11}^a \frac{\partial u_1}{\partial x}(a,y) + \alpha_{10}^a u_1(a,y) = f_{a_1}(y), \ \ \alpha_{11}^b \frac{\partial u_1}{\partial x}(a,y) + \alpha_{10}^b u_1(a,y) = f_{b_1}(y),$$

$$\beta_{11}^c \frac{\partial u_1}{\partial x}(x,c) + \beta_{10}^c u_1(x,c) = g_{c_1}(x), \ \ \beta_{11}^d \frac{\partial u_1}{\partial x}(x,d) + \beta_{10}^d u_1(x,d) = g_{d_1}(x),$$

$$\alpha_{21}^a \frac{\partial u_2}{\partial x}(a,y) + \alpha_{20}^a u_2(a,y) = f_{a_2}(y), \ \ \alpha_{21}^b \frac{\partial u_2}{\partial x}(a,y) + \alpha_{20}^b u_2(a,y) = f_{b_2}(y),$$

$$\beta_{21}^c \frac{\partial u_2}{\partial x}(x,c) + \beta_{20}^c u_2(x,c) = g_{c_2}(x), \ \ \beta_{21}^d \frac{\partial u_2}{\partial x}(x,d) + \beta_{20}^d u_2(x,d) = g_{d_2}(x),$$

$$\vdots$$

$$\alpha_{n1}^a \frac{\partial u_n}{\partial x}(a,y) + \alpha_{n0}^a u_n(a,y) = f_{a_n}(y), \ \ \alpha_{n1}^b \frac{\partial u_n}{\partial x}(a,y) + \alpha_{n0}^b u_n(a,y) = f_{b_n}(y),$$

$$\beta_{n1}^c \frac{\partial u_n}{\partial x}(x,c) + \beta_{n0}^c u_n(x,c) = g_{c_n}(x), \ \ \beta_{n1}^d \frac{\partial u_n}{\partial x}(x,d) + \beta_{n0}^d u_n(x,d) = g_{d_n}(x), \tag{2.13}$$

where for $z = 1, 2, ..., n$, α_{z1}^a, α_{z0}^a, α_{z1}^b, α_{z0}^b, β_{z1}^c, β_{z0}^c, β_{z1}^d, β_{z0}^d are known constants and $f_{a_z}(y)$, $f_{b_z}(y)$, $g_{c_z}(x)$, $g_{c_z}(x)$ are known functions. The Equations (2.10-2.12) are also solvable with Neumann boundary conditions and Dirichlet boundary conditions. Setting α_{z0}^a, α_{z0}^b, β_{z0}^c, β_{i0}^d to zero reduces the boundary conditions Equations (2.13) to Neumann boundary conditions and α_{z1}^a, α_{z1}^b, β_{z1}^c, β_{z1}^d, to zero reduces the boundary conditions Equations (2.13) to Dirichlet boundary conditions. We assume the solution is of the form

$$u_1(x,y) = \sum_{i=0}^{N_x} \sum_{j=0}^{N_y} u_1(x_i,y_j) L_i(x) L_j(y), \ \ u_2(x,y) = \sum_{i=0}^{N_x} \sum_{j=0}^{N_y} u_2(x_i,y_j) L_i(x) L_j(y), \ \ ...$$

$$u_n(x,y) = \sum_{i=0}^{N_x} \sum_{j=0}^{N_y} u_n(x_i,y_j) L_i(x) L_j(y), \tag{2.14}$$

where the Lagrange functions $L_i(x)$ and $L_j(y)$ are defined as

$$L_i(x) = \prod_{i=0, i\neq k}^{N_x} \frac{x-x_k}{x_i-x_k}; \ \ \ L_j(y) = \prod_{j=0, j\neq k}^{N_y} \frac{y-y_k}{y_j-y_k}, \tag{2.15}$$

with

$$L_i(x_k) = \delta_{ik} = \begin{cases} 0 & i \neq k; \\ 1 & i = k. \end{cases}; \ \ \ L_j(y_k) = \delta_{jk} = \begin{cases} 0 & j \neq k, \\ 1 & j = k. \end{cases} \tag{2.16}$$

for $i = 0, 1, ..., N_x$ and $j = 0, 1, ..., N_y$. This solution is evaluated using the Gauss-Lobatto grid points. Let $u = u_z$ for $z = 1, 2, ..., n$, α_{z1}^a that is instead of dealing with each case we will deal with just u but the same applies for every u_z. The derivatives are approximated at the Chebyshev-Gauss-Lobatto points $(x^{(i)}, y^{(j)})$, for $i = 0, 1, ..., N_x$ and for $j = 0, 1, ..., N_y$. We approximate the derivatives of the function with respect to x as

$$U_x(x, y_j)|_{x=x_i} = \sum_{p=0}^{N_x} \sum_{q=0}^{N_y} u(x_p, y_q) L_q(y_j) \frac{dL_p(x)}{dx} \bigg|_{x=x_i}$$

$$= \sum_{p=0}^{N_x} D_{xi,p} U(x_p, y_j) = \boldsymbol{D_x U}_j = \frac{2}{b-a} \boldsymbol{\bar{D}_x U}_j, \tag{2.17}$$

where $\bar{\boldsymbol{D}}_{\boldsymbol{x}} = (b-a)\boldsymbol{D}_{\boldsymbol{x}}/2$ is a Chebyshev differential matrix of size $(N_x+1)\times(N_x+1)$ and $j=0,1,...,N_y$. Now we differentiate with respect to y

$$\begin{aligned}
U_y(x_i,y)|_{y=y_j} &= \sum_{p=0}^{N_x}\sum_{q=0}^{N_y} u(x_p,y_q)L_q(x_i)\frac{dL_p(y)}{dy}\bigg|_{y=y_j} \\
&= \sum_{q=0}^{N_y} D_{y_{j,q}}U(x_i,y_q) = \boldsymbol{D_y}\boldsymbol{U}_i = \frac{2}{d-c}\bar{\boldsymbol{D}}_{\boldsymbol{y}}\boldsymbol{U}_i,
\end{aligned} \tag{2.18}$$

where $\bar{\boldsymbol{D}}_{\boldsymbol{y}} = (d-c)\boldsymbol{D}_{\boldsymbol{y}}/2$ is a Chebyshev differential matrix of size $(N_y+1)\times(N_y+1)$ and $i=0,1,...,N_x$. For second order derivatives we approximate these as follows

$$\begin{aligned}
U_{xx}(x,y_j)|_{x=x_i} &= \boldsymbol{D_{xx}}\boldsymbol{U}_j, \\
U_{yy}(x_i,y)|_{y=y_j} &= \boldsymbol{D_{yy}}\boldsymbol{U}_i,
\end{aligned} \tag{2.19}$$

for $j=0,1,...,N_y$ and $i=0,1,...,N_x$ respectively, where

$$\mathbf{D}_{xx} = \mathbf{D}_x\mathbf{D}_x = \frac{4}{(b-a)^2}\bar{\boldsymbol{D}}_x^2 \text{ and } \mathbf{D}_{yy} = \mathbf{D}_y\mathbf{D}_y = \frac{4}{(d-c)^2}\bar{\boldsymbol{D}}_y^2.$$

The vectors $\mathbf{U}_i$ and $\mathbf{U}_j$ are defined respectively as

$$\mathbf{U}_i = [u(x_i,y_0), u(x_i,y_1), u(x_i,y_2), ..., u(x_i,y_{N_y})]^t$$

and

$$\mathbf{U}_j = [u(x_0,y_j), u(x_1,y_j), u(x_2,y_j), ..., u(x_{N_x},y_j)]^t,$$

where t denotes the vector transpose. In the case of higher order derivatives

$$\boldsymbol{D_{xx...x}} = \left(\frac{2}{b-a}\bar{\boldsymbol{D}}_{\boldsymbol{x}}\right)^m \text{ and } \boldsymbol{D_{yy...y}} = \left(\frac{2}{d-c}\bar{\boldsymbol{D}}_{\boldsymbol{y}}\right)^n$$

and mixed derivatives

$$\boldsymbol{D_{xx...xyy...y}} = \left(\frac{2}{b-a}\bar{\boldsymbol{D}}_{\boldsymbol{x}}\right)^m\left(\frac{2}{d-c}\bar{\boldsymbol{D}}_{\boldsymbol{y}}\right)^n,$$

where m and n are the order of the derivatives in x and y respectively. We transform the rectangular domain $[a,b]\times[c,d]$ into the computational domain $[-1,1]\times[-1,1]$ using the following linear mappings in the general form:

$$x = \frac{1}{2}[(b-a)X+b+a] \quad \text{and} \quad y = \frac{1}{2}[(d-c)Y+d+c]. \tag{2.20}$$

Equations (2.10-2.12) are linearized using quasilineatization method and solved at collocation points, but for simplicity we will show this using equations (2.7) - (2.8). We begin by assigning the following variables to the system of equations (2.7) - (2.8)

$$\Psi_1 = \psi_{xx}+\psi_{yy}+R_a\theta_x = 0, \tag{2.21}$$

$$\Theta_1 = \theta_{xx}+\theta_{yy}+\psi_x\theta_y-\psi_y\theta_x = 0, \tag{2.22}$$

where $\psi_x = \dfrac{\partial \psi}{\partial x}$ and $\psi_{xx} = \dfrac{\partial^2 \psi}{\partial x^2}$. All other derivatives are defined the same way. The rectangular domain $[0,1] \times [0,1]$ is transformed into the computational domain $[-1,1] \times [-1,1]$ using the linear mappings:

$$x = \frac{1}{2}[X+1] \quad \text{and} \quad y = \frac{1}{2}[Y+1]. \tag{2.23}$$

To linearize the equations, we use the quasilinearization method which is based on the Taylor series expansion. The terms at previous and current iterations are denoted by the subscripts r and $r+1$ respectively. Equations (2.21) - (2.22) become

$$a_{\psi_{xx},r}\psi_{xx,r+1} + a_{\psi_{yy},r}\psi_{yy,r+1} + a_{\theta_x,r}\theta_{x,r+1} = R_{\psi,r}, \tag{2.24}$$

$$b_{\psi_x,r}\psi_{x,r+1} + b_{\psi_y,r}\psi_{y,r+1} + b_{\theta_{xx},r}\theta_{xx,r+1} + b_{\theta_x,r}\theta_{x,r+1} + b_{\theta_{yy},r}\theta_{yy,r+1} + b_{\theta_y,r}\theta_{y,r+1} = R_{\theta,r}, \tag{2.25}$$

where

$$a_{\psi_{xx},r} = \frac{\partial \Psi_1}{\partial \psi_{xx,r}} = 1, \quad a_{\psi_{yy},r} = \frac{\partial \Psi_1}{\partial \psi_{yy,r}} = 1, \quad a_{\theta_x,r} = \frac{\partial \Psi_1}{\partial \theta_{x,r}} = R_a,$$

$$b_{\psi_x,r} = \frac{\partial \Theta_1}{\partial \psi_{x,r}} = \theta_{y,r}, \quad b_{\psi_y,r} = \frac{\partial \Theta_1}{\partial \psi_{y,r}} = -\theta_{x,r}, \quad b_{\theta_{xx},r} = \frac{\partial \Theta_1}{\partial \theta_{xx,r}} = 1,$$

$$b_{\theta_x,r} = \frac{\partial \Theta_1}{\partial \theta_{x,r}} = -\psi_{y,r}, \quad b_{\theta_{yy},r} = \frac{\partial \Theta_1}{\partial \theta_{yy,r}} = 1, \quad b_{\theta_y,r} = \frac{\partial \Theta_1}{\partial \theta_{y,r}} = \psi_{x,r},$$

$$R_{\psi,r} = a_{\psi_{xx},r}\psi_{xx,r} + a_{\psi_{yy},r}\psi_{yy,r} + a_{\theta_x,r}\theta_{x,r} - \Psi_1,$$

$$R_{\theta,r} = b_{\psi_x,r}\psi_{x,r} + b_{\psi_y,r}\psi_{y,r} + b_{\theta_{xx},r}\theta_{xx,r} + b_{\theta_x,r}\theta_{x,r} + b_{\theta_{yy},r}\theta_{yy,r} + b_{\theta_y,r}\theta_{y,r} - \Theta_1. \tag{2.26}$$

Using a multivariate Lagrange polynomial we rewrite the system of equations (2.24) -(2.25) for collocation points as the following scheme:

$$[diag(a_{\psi_{xx},r})\boldsymbol{D_{xx}}]\boldsymbol{\psi}_{r+1}(x_i,y_j) + [diag(a_{\psi_{yy},r})\boldsymbol{D_{yy}}]\boldsymbol{\psi}_{r+1}(x_i,y_j) + [diag(a_{\theta_x,r})\boldsymbol{D_x}]\boldsymbol{\theta}_{r+1}(x_i,y_j) = \boldsymbol{R}_{\psi,r,j},$$

$$\tag{2.27}$$

$$[diag(b_{\psi_x,r})\boldsymbol{D_x}]\boldsymbol{\psi}_{r+1}(x_i,y_j) + [diag(b_{\psi_y,r})\sum_{q=0}^{N_y}\boldsymbol{D_y}_{j,q}]\boldsymbol{\psi}_{r+1}(x_i,y_q) + [diag(b_{\theta_{xx},r})\boldsymbol{D_{xx}}$$

$$+ diag(b_{\theta_x,r})\boldsymbol{D_x}]\boldsymbol{\theta}_{r+1}(x_i,y_j) + [diag(b_{\theta_{yy},r})\sum_{q=0}^{N_y}\boldsymbol{D_{yy}}_{j,q} + diag(b_{\theta_y,r})\sum_{q=0}^{N_y}\boldsymbol{D_y}_{j,q}]\boldsymbol{\theta}_{r+1}(x_i,y_q) = \boldsymbol{R}_{\theta,r,j}, \tag{2.28}$$

where the vectors $\boldsymbol{R}_{\psi,r,j}$ and $\boldsymbol{R}_{\theta,r,j}$ are $\boldsymbol{R}_{\psi,r}$ and $\boldsymbol{R}_{\theta,r}$ are defined for each y_j for $j = 0, 1, ..., N_y$ respectively. Equations (2.27) - (2.28) are expressed in the following matrix form:

$$\begin{bmatrix} \begin{bmatrix} A_{0,0}^{0,0} A_{0,1}^{0,0} \\ A_{1,0}^{0,0} A_{1,1}^{0,0} \\ A_{0,0}^{1,0} A_{0,1}^{1,0} \\ A_{1,0}^{1,0} A_{1,1}^{1,0} \end{bmatrix} & \begin{bmatrix} A_{0,0}^{0,1} A_{0,1}^{0,1} \\ A_{1,0}^{0,1} A_{1,1}^{0,1} \\ A_{0,0}^{1,1} A_{0,1}^{1,1} \\ A_{1,0}^{1,1} A_{1,1}^{1,1} \end{bmatrix} & \cdots & \begin{bmatrix} A_{0,0}^{0,N_y} A_{0,1}^{0,N_y} \\ A_{1,0}^{0,N_y} A_{1,1}^{0,N_y} \\ A_{0,0}^{1,N_y} A_{0,1}^{1,N_y} \\ A_{1,0}^{1,N_y} A_{1,1}^{1,N_y} \end{bmatrix} \\ \vdots & \vdots & \ddots & \vdots \\ \vdots & \vdots & \ddots & \vdots \\ \begin{bmatrix} A_{0,0}^{N_y,0} A_{0,1}^{N_y,0} \\ A_{1,0}^{N_y,0} A_{1,1}^{N_y,0} \end{bmatrix} & \begin{bmatrix} A_{0,0}^{N_y,1} A_{0,1}^{N_y,1} \\ A_{1,0}^{N_y,1} A_{1,1}^{N_y,1} \end{bmatrix} & \cdots & \begin{bmatrix} A_{0,0}^{N_y,N_y} A_{0,1}^{N_y,N_y} \\ A_{1,0}^{N_y,N_y} A_{1,1}^{N_y,N_y} \end{bmatrix} \end{bmatrix} \begin{bmatrix} \begin{bmatrix} \psi_{r+1}^0 \\ \theta_{r+1}^0 \\ \psi_{r+1}^1 \\ \theta_{r+1}^1 \end{bmatrix} \\ \vdots \\ \vdots \\ \begin{bmatrix} \psi_{r+1}^{N_y} \\ \theta_{r+1}^{N_y} \end{bmatrix} \end{bmatrix} = \begin{bmatrix} \begin{bmatrix} R_{\psi,r}^0 \\ R_{\theta,r}^0 \\ R_{\psi,r}^1 \\ R_{\theta,r}^1 \end{bmatrix} \\ \vdots \\ \vdots \\ \begin{bmatrix} R_{\psi,r}^{N_y} \\ R_{\theta,r}^{N_y} \end{bmatrix} \end{bmatrix}.$$

where for $i = j$

$A_{0,0}^{i,i} = diag(a_{\psi_{xx,r}})\boldsymbol{D_{xx}}, \quad A_{0,1}^{i,i} = diag(a_{\theta_{x,r}})\boldsymbol{D_x},$

$A_{1,0}^{i,i} = diag(b_{\psi_{x,r}})\boldsymbol{D_x} + diag(a_{\psi_{y,r}})\boldsymbol{D_{y}}_{i,i}\boldsymbol{I},$

$A_{1,1}^{i,i} = diag(b_{\theta_{xx,r}})\boldsymbol{D_{xx}} + diag(b_{\theta_{x,r}})\boldsymbol{D_x} + diag(b_{\theta_{yy,r}})\boldsymbol{D_{yy}}_{i,i}\boldsymbol{I} + diag(b_{\theta_{y,r}})\boldsymbol{D_{y}}_{i,i}\boldsymbol{I},$ and for $i \neq j$

$A_{0,0}^{i,j} = \boldsymbol{O}, \quad A_{0,1}^{i,j} = \boldsymbol{O},$

$A_{1,0}^{i,j} = diag(a_{\psi_{y,r}})\boldsymbol{D_{y}}_{i,j}I, \quad A_{1,1}^{i,j} = diag(b_{\theta_{yy,r}})\boldsymbol{D_{yy}}_{i,j}\boldsymbol{I} + diag(b_{\theta_{y,r}})\boldsymbol{D_{y}}_{i,j}\boldsymbol{I}.$ Here $\boldsymbol{I}$ and $\boldsymbol{O}$ are the identity and zero matrices respectively, both of size $(N_x+1) \times (N_x+1)$. We impose the boundary conditions as follows:

$$\text{at } x = 0, \quad \boldsymbol{\psi}(x_{N_x}, y_j) = 0, \quad \boldsymbol{\theta}(x_{N_x}, y_j) = 1, \quad \text{at } x = 1, \quad \boldsymbol{\psi}(x_0, y_j) = 0, \quad \boldsymbol{\theta}(x_0, y_j) = 0,$$

$$\text{at } y = 0, \quad \boldsymbol{\psi}(x_i, y_{N_y}) = 0, \quad \sum_{q=0}^{N_y} \boldsymbol{D_y}_{j,q}\boldsymbol{\theta}(x_i, y_{N_y}) = 0,$$

$$\text{at } y = 1, \quad \boldsymbol{\psi}(x_i, y_0) = 0, \quad \sum_{q=0}^{N_y} \boldsymbol{D_y}_{j,q}\boldsymbol{\theta}(x_i, y_0) = 0, \tag{2.29}$$

where 0 and 1 in the y conditions are respectively vectors of zeros and ones of size $1 \times (N_x+1)$.

2.2.2 The multivariate overlapping grid spectral quasilinearization solution

The difference between the MSQLM and MOGSQLM is that for the MOGSQLM we overlap the intervals as we collocate. We first linearize the nonlinear terms using the quasilinearization method then find the solution at the collocation points by approximating the unknown function using Lagrange basis functions.

We first divide the spatial domain $[0, 1]$ into q overlapping equal subintervals

$$\boldsymbol{\Lambda_l} = [x_{l-1}, \bar{x}_l], \quad x_{l-1} < x_l < \bar{x}_l, \quad x_0 = 0, \bar{x}_q = 1, \quad l = 1, 2, ..., q, \tag{2.30}$$

It must be noted that $x_l < \bar{x}_l$ is independent of the overlapping used. The x domain decomposition (2.30) above can be represented in pictorial form as:
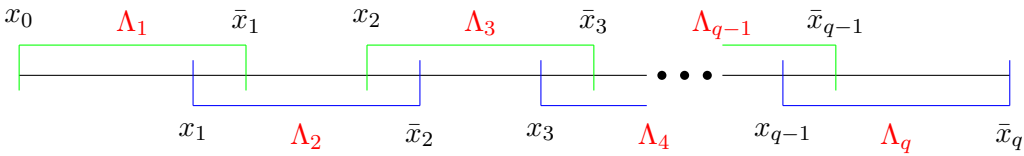
We transform the lth subintervals from the computational domain $[x_{l-1}, \bar{x}_l]$ into $[-1, 1]$ using the linear mapping.

$$\tilde{x}(x) = \frac{2}{\bar{x} - x_{l-1}}\left[x - \frac{1}{2}(\bar{x} + x_{l-1})\right]. \tag{2.31}$$

We further discretize each subinterval Λ_l into $N_x'+1$ Chebyshev-Gauss-Lobatto points $\{\tilde{x}_i\}_{i=0}^{N_x'} = \cos\left(\frac{i\pi}{N_x'}\right)$. We discretize the subintervals so that the last two points in the subinterval Λ_{l-1} overlap with the first two points in the subinterval Λ_l and remain common. To illustrate this consider $N_x' = 5$ which gives:
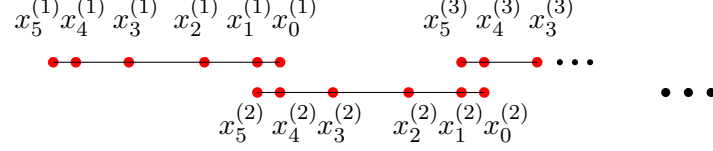
The grid points of the whole domain $[0, 1]$ can be generalised as below:

$$\{0 = x^{(1)}_{N'_x}, ..., x^{(1)}_1 = x^{(2)}_{N'_x}, x^{(1)}_0 = x^{(2)}_{N'_{x-1}}, ..., x^{(l-1)}_1 = x^{(l)}_{N'_x}, x^{(l-1)}_0 = x^{(l)}_{N'_{x-1}}, ..., x^{(q)}_0 = 1\}. \qquad (2.32)$$

We descritize along the y variable in a similar manner. We divide the spatial domain $[0, 1]$ into p overlapping equal subintervals as

$$\boldsymbol{\Gamma_k} = [y_{k-1}, \bar{y}_k], \quad y_{k-1} < y_k < \bar{y}_k, \quad y_0 = 0, \bar{y}_p = 1, \quad k = 1, 2, ..., p. \qquad (2.33)$$

We transform the kth subintervals from the computational domain $[y_{k-1}, \bar{y}_k]$ into $[-1, 1]$ using the following linear mapping.

$$\tilde{y}(y) = \frac{2}{\bar{y} - y_{k-1}} \left[y - \frac{1}{2} (\bar{y} + x_{k-1}) \right]. \qquad (2.34)$$

The grid points in the domain $[0, 1]$ can be generalised as below:

$$\{0 = y^{(1)}_{N'_y}, ..., y^{(1)}_1 = y^{(2)}_{N'_y}, y^{(1)}_0 = y^{(2)}_{N'_{y-1}}, ..., y^{(l-1)}_1 = y^{(l)}_{N'_y}, y^{(l-1)}_0 = y^{(l)}_{N'_{y-1}}, ..., y^{(q)}_0 = 1\}. \qquad (2.35)$$

We express the lengths of each subinterval $L = \bar{x} - x_{l-1}$ and $K = \bar{y} - y_{k-1}$ in terms of q and p the number of subintervals respectively as

$$L = \frac{b - a}{q + (1-q)\left(\frac{1}{2} - \frac{1}{2}\cos\left\{\frac{\pi}{N'_x}\right\}\right)}, \text{ and } K = \frac{d - c}{p + (1-p)\left(\frac{1}{2} - \frac{1}{2}\cos\left\{\frac{\pi}{N'_y}\right\}\right)}. \qquad (2.36)$$

We use the following equations when discritizing to define the overlapping subinterval boundaries:

$$\bar{x} = x_l + L\left(\frac{1}{2} - \frac{1}{2}\cos\left\{\frac{\pi}{N'_x}\right\}\right), \quad \bar{y} = y_k + K\left(\frac{1}{2} - \frac{1}{2}\cos\left\{\frac{\pi}{N'_y}\right\}\right). \qquad (2.37)$$

We assume the solution to be in the form of equation (2.14) with sub-equations defined as in equations (2.15) - (2.16). We first approximate the derivative of the function in the lth subinterval with respect to x.

$$
\begin{aligned}
U_x(x, y_j)|_{x=x_i} &= \sum_{p=0}^{N'_x} \sum_{q=0}^{N'_y} u(x_p, y_q) L_q(y_j) \frac{dL_p(x)}{dx}\bigg|_{x=x_i} \\
&= \sum_{p=0}^{N'_x} D_{xi,p,l} U(x_p, y_j) = \boldsymbol{D_{xl}} \boldsymbol{U}_j,
\end{aligned}
\qquad (2.38)
$$

for $j = 0, 1, ..., N'_y$ and l is the lth subinterval and $l = 1, 2, ..., q$. Now we differentiate with respect to y in the kth subinterval.

$$
\begin{aligned}
U_y(x_i, y)|_{y=y_j} &= \sum_{p=0}^{N'_x} \sum_{q=0}^{N'_y} u(x_p, y_q) L_q(x_i) \frac{dL_p(y)}{dy}\bigg|_{y=y_j} \\
&= \sum_{q=0}^{N'_y} D_{yj,q,k} U(x_i, y_q) = \boldsymbol{D_{yk}} \boldsymbol{U}_i,
\end{aligned}
\qquad (2.39)
$$

for $j = 0, 1, ..., N'_x$ and $k = 1, 2, ..., p$. where $\boldsymbol{D_{xl}} = \dfrac{2}{L}\boldsymbol{\bar{D}_{xl}}$ and $\boldsymbol{D_{yk}} = \dfrac{2}{K}\boldsymbol{\bar{D}_{yk}}$ are the usual Chebyshev differential matrices of sizes $(N'_x{+}1){\times}(N'_x{+}1)$ and $(N'_y{+}1){\times}(N'_y{+}1)$ respectively.

We compute the solution simultaneously in each spatial direction across all subintervals. We begin by constructing the differentiation matrices in both the x and y variables. The final two points of the $(l{-}1)^{th}$ subinterval and the first two points of the lth subinterval overlap and are shared. The rows corresponding to the recurrent grid points are removed, and the Chebyshev differentiation matrix D_x is obtained:

$$\boldsymbol{D_x} = \begin{bmatrix} D_{x0,0,q} & \cdots & D_{x0,N'_x-1,q} & D_{x0,N'_x,q} \\ D_{x1,0,q} & \cdots & D_{x1,N'_x-1,q} & D_{x1,N'_x,q} \\ \ddots & \ddots & \ddots & \ddots \\ D_{xN'_{x-1},0,q} & \cdots & D_{xN_{x-1},N'_{x-1},q} & D_{xN'_{x-1},N'_x,q} \\ & & \ddots & \ddots \\ & & D_{x1,0,2} & D_{x1,1,2} & \cdots & D_{x1,N'_x-1,2} & D_{x1,N'_x,2} \\ & & \ddots & \ddots & \ddots & \ddots & \ddots \\ & & D_{xN'_{x-1},0,2} & D_{xN'_{x-1},1,2} & \cdots & D_{xN'_{x-1},N'_{x-1},2} & D_{xN'_{x-1},N'_x,2} \\ & & & & D_{x1,0,1} & D_{x1,1,1} & \cdots & D_{x1,N'_x,1} \\ & & & & \ddots & \ddots & \cdots & \ddots \\ & & & & D_{xN'_{x-1},0,1} & D_{xN'_{x-1},1,1} & \ddots & D_{xN'_{x-1},N'_x,1} \\ & & & & D_{xN'_x,0,1} & D_{xN'_x,1,1} & \cdots & D_{xN'_x,N'_x,1} \end{bmatrix},$$

Here D_{xq} is the Chebyshev differential matrix in the lth subinterval for the x variable and the empty entries are all zeros. Matrix D_x is of size $(\delta{+}1){\times}(\delta{+}1)$, where $\delta = N'_x{+}(N'_x{-}1){\times}(q{-}1)$ Similarly for the variable y we get the Chebyshev differentiation matrix D_y:

$$\boldsymbol{D_y} = \begin{bmatrix} D_{y0,0,q} & \cdots & D_{y0,N'_y-1,q} & D_{y0,N'_y,q} \\ D_{y1,0,q} & \cdots & D_{y1,N'_y-1,q} & D_{y1,N'_y,q} \\ \ddots & \ddots & \ddots & \ddots \\ D_{yN'_{y-1},0,q} & \cdots & D_{yN'_{x-1},N'_{y-1},q} & D_{yN'_{y-1},N'_y,q} \\ & & \ddots & \ddots \\ & & D_{y1,0,2} & D_{y1,1,2} & \cdots & D_{y1,N'_y-1,2} & D_{y1,N'_y,2} \\ & & \ddots & \ddots & \ddots & \ddots & \ddots \\ & & D_{yN'_{y-1},0,2} & D_{yN'_{y-1},1,2} & \cdots & D_{yN'_{y-1},N'_{y-1},2} & D_{yN'_{y-1},N'_y,2} \\ & & & & D_{y1,0,1} & D_{y1,1,1} & \cdots & D_{y1,N'_y,1} \\ & & & & \ddots & \ddots & \cdots & \ddots \\ & & & & D_{yN'_{y-1},0,1} & D_{yN'_{y-1},1,1} & \ddots & D_{yN'_{y-1},N'_y,1} \\ & & & & D_{yN'_y,0,1} & D_{yN'_y,1,1} & \cdots & D_{yN'_y,N'_y,1} \end{bmatrix},$$

where D_{yp} is the Chebyshev differential matrix in the kth subinterval for the y variable and the empty

entries are all zeros. Matrix D_y is of size $(\sigma+1)\times(\sigma+1)$, where $\sigma = N_y'+(N_y'-1)\times(p-1)$. For higher derivatives

$$\boldsymbol{D_{xx...x}} = (\boldsymbol{D_x})^m, \ \boldsymbol{D_{yy...y}} = (\boldsymbol{D_y})^n$$

and mixed derivatives

$$\boldsymbol{D_{xx...xyy...y}} = (\boldsymbol{D_x})^m (\boldsymbol{D_y})^n,$$

where m and n denote the order of the derivatives.

Equations (2.27) - (2.28) are expressed using the following matrix equations:

$$
\begin{bmatrix}
\begin{bmatrix} A_{0,0}^{0,0} A_{0,1}^{0,0} \\ A_{1,0}^{0,0} A_{1,1}^{0,0} \end{bmatrix} & \begin{bmatrix} A_{0,0}^{0,1} A_{0,1}^{0,1} \\ A_{1,0}^{0,1} A_{1,1}^{0,1} \end{bmatrix} & \cdots & \begin{bmatrix} A_{0,0}^{0,\sigma} A_{0,1}^{0,\sigma} \\ A_{1,0}^{0,\sigma} A_{1,1}^{0,\sigma} \end{bmatrix} \\
\begin{bmatrix} A_{0,0}^{1,0} A_{0,1}^{1,0} \\ A_{1,0}^{1,0} A_{1,1}^{1,0} \end{bmatrix} & \begin{bmatrix} A_{0,0}^{1,1} A_{0,1}^{1,1} \\ A_{1,0}^{1,1} A_{1,1}^{1,1} \end{bmatrix} & \cdots & \begin{bmatrix} A_{0,0}^{1,\sigma} A_{0,1}^{1,\sigma} \\ A_{1,0}^{1,\sigma} A_{1,1}^{1,\sigma} \end{bmatrix} \\
\vdots & \vdots & \ddots & \vdots \\
\vdots & \vdots & \ddots & \vdots \\
\begin{bmatrix} A_{0,0}^{\sigma,0} A_{0,1}^{\sigma,0} \\ A_{1,0}^{\sigma,0} A_{1,1}^{\sigma,0} \end{bmatrix} & \begin{bmatrix} A_{0,0}^{\sigma,1} A_{0,1}^{\sigma,1} \\ A_{1,0}^{\sigma,1} A_{1,1}^{\sigma,1} \end{bmatrix} & \cdots & \begin{bmatrix} A_{0,0}^{\sigma,\sigma} A_{0,1}^{\sigma,\sigma} \\ A_{1,0}^{\sigma,\sigma} A_{1,1}^{\sigma,\sigma} \end{bmatrix}
\end{bmatrix}
\begin{bmatrix}
\begin{bmatrix} \psi_{r+1}^0 \\ \theta_{r+1}^0 \end{bmatrix} \\
\begin{bmatrix} \psi_{r+1}^1 \\ \theta_{r+1}^1 \end{bmatrix} \\
\vdots \\
\vdots \\
\begin{bmatrix} \psi_{r+1}^\sigma \\ \theta_{r+1}^\sigma \end{bmatrix}
\end{bmatrix}
=
\begin{bmatrix}
\begin{bmatrix} R_{\psi,r}^0 \\ R_{\theta,r}^0 \end{bmatrix} \\
\begin{bmatrix} R_{\psi,r}^1 \\ R_{\theta,r}^1 \end{bmatrix} \\
\vdots \\
\vdots \\
\begin{bmatrix} R_{\psi,r}^\sigma \\ R_{\theta,r}^\sigma \end{bmatrix}
\end{bmatrix}.
$$

where for $i = j$

$A_{0,0}^{i,i} = diag(a_{\psi_{xx},r})\boldsymbol{D_{xx}}, \quad A_{0,1}^{i,i} = diag(a_{\theta_x,r})\boldsymbol{D_x},$

$A_{1,0}^{i,i} = diag(b_{\psi_x,r})\boldsymbol{D_x}+diag(a_{\psi_y,r})\boldsymbol{D_{y_{i,i}}}\boldsymbol{I},$

$A_{1,1}^{i,i} = diag(b_{\theta_{xx},r})\boldsymbol{D_{xx}}+diag(b_{\theta_x,r})\boldsymbol{D_x}+diag(b_{\theta_{yy},r})\boldsymbol{D_{yy_{i,i}}}\boldsymbol{I}+diag(b_{\theta_y,r})\boldsymbol{D_{y_{i,i}}}\boldsymbol{I},$ for $i \neq j$

$A_{0,0}^{i,j} = \boldsymbol{O}, \quad A_{0,1}^{i,j} = \boldsymbol{O},$

$A_{1,0}^{i,j} = diag(a_{\psi_y,r})\boldsymbol{D_{y_{i,j}}}I, \quad A_{1,1}^{i,j} = diag(b_{\theta_{yy},r})\boldsymbol{D_{yy_{i,j}}}\boldsymbol{I}+diag(b_{\theta_y,r})\boldsymbol{D_{y_{i,j}}}\boldsymbol{I},$ where $\boldsymbol{I}$ and $\boldsymbol{O}$ are the identity and zero matrices, of size $(\sigma+1)\times(\sigma+1)$. We impose the boundary conditions as in equations (2.29). We calculate the residual errors in the solutions obtained using both the MSQLM and MOGSQLM to get a sense of how close the approximations are to the true solution. We use the infinity norm to calculate the residual error for the system of equations (2.21) - (2.22), namely,

$$\text{res}(\Psi_1) = \max_{x < i < N_x} \|\psi_{xx}+\psi_{yy}+R_a\theta_x\|_\infty, \tag{2.40}$$

$$\text{res}(\Theta_1) = \max_{x < i < N_x} \|\theta_{xx}+\theta_{yy}+\psi_x\theta_y-\psi_y\theta_x\|_\infty. \tag{2.41}$$

We use the norm to compare the convergence of the MSQLM and MOGSQLM techniques. The norm of the iterative error is generally expected to approach zero as the number of iterations increase. The iterative error norm is the size of the vector difference between two successive iterations. We calculate the maximum iterative error norm by using the infinity norm as

$$Error_G = \|G\|_\infty = \max_{x < i < N_x} \|G_{r+1}-G_r\|_\infty, \tag{2.42}$$

where in equations (2.21) - (2.22), G is a general representation of Ψ_1 and Θ_1.

2.3 Results and discussion

In the solution of the flow equations, the values of the Reyleigh number are taken from Malomar et al. [37] except for $R_a = 750$. The value $R_a = 1000$ was found to give poor results for both the MSQLM and MOGSQLM, thus the value of $R_a = 750$ was used. The accuracy of the MSQLM and MOGSQLM deteriorates with increasing Rayleigh numbers.

Figure 2.2 shows the iterative error norm and residual error for different values of the Rayleigh number. Figure 2.2(a) shows the iterative error norm of the temperature with respect to changes in the Rayleigh number for the MSQLM and MOGSQLM. The increase in the Rayleigh number leads to the solutions converging at a higher number of iterations for both the MSQLM and the MOGSQLM. However, both methods converge approximately after five iterations with the MOGSQLM giving a slightly smaller error than the MSQLM. This suggests that the MOGSQLM is only marginally better than the MSQLM in terms of the rate of convergence. As the Rayleigh number values increases it can be seen that the gap between the MSQLM and MOGSQLM narrows significantly. It can be said that for high values of the Rayleigh number the difference in the iterative error norm for the MSQLM and the MOGSQLM is negligible. Figure 2.2(b) illustrates the error in the stream function values. The structure of the error is similar to that in the temperature values. However, for high Rayleigh numbers the MSQLM and the MOGSQLM do not converge at the same iteration. For high Rayleigh numbers the convergence rate of the two methods deteriorates. In Figure 2.2(c) we illustrate the temperature residual error for different values of the Rayleigh number. Increasing the Rayleigh number requires a larger number of iterations to reduce the size of the error for both the MSQLM and the MOGSQLM. The difference in the residual error between the MSQLM and the MOGSQLM decreases when increasing the Rayleigh number. Since the methods converge at the same iteration and the residual error from the MOGSQLM is closer to zero, the MOGSQLM gives a more convergent solution. Figure 2.2(d) shows the structure of the residual error with changes in the Rayleigh number. Smaller constant residual errors are obtained for smaller Rayleigh numbers. The performance of the two methods is indistinguishable.
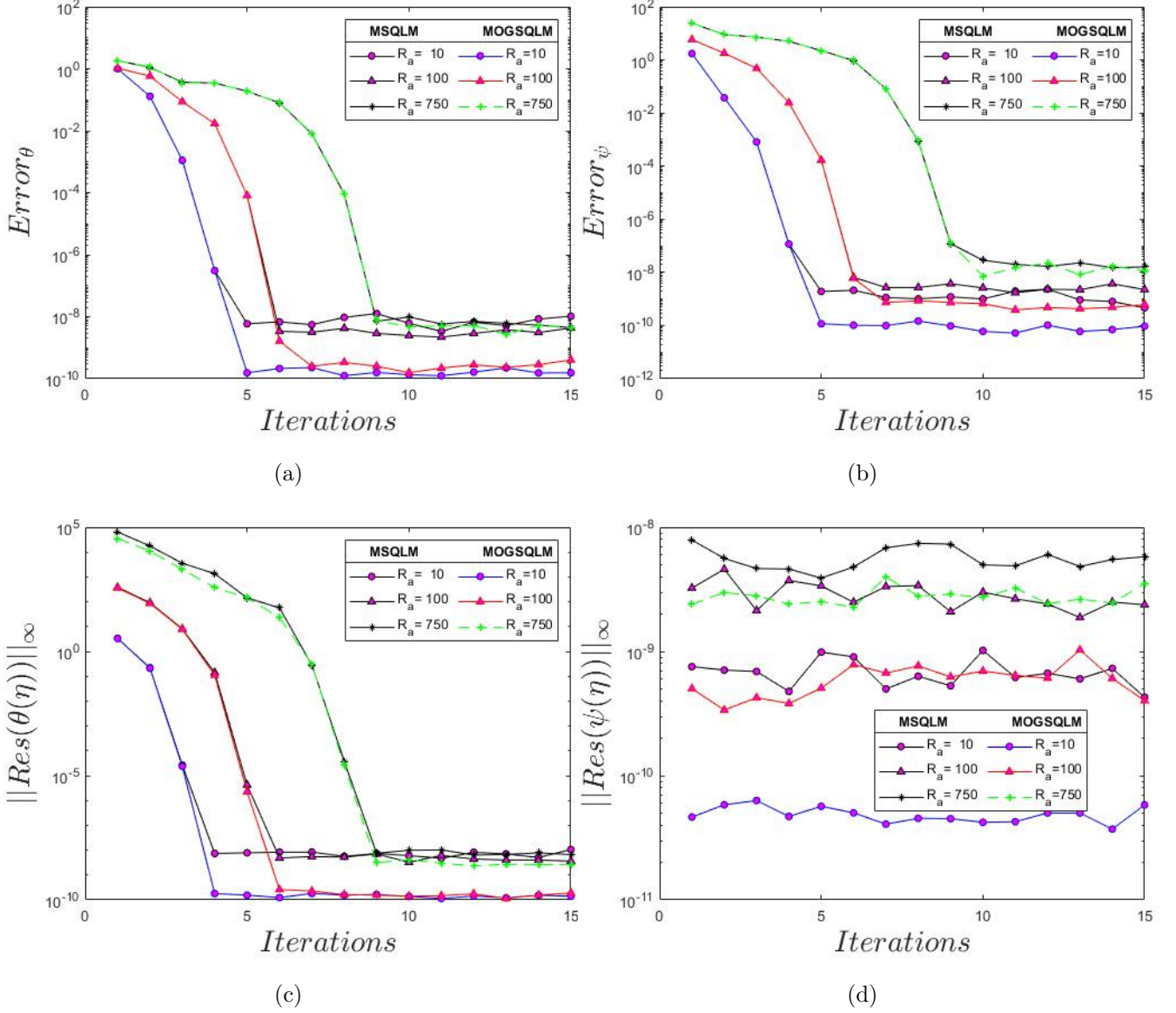
Figure 2.2: The residual error and iterative error norm using the MSQLM and the MOGSQLM with respect to changes in the Rayleigh number

The results in Figure 2.2 show that the errors reduce as the Rayleigh number decreases. This is because moving from high Rayleigh number to low means you are moving from turbulent to laminar flow. turbulent flows are usually unstable, laminar flows are stable. Thus, turbulent flow errors should be high, that corresponds to unstable solutions. The results presented in Tables 2.1 - 2.3 were generated using $R_a = 10$ and show how the change in the number of collocation points affect the error in the results. The MOGSQLM uses $\sigma = N_x' + (N_x' - 1) \times (q-1)$ and $\delta = N_y' + (N_y' - 1) \times (p-1)$ collocation points in the x and y domains respectively. For different values of N_x' and q, we get the same value for σ. Similar for δ, N_y and p. We investigate how N_x', N_y', q and p affect the error. The investigation was performed using a Dell computer with an installed 16 Gb RAM and an Intel(R) processor Core(TM) i7-7700 CPU @ 3.60GHz 3.60 GHz. In Table 2.1 we show how discretizing with 22 collocation points in

both the x and $y-$directions affects the residual error and the iterative error norm. The residual error in the stream function does not change significantly with the MOGSQLM giving a smaller error compared to the MSQLM. The temperature residual error shows a bigger difference in the errors obtained using the MOGSQLM and MSQLM. However, the MOGSQLM gives a smaller residual error. The MOGSQLM results have a smaller residual error for $N_x' = N_y' = 5$, $p = q = 5$ than for $N_x' = N_y' = 6$, $p = q = 4$. This means the MOGSQLM gives better accuracy with more overlapping intervals. The iterative error norm does not seem to change much but the MSQLM has smaller values which mean it converges faster for smaller number of collocation points. For the MOGSQLM most values of $N_x' = N_y' = 5$, $p = q = 5$ are bigger than values of $N_x' = N_y' = 6$, $p = q = 4$. This means less overlapping intervals lead to faster convergence. To achieve both fast convergence and accuracy, a careful selection of the number of the overlapping grid points is important. The CPU times show that the MOGSQLM is faster than the MSQLM. The MOGSQLM converges faster with more overlapping points. Both methods give results that converge to the accurate solution in fractions of seconds. However, the MOGSQLM is the more accurate and faster method compared to the MSQLM.

Table 2.1: Comparison of the MSQLM and MOGSQLM using 22 collocation points in both x and y directions.

				Residual error		
Iter	MSQLM		MOGSQLM			
	$N_x = N_y = 21$		$N_x' = N_y' = 5$, $p = q = 5$		$N_x' = N_y' = 6$, $p = q = 4$	
	res(Ψ_1)	res(Θ_1)	res(Ψ_1)	res(Θ_1)	res(Ψ_1)	res(Θ_1)
1	2.00479e-12	2.14697e+00	1.03029e-12	3.16401e+00	1.57385e-12	3.20218e+00
2	4.43201e-12	2.45599e-02	1.82077e-12	1.68067e-01	2.08722e-12	1.70105e-01
3	2.04281e-12	1.00347e-06	1.00009e-12	2.04413e-05	1.51879e-12	2.15450e-05
4	3.26228e-12	1.28520e-11	1.38023e-12	2.27240e-12	1.32516e-12	3.84084e-12
5	1.82609e-12	1.40697e-11	1.08180e-12	2.46375e-12	1.69464e-12	4.23883e-12
				Solution error		
	$\|\Psi_1\|_\infty$	$\|\Theta_1\|_\infty$	$\|\Psi_1\|_\infty$	$\|\Theta_1\|_\infty$	$\|\Psi_1\|_\infty$	$\|\Theta_1\|_\infty$
1	1.35802e+00	1.00000e+00	1.73113e+00	1.00000e+00	1.73632e+00	1.00000e+00
2	1.67659e-02	4.93788e-02	3.74704e-02	1.29122e-01	3.73605e-02	1.28618e-01
3	1.42759e-04	1.79872e-04	8.10460e-04	1.10600e-03	8.17565e-04	1.11342e-03
4	5.06275e-09	1.45035e-08	1.16610e-07	3.07040e-07	1.15324e-07	3.05385e-07
5	3.29073e-12	6.00719e-12	2.88593e-12	4.43789e-12	1.93475e-12	6.74438e-12
CPU time	0.155977 seconds		0.142997 seconds		0.147875 seconds	

In Table 2.2 we descritized in the x and y domains using 50 collocation points. It can be clearly seen that the residual error obtained using the MOGSQLM is smaller than that obtained using the MSQLM. The results from the MOGSQLM have shown a small difference for $N_x' = N_y' = 7$, $p = q = 8$ and

$N'_x = N'_y = 9$, $p = q = 6$. The results when $N'_x = N'_y = 7$, $p = q = 8$ are closer to zero than when $N'_x = N'_y = 9$, $p = q = 6$ suggest that the methods gives better accuracy when using more overlapping intervals. The iterative error norm obtained using the MOGSQLM is closer to zero than error obtained using the MSQLM. Thus, for large values of collocation points, the MOGSQLM converges faster than the MSQLM. The CPU time confirms that the MOGSQLM is faster than the MSQLM. The CPU time is less for $N'_x = N'_y = 7$, $p = q = 8$ than for $N'_x = N'_y = 9$, $p = q = 6$ suggesting that the MOGSQLM solves the problem faster with more overlapping intervals. The MOGSQLM is found to be accurate with faster convergence.

Table 2.2: Comparison of the MSQLM and MOGSQLM using 50 collocation points in both x and y directions.

Residual error					
Iter	MSQLM		MOGSQLM			
	$N_x = N_y = 49$		$N'_x = N'_y = 7$, $p = q = 8$		$N'_x = N'_y = 9$, $p = q = 6$	
	res(Ψ_1)	res(Θ_1)	res(Ψ_1)	res(Θ_1)	res(Ψ_1)	res(Θ_1)
1	1.33065e-10	2.21339e+00	3.07860e-11	3.31214e+00	4.00551e-11	3.32519e+00
2	3.11676e-10	2.60515e-02	3.52021e-11	2.04608e-01	4.21299e-11	2.08989e-01
3	1.05447e-10	1.09636e-06	2.86970e-11	2.32939e-05	4.03730e-11	2.36660e-05
4	1.71291e-10	9.03451e-10	2.62261e-11	7.15979e-11	2.57039e-11	9.48464e-11
5	1.63233e-10	8.28999e-10	3.45910e-11	8.58830e-11	4.02220e-11	1.18176e-10
Solution error						
	$\|\Psi_1\|_\infty$	$\|\Theta_1\|_\infty$	$\|\Psi_1\|_\infty$	$\|\Theta_1\|_\infty$	$\|\Psi_1\|_\infty$	$\|\Theta_1\|_\infty$
1	1.35781e+00	1.00000e+00	1.73666e+00	1.00000e+00	1.73668e+00	1.00000e+00
2	1.67302e-02	4.95627e-02	3.74879e-02	1.29071e-01	3.74722e-02	1.29040e-01
3	1.43106e-04	1.82492e-04	8.18032e-04	1.11330e-03	8.18058e-04	1.11438e-03
4	5.14355e-09	1.45271e-08	1.17058e-07	3.06363e-07	1.17387e-07	3.06131e-07
5	2.19494e-10	7.60767e-10	4.04565e-11	8.09808e-11	6.00578e-11	1.24634e-10
CPU time	5.284878 seconds		5.061762 seconds		5.221667 seconds	

Table 2.3 illustrates the residual error and the iterative error norm using 110 collocation points in both the x and y domains for the MSQLM and MOGSQLM. The results in Table 2.3 show a trend similar to that observed in Table 2.2. The residual error obtained using the MOGSQLM is smaller than the residual error obtained using the MSQLM. The results using the MOGSQLM show negligible difference for $N'_x = N'_y = 7$, $p = q = 18$ and $N'_x = N'_y = 13$, $p = q = 9$. The MOGSQLM gives better accuracy when more overlapping intervals are used. The CPU time illustrates that the MOGSQLM is a faster method. It can be said that the MOGSQLM is faster with more overlapping intervals.

Table 2.3: Comparison of the MSQLM and MOGSQLM using 110 collocation points in both x and y direction.

Residual error					
Iter	MSQLM		MOGSQLM			
	$N_x = N_y = 109$		$N_x' = N_y' = 7$, $p = q = 18$		$N_x' = N_y' = 13$, $p = q = 9$	
	res(Ψ_1)	res(Θ_1)	res(Ψ_1)	res(Θ_1)	res(Ψ_1)	res(Θ_1)
1	3.54177e-09	2.22730e+00	5.00053e-10	3.34777e+00	1.17634e-09	3.35986e+00
2	1.58086e-08	2.62575e-02	5.02363e-10	2.15508e-01	9.04929e-10	2.18623e-01
3	5.29538e-09	1.10509e-06	8.40648e-10	2.41337e-05	1.14272e-09	2.52463e-05
4	7.43798e-09	6.11176e-08	3.87657e-10	3.89958e-10	9.23069e-10	1.16067e-09
5	4.53026e-09	4.91121e-08	5.92578e-10	4.05308e-10	1.03503e-09	1.60529e-09
Solution error						
	$\|\Psi_1\|_\infty$	$\|\Theta_1\|_\infty$	$\|\Psi_1\|_\infty$	$\|\Theta_1\|_\infty$	$\|\Psi_1\|_\infty$	$\|\Theta_1\|_\infty$
1	1.35809e+00	1.00000e+00	1.73670e+00	1.00000e+00	1.73648e+00	1.00000e+00
2	1.67706e-02	4.95876e-02	3.75657e-02	1.29117e-01	3.75686e-02	1.29110e-01
3	1.43065e-04	1.82528e-04	8.18088e-04	1.11387e-03	8.17795e-04	1.11435e-03
4	1.01870e-08	4.64974e-08	1.17334e-07	3.06484e-07	1.17336e-07	3.06557e-07
5	7.53437e-09	4.33588e-08	5.82569e-10	4.51619e-10	1.26774e-09	1.36081e-09
CPU time	372.853690 seconds		334.621641 seconds		341.675665 seconds	

Figure 2.3 illustrates the minimum number of iterations required for the MSQLM and the MOGSQLM to produce accurate and converged results. The MSQLM and MOGSQLM used four grid points to produce these results. The solution errors for the temperature Figure 2.3(a) and for the stream function Figure 2.3(b) shows that there is negligible difference in the results produced by the MSQLM and the results produced by the MOGSQLM. Also the residual errors for the temperature and stream function Figure 2.3(c) and Figure 2.3(d) respectively show similar results with negligible difference for the MSQLM and the MOGSQLM. The MOGSQLM and the MSQLM converge to an accurate solution on the same iteration. Thus the level of significance is the same on both MSQLM and MOGSQLM.
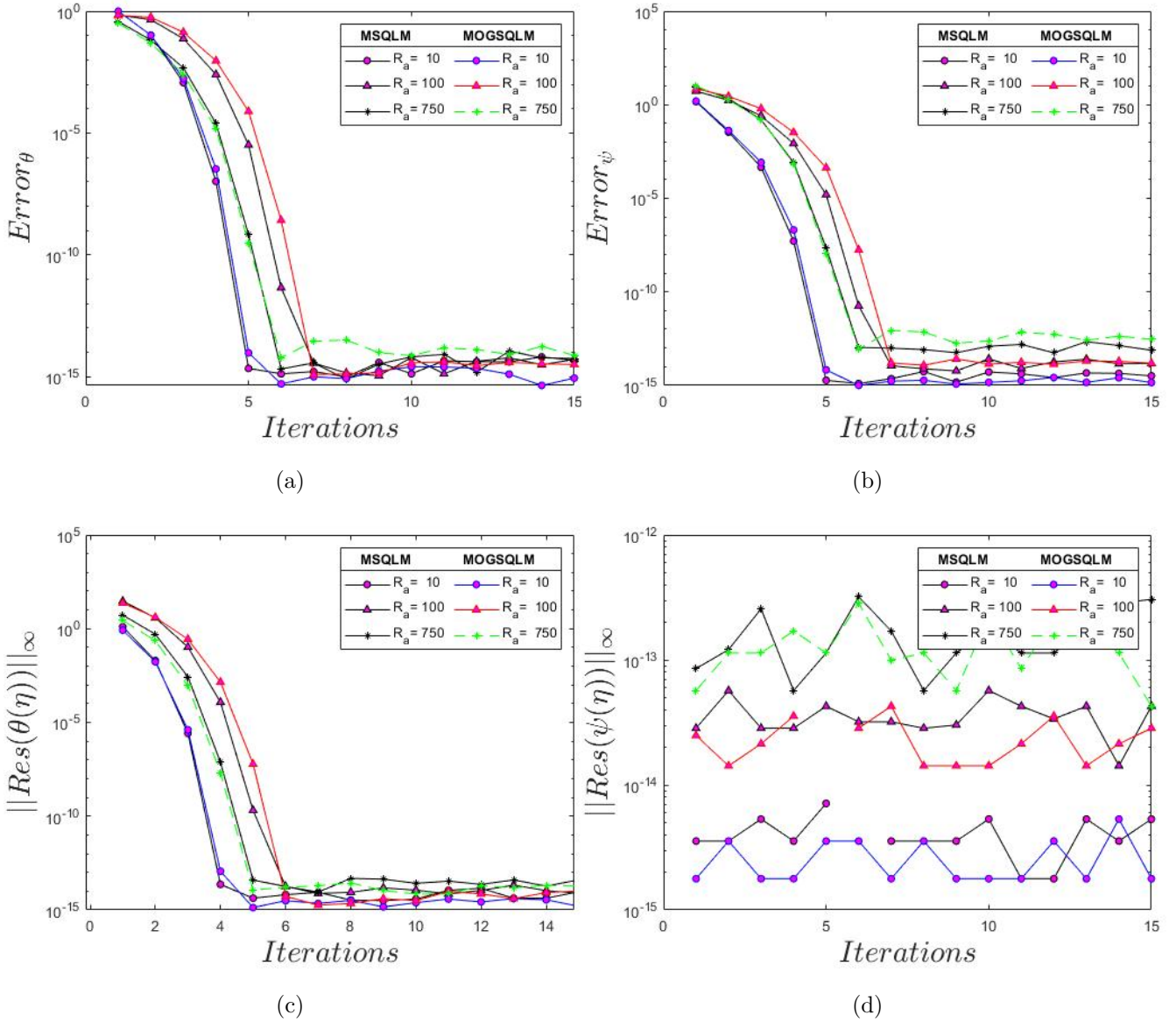
Figure 2.3: The minimum iterations for the residual error and iterative error norm to reduce below 10^{-14} using the MSQLM and the MOGSQLM with respect to changes in the Rayleigh number

Figure 2.4 shows the effect of Rayleigh number on the streamlines and isotherms. The streamlines in Figure 2.4(a) were simulated using the MSQLM. The heated fluid along the left wall moves upward along the hot wall towards the cooled top right corner where the cooled fluid falls to the bottom of the cavity. For small values of the Rayleigh numbers, the flow near the centre of the square cavity is circular and less concentrated compared to the side walls, suggesting less fluid circulation near the center of the cavity. This is explained by the fact that the heated fluid at the side walls is less dense causing the fluid to flow faster near the vertical walls. This type of flow circulation has been observed in literature for heated cavities [21, 22, 24, 35, 37]. For larger Rayleigh numbers, the circulation pattern is elliptic, with a larger middle zone without fluid flow. With large Rayleigh numbers additional circulations are observed and these are more concentrated and cover a larger area of the cavity. This suggests

that the fluid circulation changes with an increase in the Rayleigh number. The strength of the flow circulation increases with the Rayleigh number. This is because increasing the Rayleigh number causes the fluid flow to slow down. Similar discussion on the impact of the Rayleigh number can be found in the literature [7, 22, 37]. Figure 2.4(b) shows results produced using the MOGSQLM. The qualitative results are identical to those in Figure 2.4(a) obtained using the MSQLM suggesting that the method used has no impact on the results.

Figure 2.4(c) shows the isotherms obtained using the MSQLM. These show that for small Rayleigh numbers, the isotherms are nearly uniformly distributed, implying that the temperature of the fluid is nearly constant across the fluid. It is worth noting that as the Rayleigh number increases, the isotherms along the vertical walls are more highly concentrated than those in the center. A high Rayleigh number causes the fluid to slow down while the heat produced by conduction remains constant. Similar results have been found in the literature see [7, 21, 22, 24, 37]. Similar qualitative results can be seen in Figure 2.4(d) where the MOGSQLM was used for simulations.

MSQLM   MOGSQLM

(a)   (b)

(c)   (d)
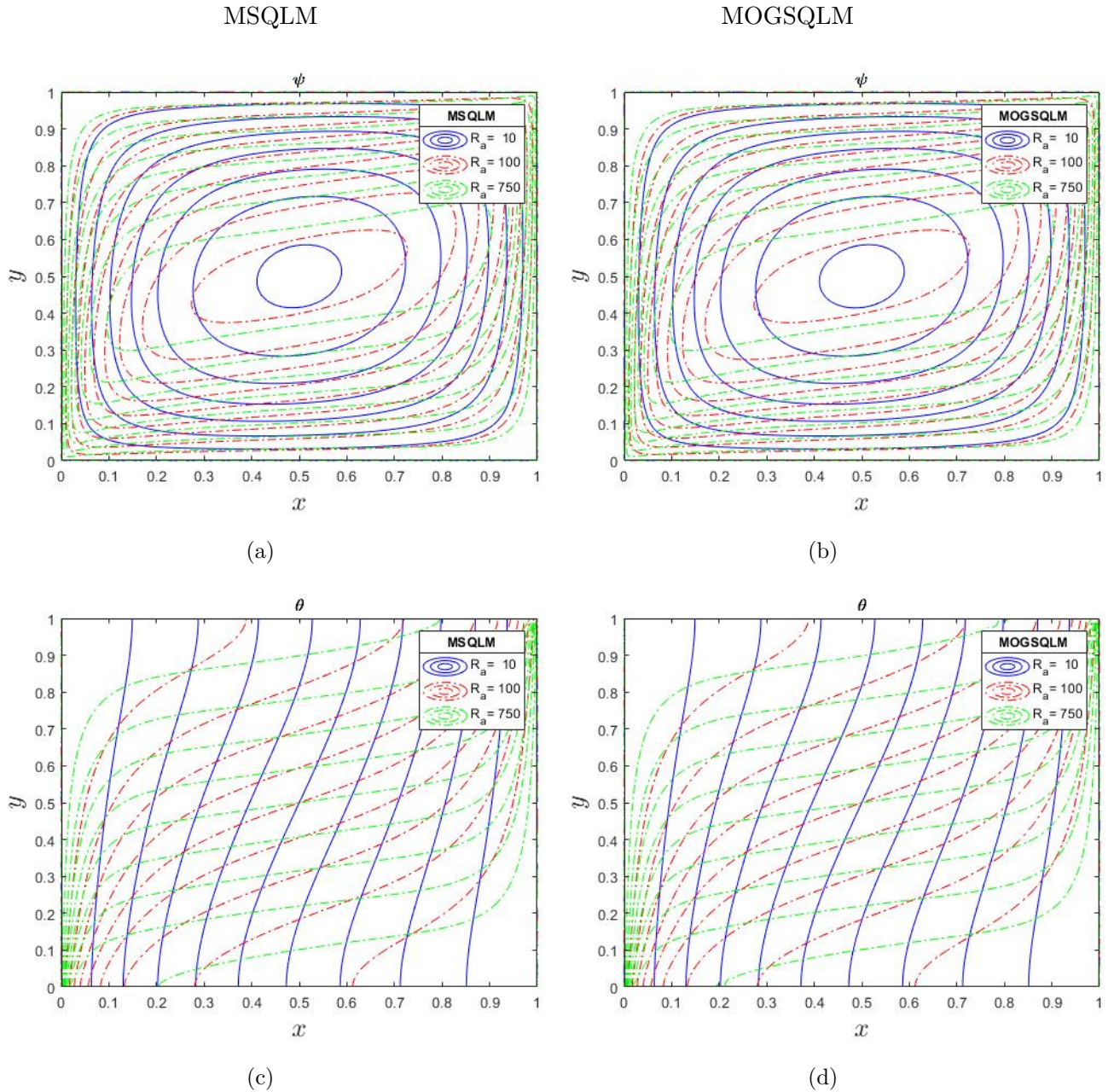
Figure 2.4: The effect of Rayleigh number on a streamlines ((a),(b)) and isotherms((c),(d)) using the MSQLM and MOGSQLM respectively.

Figure 2.5 illustrates the impact of the Rayleigh number on the right side wall skin friction. The skin friction on the right wall is an increasing function of the right side wall height. The increase in the Rayleigh number increases the skin friction and thus the drag force on the flowing fluid increases. This is because the temperature gradient is high at the bottom right wall where the fresh stream of cold flow reaches the hot surface.
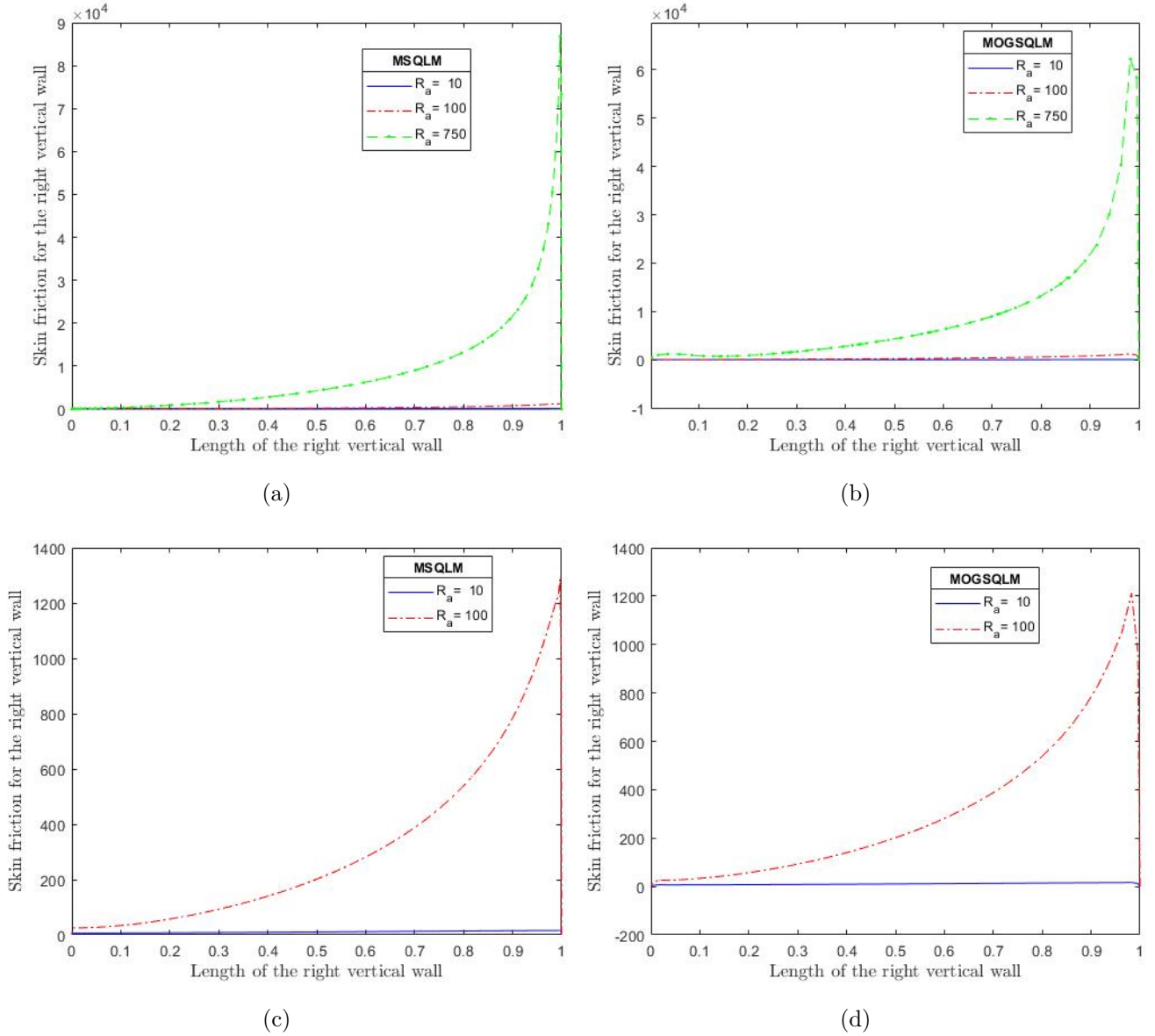
Figure 2.5: The impact of Rayleigh number on skin friction on the right side wall using the MSQLM ((a),(c)) and the MOGSQLM ((b),(d)).

Figure 2.6 shows the skin friction on the left side wall with changes in the Rayleigh number. The skin friction deceases with the length of the left side wall. This is because on the left side wall the flow is hotter near the top part of the wall. The Rayleigh number reduces the skin friction.
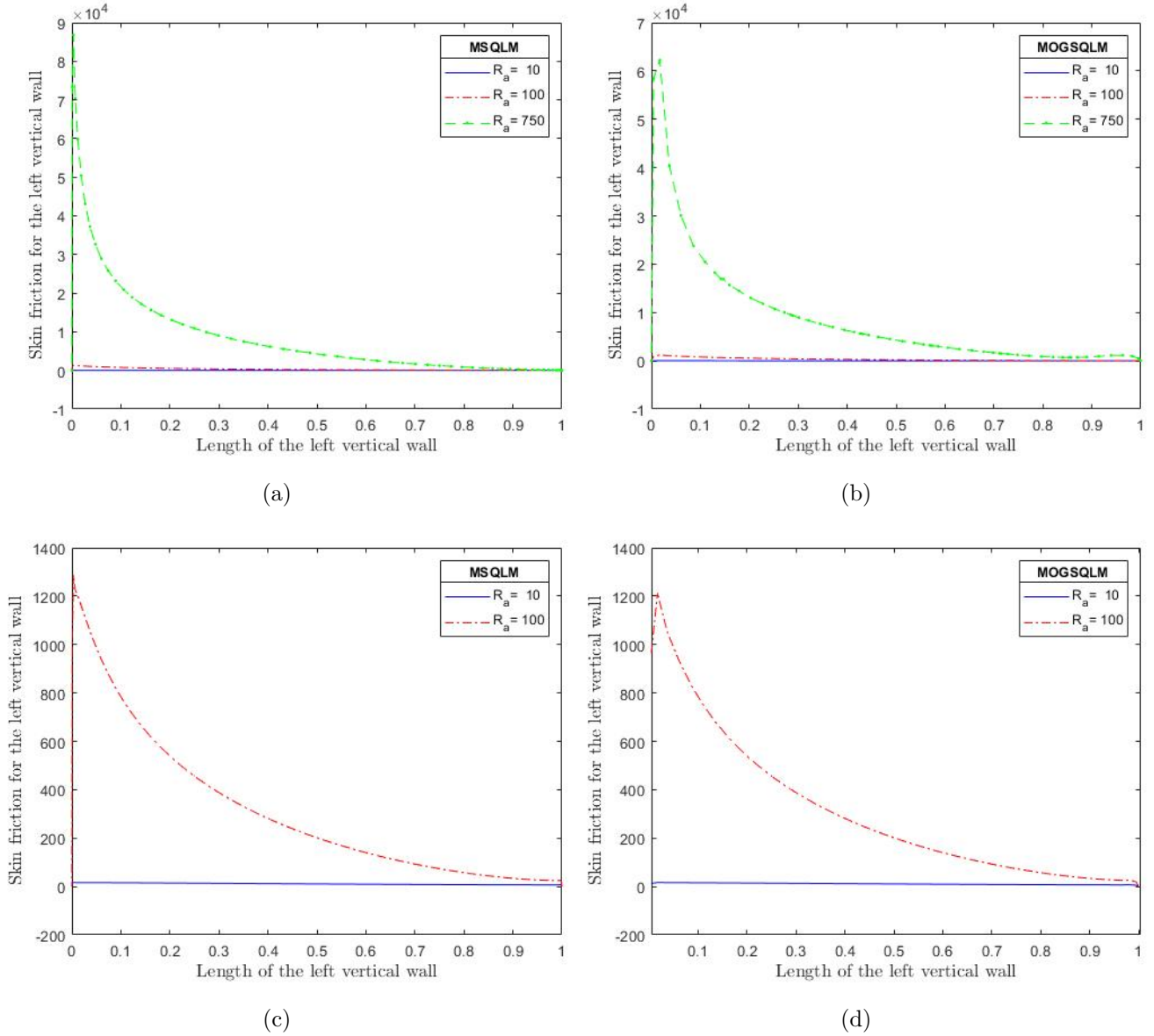
Figure 2.6: The impact of Rayleigh number on skin friction on the left side wall using the MSQLM ((a),(c)) and the MOGSQLM ((b),(d)).

2.4 Summary

Flow in a square cavity with the left side wall heated and the right side wall cooled was investigated using the MSQLM and MOGSQLM to solve the flow equations. The MSQLM and MOGSQLM were both found to be accurate and to converge rapidly to the solution. For the set of equations, the MOGSQLM was shown to perform better than the MSQLM in terms of accuracy, convergence and CPU time. The level of efficiency was found to be the same for both the MSQLM and the MOGSQLM. A higher number of overlapping intervals leds to higher accuracy, faster convergence and reduced time to produce the solution using the MOGSQLM. The increase in the Rayleigh number or collocation points led to an increase in the residual and solution errors. The flow pattern changes from circular to elliptic with an

increase in the central region with no circulation. The flow moves in a clockwise direction. The results are similar to those of Malomar et al. [37] shows that the methods used in this study produced credible results.

Chapter 3

On a porous cavity saturated with a nanofluid

In Chapter 2, we applied the MSQLM and MOGSQLM to the problem of natural convection in a porous square cavity. In this chapter, we use the MSQLM and MOGSQLM to solve a more complex set of equations. We study free convection in a square cavity filled with a porous medium saturated with a nanofluid and subjected to radiation effects and viscous dissipation. In this study, all the cavity walls are stationary with the side walls heated, and the horizontal walls cooled and the bottom wall concentrated. Including a concentration equation adds a layer of complexity not seen in Chapter 2. The effect of parameters such as the Eckert number, Brownian motion parameter and the radiation parameter are investigated.

3.1   Mathematical Formulation

Consider free convective flow of a saturated nanofluid in a porous square cavity of size L. The cavity has vertical walls heated with high constant temperatures T_h, horizontal walls with constant temperatures T_c. The cavity has impermeable, rigid and insulated walls. The physical model and the coordinate system is shown in Figure 3.1. The nanoparticles are well dispersed in the base fluid and the suspension is stable. The fluid emits and absorbs gray light but does not scatter it, and the fluid and medium are in local thermal equilibrium throughout the medium.

The Darcy-Boussinesq approximation and fluid homogeneity are assumed in the porous medium. With the above assumptions the equations of conservation mass, momentum, thermal energy, and nanopar-

ticles, respectively, [24] are

$$\nabla \cdot V = 0, \tag{3.1}$$

$$0 = -\nabla P - \frac{\mu}{k}V + [C\rho_p + (1-C)\rho_{f_0}(1-\beta(T-T_c))]g, \tag{3.2}$$

$$(V \cdot \nabla)T = \alpha_m \nabla^2 T + \delta\left(D_B \nabla C \cdot \nabla T + \frac{D_T}{T_c} \cdot \nabla T\right) - \nabla \cdot q_r + \Phi, \tag{3.3}$$

$$\frac{\partial C}{\partial t} + \frac{1}{\varepsilon}(V \cdot \nabla)C = -\nabla \cdot \left(D_B \nabla C + \frac{D_T}{T_c} \nabla T\right), \tag{3.4}$$

where T is the fluid temperature, ε is porosity of the medium, k is the permeability, V is the Darcy velocity vector, C is the nanoparticle volume fraction, ρ_{f_0} is the reference density of the fluid, t is the time, g is the gravity vector, P is the fluid pressure, D_T is the thermophoretic diffusion coefficient, and D_B is the Brownian diffusion coefficient. In the above equations (3.1-3.4), α_m, ρ_p, μ denote the effective thermal diffusivity of the porous medium, nanoparticle mass density, and the dynamic viscosity, respectively. δ and σ are quantities defined by $\delta = \frac{\varepsilon(\rho C_P)_P}{(\rho C_P)_f}$ and $\sigma = \frac{(\rho C_P)_m}{(\rho C_P)_f}$. C_p is a constant pressure heat capacity, $(\rho C_p)_P$ is effective heat capacity of the nanoparticle material, $(\rho C_p)_f$ is the base fluid heat capacity, $(\rho C_p)_m$ is effective heat capacity of the porous medium, q_r is the radiation flux, β is the coefficient of thermal expansion, and Φ is the viscous dissipation term.
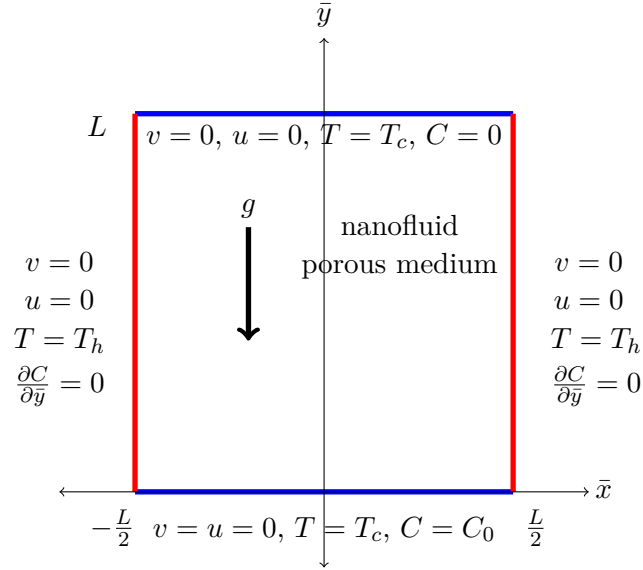

Figure 3.1: The geometry of the problem

It is assumed that the flow is slow if the advective term and the Forchheimer quadratic term do not appear in the momentum equation. We assume the Rosseland approximation for radiation

$$q_r = -\frac{4\sigma_{SB}}{3a_R}\left(\frac{\partial T^4}{\partial \bar{x}} + \frac{\partial T^4}{\partial \bar{y}}\right), \tag{3.5}$$

where a_r represents the Rosseland mean spectral absorption coefficient and σ_{BS} represents Stefan-Boltzmann constant. The term T^4 is expanded in a Taylor series about T_∞ and the higher orders are

neglected to give

$$T^4 \approx 4TT_\infty^3 - 3T_\infty^3. \tag{3.6}$$

The momentum equation (3.2) is differentiated to eliminate the pressure P and thus the equations for the problem can be written as follows:

$$\frac{\partial u}{\partial \bar{x}} + \frac{\partial v}{\partial \bar{y}} = 0, \tag{3.7}$$

$$0 = -\frac{\mu}{K}\left(\frac{\partial u}{\partial \bar{y}} - \frac{\partial v}{\partial \bar{x}}\right) + g(\rho_P - \rho_{f_0})\frac{\partial C}{\partial \bar{x}} - (1-C_0)\rho_{f_0}\beta g \frac{\partial T}{\partial \bar{x}}, \tag{3.8}$$

$$u\frac{\partial T}{\partial \bar{x}} + v\frac{\partial T}{\partial \bar{y}} = \alpha_m\left(\frac{\partial^2 T}{\partial \bar{x}^2} + \frac{\partial^2 T}{\partial \bar{y}^2}\right) + \delta\left\{D_B\left(\frac{\partial C}{\partial \bar{x}}\frac{\partial T}{\partial \bar{x}} + \frac{\partial C}{\partial \bar{y}}\frac{\partial T}{\partial \bar{y}}\right) + \frac{D_T}{T_c}\left[\left(\frac{\partial T}{\partial \bar{x}}\right)^2 + \left(\frac{\partial T}{\partial \bar{y}}\right)^2\right]\right\}$$
$$+ \frac{16\sigma_{SB}T_\infty^3}{3a_R}\left(\frac{\partial^2 T}{\partial \bar{x}^2} + \frac{\partial^2 T}{\partial \bar{y}^2}\right) + \frac{\mu}{K(\rho C_P)_f}\left(u^2 + v^2\right), \tag{3.9}$$

$$\frac{1}{\varepsilon}\left(u\frac{\partial C}{\partial \bar{x}} + v\frac{\partial C}{\partial \bar{y}}\right) = D_B\left(\frac{\partial^2 C}{\partial \bar{x}^2} + \frac{\partial^2 C}{\partial \bar{y}^2}\right) + \frac{D_T}{T_c}\left(\frac{\partial^2 T}{\partial \bar{x}^2} + \frac{\partial^2 T}{\partial \bar{y}^2}\right), \tag{3.10}$$

where u, v denote the velocity components in the $\bar{x}$ and $\bar{y}$ directions. The boundary conditions at the top, bottom, left and right walls are shown in Figure 3.1. The stream function (1.13) is introduced in equations (3.7) - (3.10) to give the following system

$$\frac{\partial^2 \Psi}{\partial \bar{y}^2} + \frac{\partial^2 \Psi}{\partial \bar{x}^2} = -\frac{(1-C_0)\rho_f gK\beta}{\mu}\frac{\partial T}{\partial \bar{x}} + \frac{gK(\rho_p - \rho_f)}{\mu}\frac{\partial C}{\partial \bar{x}}, \tag{3.11}$$

$$\frac{\partial \Psi}{\partial \bar{y}}\frac{\partial T}{\partial \bar{x}} + \frac{\partial \Psi}{\partial \bar{x}}\frac{\partial T}{\partial \bar{y}} = \alpha_m\left(\frac{\partial^2 T}{\partial \bar{x}^2} + \frac{\partial^2 T}{\partial \bar{y}^2}\right) + \delta D_B\left(\frac{\partial C}{\partial \bar{x}}\frac{\partial T}{\partial \bar{x}} + \frac{\partial C}{\partial \bar{y}}\frac{\partial T}{\partial \bar{y}}\right) + \delta\frac{D_T}{T_c}\left(\left(\frac{\partial T}{\partial \bar{x}}\right)^2 + \left(\frac{\partial T}{\partial \bar{y}}\right)^2\right)$$
$$+ \frac{16\sigma_{SB}T_\infty^3}{3\alpha_R}\left(\frac{\partial^2 T}{\partial \bar{x}^2} + \frac{\partial^2 T}{\partial \bar{y}^2}\right) + \frac{\mu}{k(\rho C_p)_f}\left(\left(\frac{\partial \Psi}{\partial \bar{x}}\right)^2 + \left(\frac{\partial \Psi}{\partial \bar{y}}\right)^2\right), \tag{3.12}$$

a layer of complexity not seen in Chapter 2.

$$\frac{\partial \Psi}{\partial \bar{y}}\frac{\partial C}{\partial \bar{x}} + \frac{\partial \Psi}{\partial \bar{x}}\frac{\partial C}{\partial \bar{y}} = D_B\varepsilon\left(\frac{\partial^2 C}{\partial \bar{x}^2} + \frac{\partial^2 C}{\partial \bar{y}^2}\right) + \varepsilon\frac{D_T}{T_c}\left(\frac{\partial^2 T}{\partial \bar{x}^2} + \frac{\partial^2 T}{\partial \bar{y}^2}\right). \tag{3.13}$$

We introduce the non-dimension variable as follows

$$x = \frac{\bar{x}}{l}, \, y = \frac{\bar{y}}{l}, \, \psi = \frac{\Psi}{\alpha_m}, \, \theta = \frac{T-T_c}{\Delta T}, \, \phi = \frac{C}{C_0}, \tag{3.14}$$

where $\Delta T = T_h - T_c$. We substitute the non-dimension variables (3.14) into equations (3.11) - (3.13) and obtain the following equations

$$\frac{\partial^2 \psi}{\partial x^2} + \frac{\partial^2 \psi}{\partial y^2} = -R_a\frac{\partial \theta}{\partial x} + R_a N_r\frac{\partial \phi}{\partial x}, \tag{3.15}$$

$$\frac{\partial \psi}{\partial y}\frac{\partial \theta}{\partial x} - \frac{\partial \psi}{\partial x}\frac{\partial \theta}{\partial y} = \left(1 + \frac{4}{3}N_R\right)\left(\frac{\partial^2 \theta}{\partial x^2} + \frac{\partial^2 \theta}{\partial y^2}\right) + N_b\left(\frac{\partial \phi}{\partial y}\frac{\partial \theta}{\partial x} + \frac{\partial \phi}{\partial x}\frac{\partial \theta}{\partial y}\right) + N_t\left(\left(\frac{\partial \theta}{\partial x}\right)^2 + \left(\frac{\partial \theta}{\partial y}\right)^2\right)$$
$$+ E_c\left(\left(\frac{\partial \psi}{\partial x}\right)^2 + \left(\frac{\partial \psi}{\partial y}\right)^2\right), \tag{3.16}$$

$$\frac{\partial \psi}{\partial y}\frac{\partial \phi}{\partial x} - \frac{\partial \psi}{\partial x}\frac{\partial \phi}{\partial y} = \frac{1}{L_e}\left(\frac{\partial^2 \phi}{\partial x^2} + \frac{\partial^2 \phi}{\partial y^2}\right) + \frac{1}{L_e}\frac{N_t}{N_b}\left(\frac{\partial^2 \theta}{\partial x^2} + \frac{\partial^2 \theta}{\partial y^2}\right), \tag{3.17}$$

where $L_e = \dfrac{\alpha_m}{\varepsilon D_B}$ is the Lewis number, $R_a = \dfrac{(1-C_0)gk\rho_f\beta\Delta TL}{\mu\alpha_m}$ is the porous medium's Rayleigh number, $N_R = \dfrac{4\sigma_s BT_\infty^3}{\alpha_R\alpha_m}$ is the radiation parameter, $E_c = \dfrac{\mu\alpha_m}{k(\rho C_p)_f\Delta T}$ is the porous medium's Eckert number, $N_b = \dfrac{\delta D_B C_0}{\alpha_m}$ is the Brownian motion parameter, $N_r = \dfrac{(\rho_p-\rho_f)C_0}{\rho_f\beta\Delta T(1-C_0)}$ is the buoyancy ratio parameter, and $N_t = \dfrac{\delta D_T\Delta T}{\alpha_m T_c}$ is thermophoresis parameter. The boundary conditions at the left wall, right wall, bottom wall and top wall corresponding to these equations are given respectively by

$$\psi(x,y) = 0,\ \theta(x,y) = 1,\ \frac{\partial\phi(x,y)}{\partial y} = 0,\ \text{at } x = -0.5 \text{ and } x = 0.5,$$

$$\psi(x,y) = 0,\ \theta(x,y) = 0,\ \text{at } y = 0 \text{ and } y = 1,\ \phi(x,0) = 1,\ \phi(x,1) = 0. \tag{3.18}$$

3.2 Numerical solution

In this section we solve equations (3.15) - (3.17) using the MSQLM and MOGSQLM techniques. In Section 3.2.1 we solve using the MSQLM and use the MOGSQLM in Section 3.2.2.

3.2.1 Multivariate spectral quasilinearization solution

The system of equations (3.15) - (3.17) are assigned to variables as below:

$$\Psi_2 = \psi_{xx}+\psi_{yy}+R_a\theta_x-R_aN_r\phi_x = 0, \tag{3.19}$$

$$\Theta_2 = \left(1+\frac{4}{3}N_R\right)(\theta_{xx}+\theta_{yy})+N_b[\phi_x\theta_x+\phi_y\theta_y]+N_t[\theta_x^2+\theta_y^2]+E_c[\psi_x^2+\psi_y^2]-\psi_y\theta_x+\psi_x\theta_y = 0, \tag{3.20}$$

$$\Phi_2 = \frac{1}{l_e}(\phi_{xx}+\phi_{yy})+\frac{1}{l_e}\frac{N_t}{N_b}(\theta_{xx}+\theta_{yy})-\psi_y\phi_x+\psi_x\phi_y = 0. \tag{3.21}$$

The rectangular domain is transformed into the square computational domain $(x,y) \in [-1,1]\times[-1,1]$. Utilizing linear mappings:

$$x = \frac{1}{2}X \quad \text{and} \quad y = \frac{1}{2}(Y+1). \tag{3.22}$$

We linearize equations (3.19)-(3.21) using the quasilinearization method and indicate function evaluations and previous and current iterations by r and $r+1$ respectively. The linearized equations become

$$a_{\psi_{xx},r}\psi_{xx,r+1}+a_{\psi_{yy},r}\psi_{yy,r+1}+a_{\theta_x,r}\theta_{x,r+1}+a_{\phi_x,r}\phi_{x,r+1} = R_{\psi,r}, \tag{3.23}$$

$$b_{\psi_x,r}\psi_{x,r+1}+b_{\psi_y,r}\psi_{y,r+1}+b_{\theta_{xx},r}\theta_{xx,r+1}+b_{\theta_x,r}\theta_{x,r+1}+b_{\theta_{yy},r}\theta_{yy,r+1}+b_{\theta_y,r}\theta_{y,r+1}+b_{\phi_x,r}\phi_{x,r+1}+b_{\phi_y,r}\phi_{y,r+1}$$
$$= R_{\theta,r}, \tag{3.24}$$

$$c_{\psi_x,r}\psi_{x,r+1}+c_{\psi_y,r}\psi_{y,r+1}+c_{\theta_{xx},r}\theta_{xx,r+1}+c_{\theta_{yy},r}\theta_{yy,r+1}+c_{\phi xx,r}\phi_{xx,r+1}+c_{\phi x,r}\phi_{x,r+1}+c_{\phi yy,r}\phi_{yy,r+1}$$
$$+c_{\phi y,r}\phi_{y,r+1} = R_{\phi,r}, \tag{3.25}$$

where

$$a_{\psi_{xx,r}} = \frac{\partial \Psi_2}{\partial \psi_{xx,r}} = 1, \ a_{\psi_{yy,r}} = \frac{\partial \Psi_2}{\partial \psi_{yy,r}} = 1, \ a_{\theta_{x,r}} = \frac{\partial \Psi_2}{\partial \theta_{x,r}} = R_a, \ a_{\phi_{x,r}} = \frac{\partial \Psi_2}{\partial \phi_{x,r}} = -R_a N_r,$$

$$b_{\psi_{x,r}} = \frac{\partial \Theta_2}{\partial \psi_{x,r}} = 2E_c \psi_{x,r} + \theta_{y,r}, \ b_{\psi_{y,r}} = \frac{\partial \Theta_2}{\partial \psi_{y,r}} = 2E_c \psi_{y,r} - \theta_{x,r}, \ b_{\theta_{xx,r}} = \frac{\partial \Theta_2}{\partial \theta_{xx,r}} = 1 + \frac{4}{3} N_R,$$

$$b_{\theta_{x,r}} = \frac{\partial \Theta_2}{\partial \theta_{x,r}} = N_b \phi_{x,r} + 2N_t \theta_{x,r} - \psi_{y,r}, \ b_{\theta_{yy,r}} = \frac{\partial \Theta_2}{\partial \theta_{yy,r}} = 1 + \frac{4}{3} N_R,$$

$$b_{\theta_{y,r}} = \frac{\partial \Theta_2}{\partial \theta_{y,r}} = N_b \phi_{y,r} + 2N_t \theta_{y,r} + \psi_{x,r}, \ b_{\phi_{x,r}} = \frac{\partial \Theta_2}{\partial \phi_{x,r}} = N_b \theta_{x,r}, \ b_{\phi_{y,r}} = \frac{\partial \Theta_2}{\partial \phi_{y,r}} = N_b \theta_{y,r},$$

$$c_{\psi_{x,r}} = \frac{\partial \Phi_2}{\partial \psi_{x,r}} = \psi_{y,r}, \ c_{\psi_{y,r}} = \frac{\partial \Phi_2}{\partial \psi_{y,r}} = -\psi_{x,r}, \ c_{\theta_{xx,r}} = \frac{\partial \Phi_2}{\partial \theta_{xx,r}} = \frac{1}{L_e} \frac{N_t}{N_b}, \ c_{\theta_{yy,r}} = \frac{\partial \Phi_2}{\partial \theta_{yy,r}} = \frac{1}{L_e} \frac{N_t}{N_b},$$

$$c_{\phi_{xx,r}} = \frac{\partial \Phi_2}{\partial \phi_{xx,r}} = \frac{1}{L_e}, \ c_{\phi_{x,r}} = \frac{\partial \Phi_2}{\partial \phi_{x,r}} = -\psi_{y,r}, \ c_{\phi_{yy,r}} = \frac{\partial \Phi_2}{\partial \phi_{yy,r}} = \frac{1}{L_e}, \ c_{\phi_{y,r}} = \frac{\partial \Phi_2}{\partial \phi_{y,r}} = \psi_{x,r},$$

$$R_{\psi,r} = a_{\psi_{xx,r}} \psi_{xx,r} + a_{yy,r} \psi_{yy,r} + a_{\theta_{x,r}} \theta_{x,r} + a_{\phi_{x,r}} \phi_{x,r} - \Psi_2,$$

$$R_{\theta,r} = b_{\psi_{x,r}} \psi_{x,r} + b_{\psi_{y,r}} \psi_{y,r} + b_{\theta_{xx,r}} \theta_{xx,r} + b_{\theta_{x,r}} \theta_{x,r} + b_{\theta_{yy,r}} \theta_{yy,r} + b_{\theta_{y,r}} \theta_{y,r} + b_{\phi_{x,r}} \phi_{x,r} + b_{\phi_{y,r}} \phi_{y,r} - \Theta_2,$$

$$R_{\Phi,r} = c_{\psi_{x,r}} \psi_{x,r} + c_{\psi_{y,r}} \psi_{y,r} + c_{\theta_{xx,r}} \theta_{xx,r} + c_{\theta_{yy,r}} \theta_{yy,r} + c_{\phi_{xx,r}} \phi_{xx,r} + c_{\phi_{x,r}} \phi_{x,r} + c_{\phi_{yy,r}} \phi_{yy,r} + c_{\phi_{y,r}} \phi_{y,r} - \Phi_2.$$

(3.26)

Using a multivariate Lagrange polynomial we rewrite the system of equations (3.23) - (3.25) for application of the spectral collocation method. The equations are rewritten as the following scheme:

$$[diag(a_{\psi_{xx,r}}) \boldsymbol{D_{xx}}] \boldsymbol{\psi}_{r+1}(x_i, y_j) + [diag(a_{\psi_{yy,r}}) \sum_{q=0}^{N_y} \boldsymbol{D_{yy}}_{j,q}] \boldsymbol{\psi}_{r+1}(x_i, y_q) + [diag(a_{\theta_{x,r}}) \boldsymbol{D_x}] \boldsymbol{\theta}_{r+1}(x_i, y_j)$$

$$= \boldsymbol{R}_{\psi,r,j}, \tag{3.27}$$

$$[diag(b_{\psi_{x,r}}) \boldsymbol{D_x}] \boldsymbol{\psi}_{r+1}(x_i, y_j) + [diag(b_{\psi_{y,r}}) \sum_{q=0}^{N_y} \boldsymbol{D_y}_{j,q}] \boldsymbol{\psi}_{r+1}(x_i, y_q) + [diag(b_{\theta_{xx,r}}) \boldsymbol{D_{xx}}$$

$$+ diag(b_{\theta_{x,r}}) \boldsymbol{D_x}] \boldsymbol{\theta}_{r+1}(x_i, y_j) + [diag(b_{\theta_{yy,r}}) \sum_{q=0}^{N_y} \boldsymbol{D_{yy}}_{j,q} + diag(b_{\theta_{y,r}}) \sum_{q=0}^{N_y} \boldsymbol{D_y}_{j,q}] \boldsymbol{\theta}_{r+1}(x_i, y_q)$$

$$+ [diag(b_{\phi_{xx,r}}) \boldsymbol{D_{xx}}] \boldsymbol{\phi}_{r+1}(x_i, y_j) + [diag(b_{\phi_{y,r}}) \sum_{q=0}^{N_y} \boldsymbol{D_y}_{j,q}] \boldsymbol{\phi}(x_i, y_q) = \boldsymbol{R}_{\theta,r,j}, \tag{3.28}$$

$$[diag(c_{\psi_{x,r}}) \boldsymbol{D_x}] \boldsymbol{\psi}_{r+1}(x_i, y_j) + [diag(c_{\psi_{y,r}}) \sum_{q=0}^{N_y} \boldsymbol{D_y}_{j,q}] \boldsymbol{\psi}_{r+1}(x_i, y_q) + [diag(c_{\theta_{xx,r}}) \boldsymbol{D_{xx}}] \boldsymbol{\theta}_{r+1}(x_i, y_j)$$

$$+ [diag(c_{\theta_{yy,r}}) \sum_{q=0}^{N_y} \boldsymbol{D_{yy}}_{j,q}] \boldsymbol{\theta}_{r+1}(x_i, y_q) + [diag(c_{\phi_{xx,r}}) \boldsymbol{D_{xx}} + diag(c_{\phi_{x,r}}) \boldsymbol{D_x}] \boldsymbol{\phi}_{r+1}(x_i, y_j)$$

$$+ [diag(c_{\phi_{yy,r}}) \sum_{q=0}^{N_y} \boldsymbol{D_{yy}}_{j,q} + diag(c_{\phi_{y,r}}) \sum_{q=0}^{N_y} \boldsymbol{D_y}_{j,q}] \boldsymbol{\phi}_{r+1}(x_i, y_q) = \boldsymbol{R}_{\phi,r,j}, \tag{3.29}$$

where the vectors $\boldsymbol{R}_{\psi,r,j}$, $\boldsymbol{R}_{\theta,r,j}$ and $\boldsymbol{R}_{\phi,r,j}$ are $\boldsymbol{R}_{\psi,r}$, $\boldsymbol{R}_{\theta,r}$ and $\boldsymbol{R}_{\phi,r}$ are defined for each y_j for $j = 0, 1, ..., N_y$. Equations (3.27) - (3.29) are then expressed using the following matrix:

$$\begin{bmatrix} \begin{bmatrix} A_{0,0}^{0,0} A_{0,1}^{0,0} A_{0,2}^{0,0} \\ A_{1,0}^{0,0} A_{1,1}^{0,0} A_{1,2}^{0,0} \\ A_{2,0}^{0,0} A_{2,1}^{0,0} A_{2,2}^{0,0} \end{bmatrix} & \begin{bmatrix} A_{0,0}^{0,1} A_{0,1}^{0,1} A_{0,2}^{0,1} \\ A_{1,0}^{0,1} A_{1,1}^{0,1} A_{1,2}^{0,1} \\ A_{2,0}^{0,1} A_{2,1}^{0,1} A_{2,2}^{0,1} \end{bmatrix} & \cdots & \begin{bmatrix} A_{0,0}^{0,N_y} A_{0,1}^{0,N_y} A_{0,2}^{0,N_y} \\ A_{1,0}^{0,N_y} A_{1,1}^{0,N_y} A_{1,2}^{0,N_y} \\ A_{2,0}^{0,N_y} A_{2,1}^{0,N_y} A_{2,2}^{0,N_y} \end{bmatrix} \\ \begin{bmatrix} A_{0,0}^{1,0} A_{0,1}^{1,0} A_{0,2}^{1,0} \\ A_{1,0}^{1,0} A_{1,1}^{1,0} A_{1,2}^{1,0} \\ A_{2,0}^{1,0} A_{2,1}^{1,0} A_{2,2}^{1,0} \end{bmatrix} & \begin{bmatrix} A_{0,0}^{1,1} A_{0,1}^{1,1} A_{0,2}^{1,1} \\ A_{1,0}^{1,1} A_{1,1}^{1,1} A_{1,2}^{1,1} \\ A_{2,0}^{1,1} A_{2,1}^{1,1} A_{2,2}^{1,1} \end{bmatrix} & \cdots & \begin{bmatrix} A_{0,0}^{1,N_y} A_{0,1}^{1,N_y} A_{0,2}^{1,N_y} \\ A_{1,0}^{1,N_y} A_{1,1}^{1,N_y} A_{1,2}^{1,N_y} \\ A_{2,0}^{1,N_y} A_{2,1}^{1,N_y} A_{2,2}^{1,N_y} \end{bmatrix} \\ \vdots & \vdots & \ddots & \vdots \\ \vdots & \vdots & \ddots & \vdots \\ \begin{bmatrix} A_{0,0}^{N_y,0} A_{0,1}^{N_y,0} A_{0,2}^{N_y,0} \\ A_{1,0}^{N_y,0} A_{1,1}^{N_y,0} A_{1,2}^{N_y,0} \\ A_{2,0}^{N_y,0} A_{2,1}^{N_y,0} A_{2,2}^{N_y,0} \end{bmatrix} & \begin{bmatrix} A_{0,0}^{N_y,1} A_{0,1}^{N_y,1} A_{0,2}^{N_y,1} \\ A_{1,0}^{N_y,1} A_{1,1}^{N_y,1} A_{1,2}^{N_y,1} \\ A_{2,0}^{N_y,1} A_{2,1}^{N_y,1} A_{2,2}^{N_y,1} \end{bmatrix} & \cdots & \begin{bmatrix} A_{0,0}^{N_y,N_y} A_{0,1}^{N_y,N_y} A_{0,2}^{N_y,N_y} \\ A_{1,0}^{N_y,N_y} A_{1,1}^{N_y,N_y} A_{1,2}^{N_y,N_y} \\ A_{2,0}^{N_y,N_y} A_{2,1}^{N_y,N_y} A_{2,2}^{N_y,N_y} \end{bmatrix} \end{bmatrix} \begin{bmatrix} \psi_{r+1}^0 \\ \theta_{r+1}^0 \\ \phi_{r+1}^0 \\ \psi_{r+1}^1 \\ \theta_{r+1}^1 \\ \phi_{r+1}^1 \\ \vdots \\ \vdots \\ \psi_{r+1}^{N_y} \\ \theta_{r+1}^{N_y} \\ \phi_{r+1}^{N_y} \end{bmatrix} = \begin{bmatrix} R_{\psi,r}^0 \\ R_{\theta,r}^0 \\ R_{\phi,r}^0 \\ R_{\psi,r}^1 \\ R_{\theta,r}^1 \\ R_{\phi,r}^1 \\ \vdots \\ \vdots \\ R_{\psi,r}^{N_y} \\ R_{\theta,r}^{N_y} \\ R_{\phi,r}^{N_y} \end{bmatrix},$$

where for $i = j$

$A_{0,0}^{i,i} = diag(a_{\psi_{xx},r})\boldsymbol{D_{xx}} + diag(a_{\psi_{yy},r})\boldsymbol{D_{yy}}_{i,i}\boldsymbol{I}, \quad A_{0,1}^{i,i} = diag(a_{\theta_x,r})\boldsymbol{D_x}, \quad A_{0,2}^{i,i} = diag(a_{\phi_x,r})\boldsymbol{D_x},$

$A_{1,0}^{i,i} = diag(b_{\psi_x,r})\boldsymbol{D_x} + diag(a_{\psi_y,r})\boldsymbol{D_y}_{i,i}\boldsymbol{I}, \quad A_{1,1}^{i,i} = diag(b_{\theta_{xx},r})\boldsymbol{D_{xx}} + diag(b_{\theta_x,r})\boldsymbol{D_x} +$

$diag(b_{\theta_{yy},r})\boldsymbol{D_{yy}}_{i,i}\boldsymbol{I} + diag(b_{\theta_y,r})\boldsymbol{D_y}_{i,i}\boldsymbol{I}, \quad A_{1,2}^{i,i} = diag(b_{\phi_x,r})\boldsymbol{D_x} + diag(a_{\phi_y,r})\boldsymbol{D_y}_{i,i}\boldsymbol{I},$

$A_{2,0}^{i,i} = diag(c_{\psi_x,r})\boldsymbol{D_x} + diag(c_{\psi_y,r})\boldsymbol{D_y}_{i,i}\boldsymbol{I}, \quad A_{2,1}^{i,i} = diag(c_{\theta_x,r})\boldsymbol{D_x} + diag(c_{\theta_y,r})\boldsymbol{D_y}_{i,i}\boldsymbol{I},$

$A_{2,2}^{i,i} = diag(c_{\phi_{xx},r})\boldsymbol{D_{xx}} + diag(c_{\phi_x,r})\boldsymbol{D_x} + diag(c_{\phi_{yy},r})\boldsymbol{D_{yy}}_{i,i}\boldsymbol{I} + diag(c_{\phi_y,r})\boldsymbol{D_y}_{i,i}\boldsymbol{I}$

For $i \neq j$

$A_{0,0}^{i,j} = diag(a_{\psi_{yy},r})\boldsymbol{D_{yy}}_{i,j}\boldsymbol{I}, \quad A_{0,1}^{i,i} = \boldsymbol{O}, \quad A_{0,2}^{i,i} = \boldsymbol{O},$

$A_{1,0}^{i,j} = diag(a_{\psi_y,r})\boldsymbol{D_y}_{i,j}\boldsymbol{I}, \quad A_{1,1}^{i,j} = diag(b_{\theta_{yy},r})\boldsymbol{D_{yy}}_{i,j}\boldsymbol{I} + diag(b_{\theta_y,r})\boldsymbol{D_y}_{i,j}\boldsymbol{I}, \quad A_{1,2}^{i,j} = diag(a_{\phi_y,r})\boldsymbol{D_y}_{i,j}\boldsymbol{I},$

$A_{2,0}^{i,j} = diag(c_{\psi_y,r})\boldsymbol{D_y}_{i,j}\boldsymbol{I}, \quad A_{2,1}^{i,j} = diag(c_{\theta_y,r})\boldsymbol{D_y}_{i,j}\boldsymbol{I}, \quad A_{2,2}^{i,j} = diag(c_{\phi_{yy},r})\boldsymbol{D_{yy}}_{i,j}\boldsymbol{I} + diag(c_{\phi_y,r})\boldsymbol{D_y}_{i,j}\boldsymbol{I},$

where $\boldsymbol{I}$ and $\boldsymbol{O}$ are identity matrix and zero matrix respectively, both of size $(N_x+1) \times (N_x+1)$. We now impose the boundary conditions accordingly as follows:

$$\text{at } x = -0.5, \quad \boldsymbol{\psi}(x_{N_x}, y_j) = 0, \quad \boldsymbol{\theta}(x_{N_x}, y_j) = 1, \sum_{q=0}^{N_y} \boldsymbol{D_y}_{j,q}\phi(x_{N_x}, y_j) = 0,$$

$$\text{at } x = 0.5, \quad \boldsymbol{\psi}(x_0, y_j) = 0, \quad \boldsymbol{\theta}(x_0, y_j) = 1, \quad \sum_{q=0}^{N_y} \boldsymbol{D_y}_{j,q}\phi(x_0, y_j) = 0, \qquad (3.30)$$

$$\text{at } y = 0, \quad \boldsymbol{\psi}(x_i, y_{N_y}) = 0, \quad \boldsymbol{\theta}(x_i, y_{N_y}) = 0, \quad \boldsymbol{\phi}(x_i, y_{N_y}) = 1,$$

$$\text{at } y = 1, \quad \boldsymbol{\psi}(x_i, y_0) = 0, \quad \boldsymbol{\theta}(x_i, y_0) = 0, \quad \boldsymbol{\phi}(x_i, y_0) = 0,$$

where 0 and 1 in the conditions are respectively vectors of zeros and ones of size $(N_x+1) \times 1$.

3.2.2 Multivariate overlapping grid spectral quasilinearization solution

The system of equations (3.19) - (3.21) are solved using the multivariate overlapping spectral quasilinearization method. In light of the fact that we are dealing with the same equation as in Section 3.2.1 the linearization is similar to equations (3.23) - (3.25) and equations (3.27) - (3.29). Equations (3.27) - (3.29) are then expressed in the following matrix form:

$$
\begin{bmatrix}
\begin{bmatrix} A_{0,0}^{0,0} A_{0,1}^{0,0} A_{0,2}^{0,0} \\ A_{1,0}^{0,0} A_{1,1}^{0,0} A_{1,2}^{0,0} \\ A_{2,0}^{0,0} A_{2,1}^{0,0} A_{2,2}^{0,0} \end{bmatrix} & \begin{bmatrix} A_{0,0}^{0,1} A_{0,1}^{0,1} A_{0,2}^{0,1} \\ A_{1,0}^{0,1} A_{1,1}^{0,1} A_{1,2}^{0,1} \\ A_{2,0}^{0,1} A_{2,1}^{0,1} A_{2,2}^{0,1} \end{bmatrix} & \cdots & \begin{bmatrix} A_{0,0}^{0,\sigma} A_{0,1}^{0,\sigma} A_{0,2}^{0,\sigma} \\ A_{1,0}^{0,\sigma} A_{1,1}^{0,\sigma} A_{1,2}^{0,\sigma} \\ A_{2,0}^{0,\sigma} A_{2,1}^{0,\sigma} A_{2,2}^{0,\sigma} \end{bmatrix} \\
\begin{bmatrix} A_{0,0}^{1,0} A_{0,1}^{1,0} A_{0,2}^{1,0} \\ A_{1,0}^{1,0} A_{1,1}^{1,0} A_{1,2}^{1,0} \\ A_{2,0}^{1,0} A_{2,1}^{1,0} A_{2,2}^{1,0} \end{bmatrix} & \begin{bmatrix} A_{0,0}^{1,1} A_{0,1}^{1,1} A_{0,2}^{1,1} \\ A_{1,0}^{1,1} A_{1,1}^{1,1} A_{1,2}^{1,1} \\ A_{2,0}^{1,1} A_{2,1}^{1,1} A_{2,2}^{1,1} \end{bmatrix} & \cdots & \begin{bmatrix} A_{0,0}^{1,\sigma} A_{0,1}^{1,\sigma} A_{0,2}^{1,\sigma} \\ A_{1,0}^{1,\sigma} A_{1,1}^{1,\sigma} A_{1,2}^{1,\sigma} \\ A_{2,0}^{1,\sigma} A_{2,1}^{1,\sigma} A_{2,2}^{1,\sigma} \end{bmatrix} \\
\vdots & \vdots & \ddots & \vdots \\
\vdots & \vdots & \ddots & \vdots \\
\begin{bmatrix} A_{0,0}^{\sigma,0} A_{0,1}^{\sigma,0} A_{0,2}^{\sigma,0} \\ A_{1,0}^{\sigma,0} A_{1,1}^{\sigma,0} A_{1,2}^{\sigma,0} \\ A_{2,0}^{\sigma,0} A_{2,1}^{\sigma,0} A_{2,2}^{\sigma,0} \end{bmatrix} & \begin{bmatrix} A_{0,0}^{\sigma,1} A_{0,1}^{\sigma,1} A_{0,2}^{\sigma,1} \\ A_{1,0}^{\sigma,1} A_{1,1}^{\sigma,1} A_{1,2}^{\sigma,1} \\ A_{2,0}^{\sigma,1} A_{2,1}^{\sigma,1} A_{2,2}^{\sigma,1} \end{bmatrix} & \cdots & \begin{bmatrix} A_{0,0}^{\sigma,\sigma} A_{0,1}^{\sigma,\sigma} A_{0,2}^{\sigma,\sigma} \\ A_{1,0}^{\sigma,\sigma} A_{1,1}^{\sigma,\sigma} A_{1,2}^{\sigma,\sigma} \\ A_{2,0}^{\sigma,\sigma} A_{2,1}^{\sigma,\sigma} A_{2,2}^{\sigma,\sigma} \end{bmatrix}
\end{bmatrix}
\begin{bmatrix}
\begin{bmatrix} \psi_{r+1}^0 \\ \theta_{r+1}^0 \\ \phi_{r+1}^0 \end{bmatrix} \\
\begin{bmatrix} \psi_{r+1}^1 \\ \theta_{r+1}^1 \\ \phi_{r+1}^1 \end{bmatrix} \\
\vdots \\
\vdots \\
\begin{bmatrix} \psi_{r+1}^\sigma \\ \theta_{r+1}^\sigma \\ \phi_{r+1}^\sigma \end{bmatrix}
\end{bmatrix}
=
\begin{bmatrix}
\begin{bmatrix} R_{\psi,r}^0 \\ R_{\theta,r}^0 \\ R_{\phi,r}^0 \end{bmatrix} \\
\begin{bmatrix} R_{\psi,r}^1 \\ R_{\theta,r}^1 \\ R_{\phi,r}^1 \end{bmatrix} \\
\vdots \\
\vdots \\
\begin{bmatrix} R_{\psi,r}^\sigma \\ R_{\theta,r}^\sigma \\ R_{\phi,r}^\sigma \end{bmatrix}
\end{bmatrix}
$$

where for $i = j$

$A_{0,0}^{i,i} = diag(a_{\psi_{xx},r})\boldsymbol{D_{xx}} + diag(a_{\psi_{yy},r})\boldsymbol{D_{yy}}_{i,i}\boldsymbol{I}, \quad A_{0,1}^{i,i} = diag(a_{\theta_x,r})\boldsymbol{D_x}, \ A_{0,2}^{i,i} = diag(a_{\phi_x,r})\boldsymbol{D_x},$

$A_{1,0}^{i,i} = diag(b_{\psi_x,r})\boldsymbol{D_x} + diag(a_{\psi_y,r})\boldsymbol{D_y}_{i,i}\boldsymbol{I}, \ A_{1,1}^{i,i} = diag(b_{\theta_{xx},r})\boldsymbol{D_{xx}} + diag(b_{\theta_x,r})\boldsymbol{D_x} +$

$diag(b_{\theta_{yy},r})\boldsymbol{D_{yy}}_{i,i}\boldsymbol{I} + diag(b_{\theta_y,r})\boldsymbol{D_y}_{i,i}\boldsymbol{I}, \ A_{1,2}^{i,i} = diag(b_{\phi_x,r})\boldsymbol{D_x} + diag(a_{\phi_y,r})\boldsymbol{D_y}_{i,i}I,$

$A_{2,0}^{i,i} = diag(c_{\psi_x,r})\boldsymbol{D_x} + diag(c_{\psi_y,r})\boldsymbol{D_y}_{i,i}\boldsymbol{I}, \ A_{2,1}^{i,i} = diag(c_{\theta_x,r})\boldsymbol{D_x} + diag(c_{\theta_y,r})\boldsymbol{D_y}_{i,i}\boldsymbol{I},$

$A_{2,2}^{i,i} = diag(c_{\phi_{xx},r})\boldsymbol{D_{xx}} + diag(c_{\phi_x,r})\boldsymbol{D_x} + diag(c_{\phi_{yy},r})\boldsymbol{D_{yy}}_{i,i}\boldsymbol{I} + diag(c_{\phi_y,r})\boldsymbol{D_y}_{i,i}\boldsymbol{I}.$

For $i \neq j$

$A_{0,0}^{i,j} = diag(a_{\psi_{yy},r})\boldsymbol{D_{yy}}_{i,j}\boldsymbol{I}, \ A_{0,1}^{i,j} = \boldsymbol{O}, \ A_{0,2}^{i,i} = \boldsymbol{O},$

$A_{1,0}^{i,j} = diag(a_{\psi_y,r})\boldsymbol{D_y}_{i,j}\boldsymbol{I}, \ A_{1,1}^{i,j} = diag(b_{\theta_{yy},r})\boldsymbol{D_{yy}}_{i,j}\boldsymbol{I} + diag(b_{\theta_y,r})\boldsymbol{D_y}_{i,j}\boldsymbol{I}, \ A_{1,2}^{i,j} = diag(a_{\phi_y,r})\boldsymbol{D_y}_{i,j}\boldsymbol{I},$

$A_{2,0}^{i,j} = diag(c_{\psi_y,r})\boldsymbol{D_y}_{i,j}\boldsymbol{I}, \ A_{2,1}^{i,j} = diag(c_{\theta_y,r})\boldsymbol{D_y}_{i,j}\boldsymbol{I}, \ A_{2,2}^{i,j} = diag(c_{\phi_{yy},r})\boldsymbol{D_{yy}}_{i,j}\boldsymbol{I} + diag(c_{\phi_y,r})\boldsymbol{D_y}_{i,j}\boldsymbol{I}.$

where $\boldsymbol{I}$ and $\boldsymbol{O}$ are identity matrix and zero matrix respectively, both of size $(N'_x+1)\times(N'_x+1)$.

3.3 Results and discussion

The equations for the cavity flow were solved numerically using the MSQLM and MOGSQLM. Here we illustrate and analyse the result. In this study we used the constant parameters $N_t = 0.25$, $N_r = 0.1$, $N_R = 0.25$, $N_b = 0.1$, $E_c = 0.005$, $R_a = 50$ and $L_e = 1.2$ unless otherwise stated. The parameters were taken from the study by Goqo et al. [7].

Figure 3.2 shows the solution error in the stream function, temperature and concentration with changes in the Eckert number. The Figure gives a comparison of the performance of the two methods, namely, the MSQLM and MOGSQLM. Figure 3.2(a) illustrates the stream function iterative error norm with changes in the Eckert number using the MSQLM and the MOGSQLM. Both methods give small errors in the range $10^{-8}-10^{-10}$ in four to five iterations. Larger Eckert numbers lead to much smaller errors with fewer iterations. For the same number of iterations, the MOGSQLM gives a smaller error than the MSQLM. Similar results are observed in Figures 3.2 (b)-(c), and the same conclusions regarding the relative accuracy of the MSQLM and MOGSQLM methods holds.
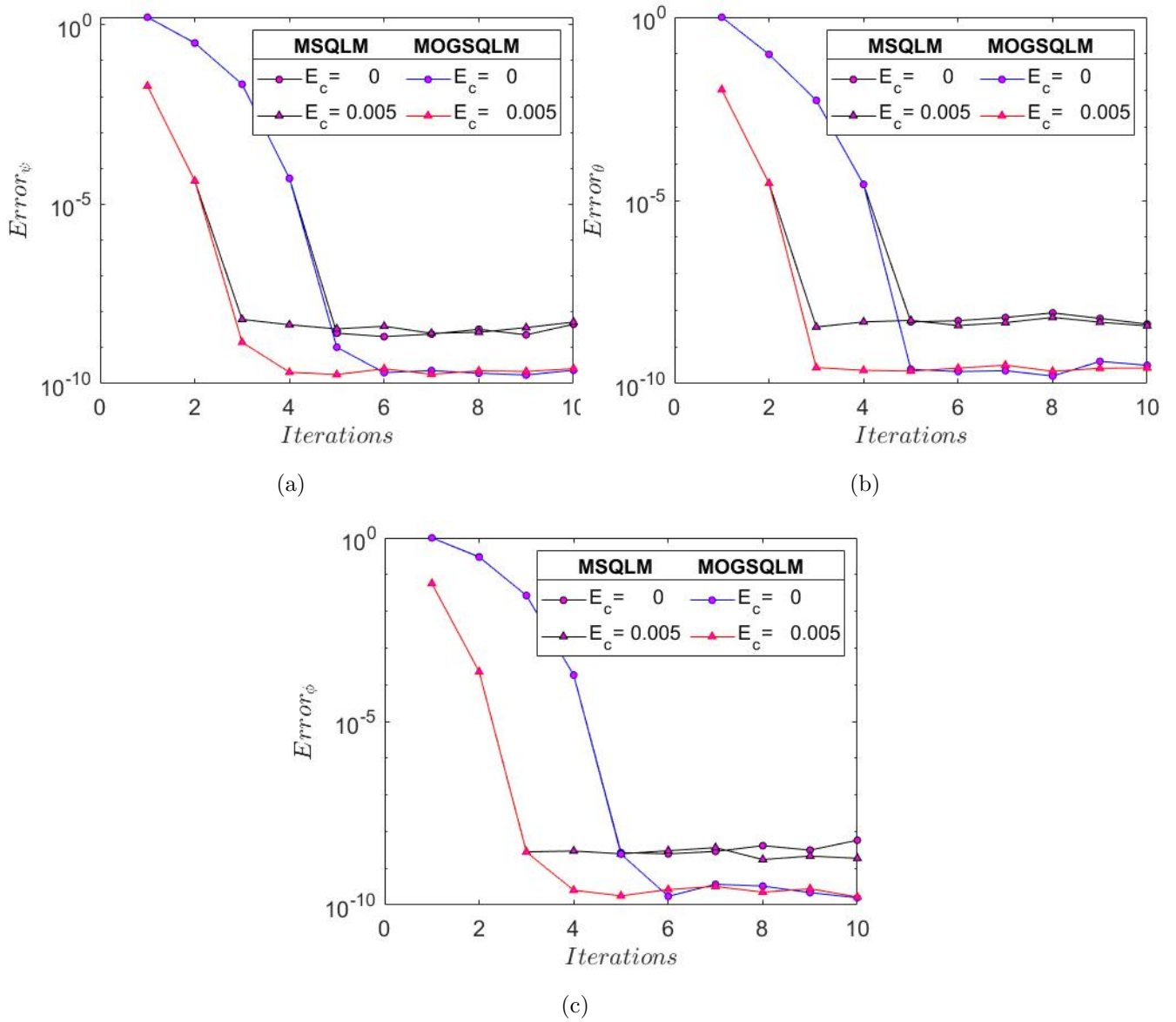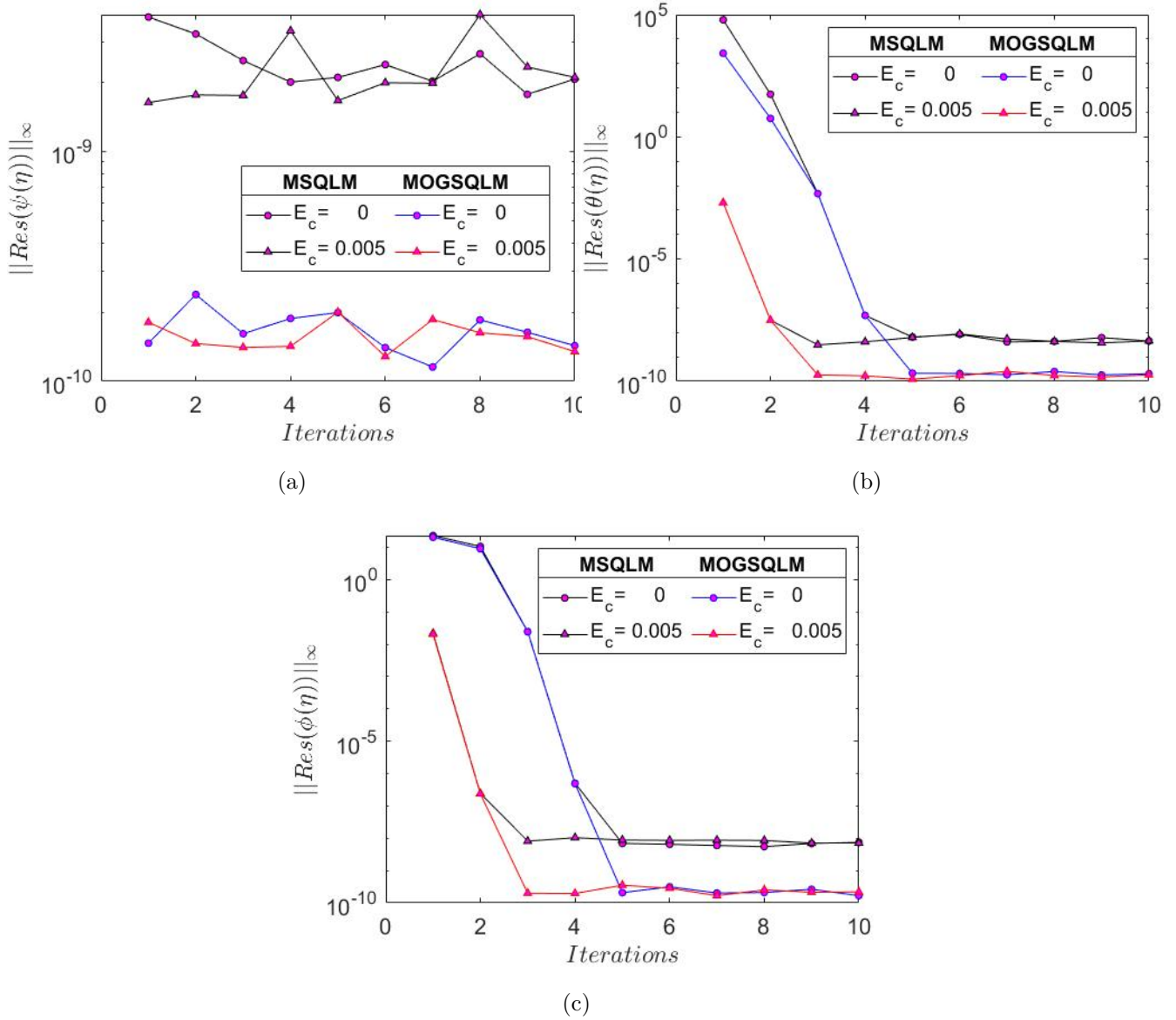
Figure 3.2: The effect of changes in the Eckert number on iterative error norms in (a) the stream function, (b) the temperature and (c) the concentration fields.

The effect of the Eckert number on the residual error in the stream function, temperature and concentration obtained using the MSQLM and MOGSQLM are shown in Figure 3.3. The stream function residual error is illustrated in Figure 3.3(a). The effect of a non-zero Eckert number is to significantly reduce the size of the residual error. It is noted however, that the for any Eckert number, the error does not change with the number of iterations. Overall, the MOGSQLM is seen to give a smaller error than the MSQLM. Similar results are observed in Figures 3.3(b)-(c) which illustrate the error in the temperature and concentration fields. However, in this case, the size of residual errors reduce as the number of iterations increases. This, in general, is expected of convergent iterative schemes.

Figure 3.3: The effect of changes in the Eckert number on residual errors in (a) the stream function, (b) the temperature and (c) the concentration fields.

Figure 3.4 shows changes in the streamline pattern with the Eckert number. We observe two counter rotating circulations which are symmetric about the line $x = 0$. The two circulation flows are formed as a result of equal heating and the left and right vertical walls. The heating on the left wall leads to the left flow circulation and similarly the heating on the right hand side leads to the right flow circulation. With heating the fluid becomes less dense and moves in an upward direction, where it is cooled, becomes heavier and is forced downwards. The streamlines are more concentrated near the top, which is where the fluid is fastest. The fluid gains more velocity as it moves up along the hot wall. Thus it reaches the top with the maximum velocity. The top wall is cold, hence the cold temperature sends the fluid downwards. The fluid slows down as it gains density on it downwards movement. The fluid is slow at the bottom wall as it has the maximum density because of the cold wall. Thus, there is less fluid

near the bottom wall since the fluid is slow and more fluid is near the top wall. The increase in the Eckert number pushes the fluid towards the top wall and nearer the hot wall. The increase in the Eckert number also leads to a decrease in streamline concentration created thus the flow slows down. This is may be attributed to the fact that increasing the Eckert number increases the viscous dissipation, which leads to a slowing down of the motion. Figure 3.4(b) shows streamlines obtained using the MOGSQLM. The two results are qualitatively similar.

(a)

(b)
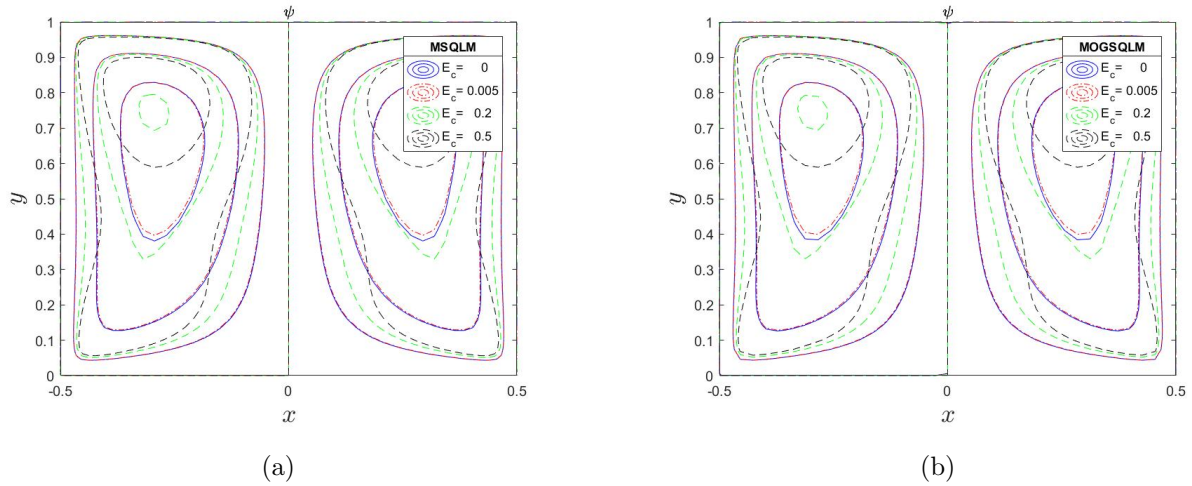
Figure 3.4: The effect of changes in the Eckert number on the streamline patterns using (a)the MSQLM and (b)the MOGSQLM.

Figure 3.5(a) illustrates the isotherms produced by the MSQLM. Increasing the Eckert number leads to an increase in the cooling of the fluid and a decrease in heat transfer. It can also be seen that the isotherms at the top cooling wall are more spread than isotherms near the bottom cooling wall. This is because more cooling occurs at the top wall than near the bottom wall. Qualitatively similar results were obtained using the MOGSQLM in Figure 3.5(b).
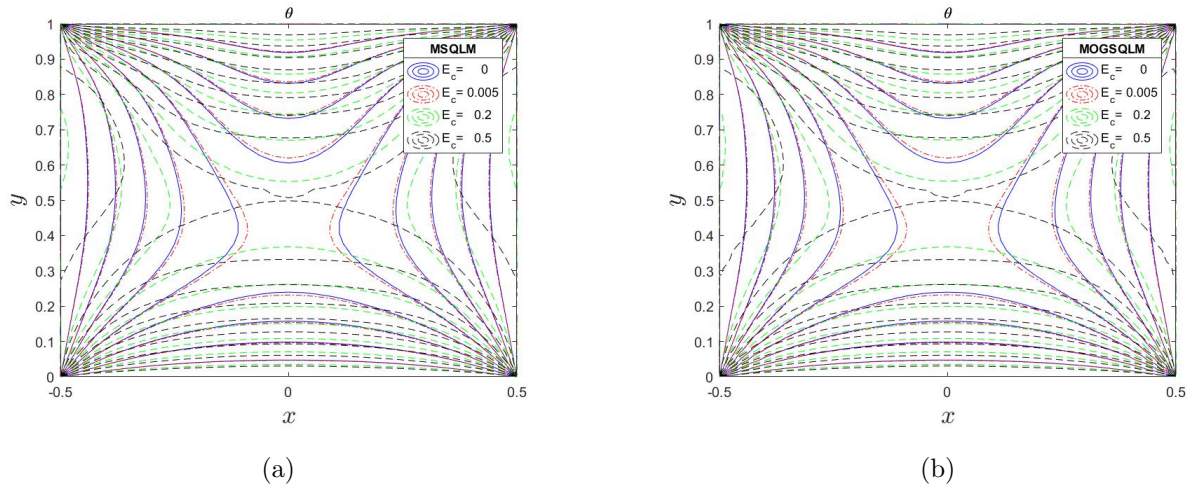
Figure 3.5: Effect of changes in the Eckert number on the isotherms using (a) the MSQLM and (b) the MOGSQLM.

Figure 3.6(a) illustrates the distribution of isoconcentrations with changes in the Eckert number obtained using the MSQLM. The isoconcentration curves are denser towards the bottom of the cavity. Qualitatively similar results are obtained using the MOGSQLM in Figure 3.6(b).
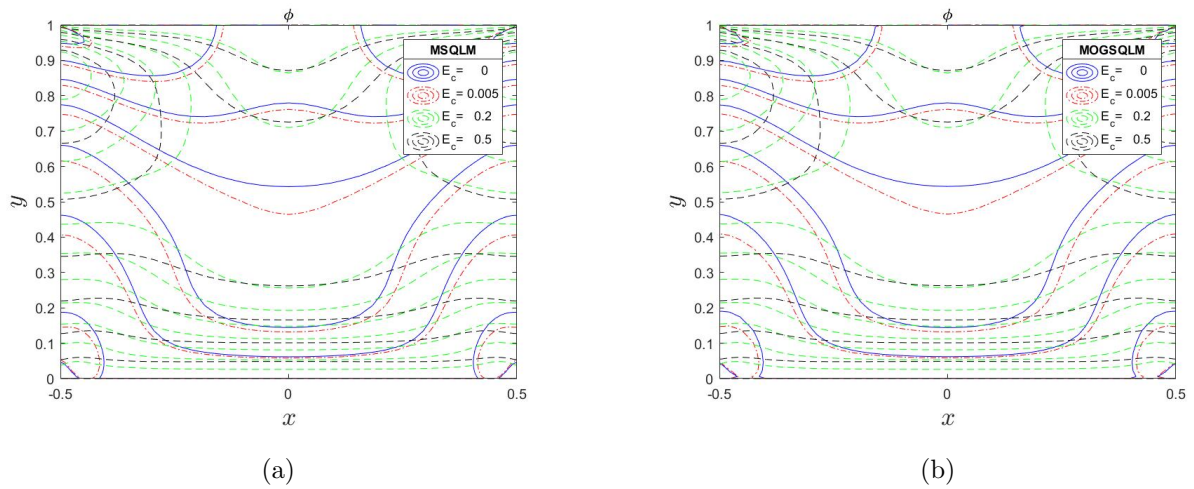

Figure 3.6: The effect of changes in the Eckert number on the isoconcentrations using (a) the MSQLM and (b) the MOGSQLM.

Figure 3.7 shows the changes in the streamline patterns with the Brownian motion parameter as obtained using the MSQLM and the MOGSQLM. An increase in the Brownian motion reduces the density of the streamlines. Increasing the Brownian motion increases thermal diffusion.

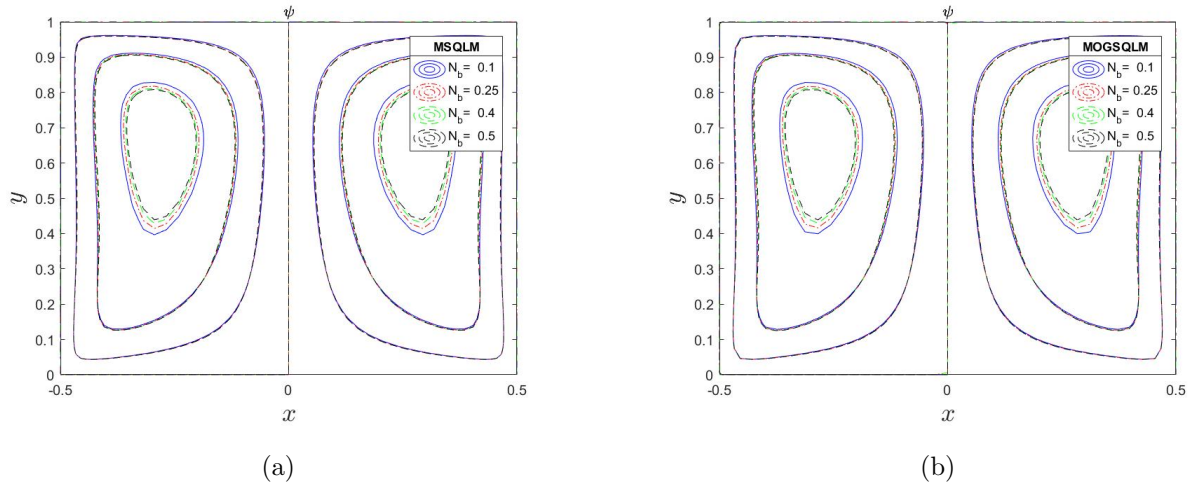(a)   (b)

Figure 3.7: The effect of changes in the Brownian motion parameter on the streamlines using (a) the MSQLM and (b) the MOGSQLM.

Figure 3.8 shows the isotherms with changes in the Brownian motion parameter. The increase in the parameter increases the temperature.
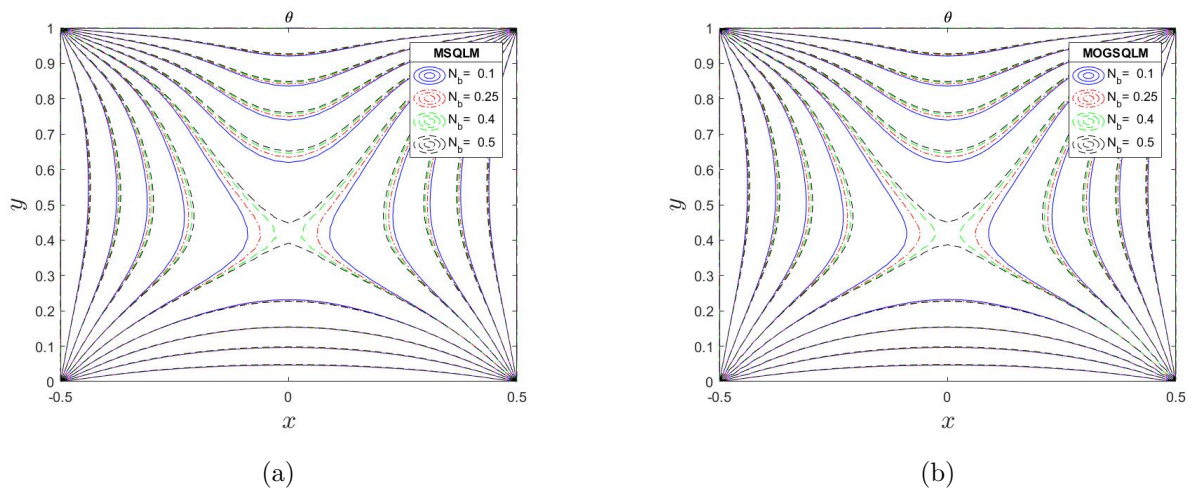

(a)   (b)

Figure 3.8: The effect of changes in the Brownian motion parameter on the isotherms using (a) the MSQLM and (b) the MOGSQLM.

Figure 3.9 are isoconcentrations for changing the Brownian parameter. Near the heated walls the parameter reduces the density of the isoconcentrations.
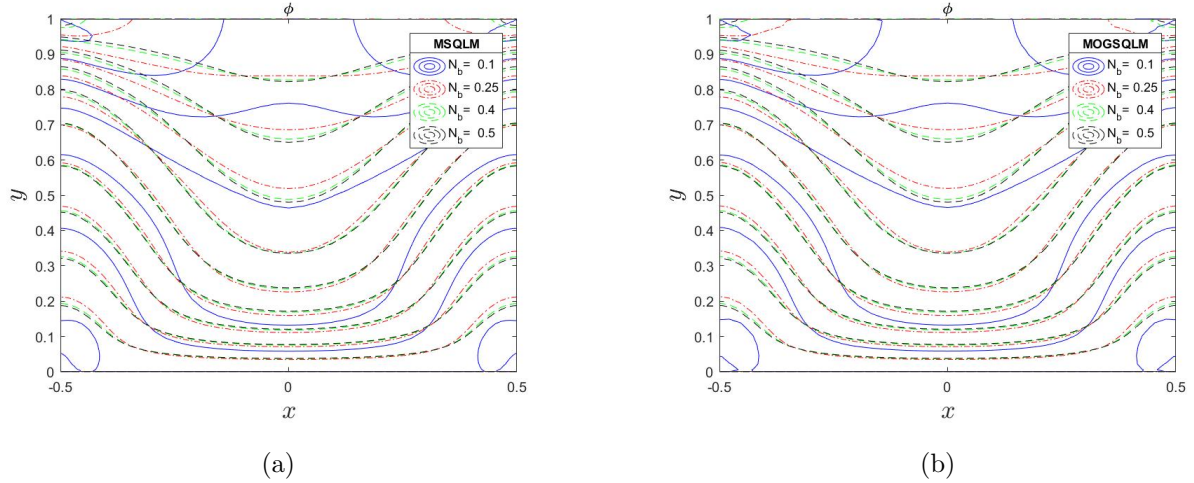
Figure 3.9: The effect of changes in the Brownian motion parameter on the isoconcentrations using (a) the MSQLM and (b) the MOGSQLM.

Figure 3.10 shows the effect of changing the radiation parameter on streamlines, isotherms and isoconcentration. Figure 3.10(a) shows the effect of changing the radiation parameter on the streamlines using the MSQLM. The streamlines decrease with an increase in the radiation parameter. It can be said that the flow becomes faster as the radiation parameter increases. Figure 3.10(b) illustrates the streamlines using the MOGSQLM with qualitatively similar results.
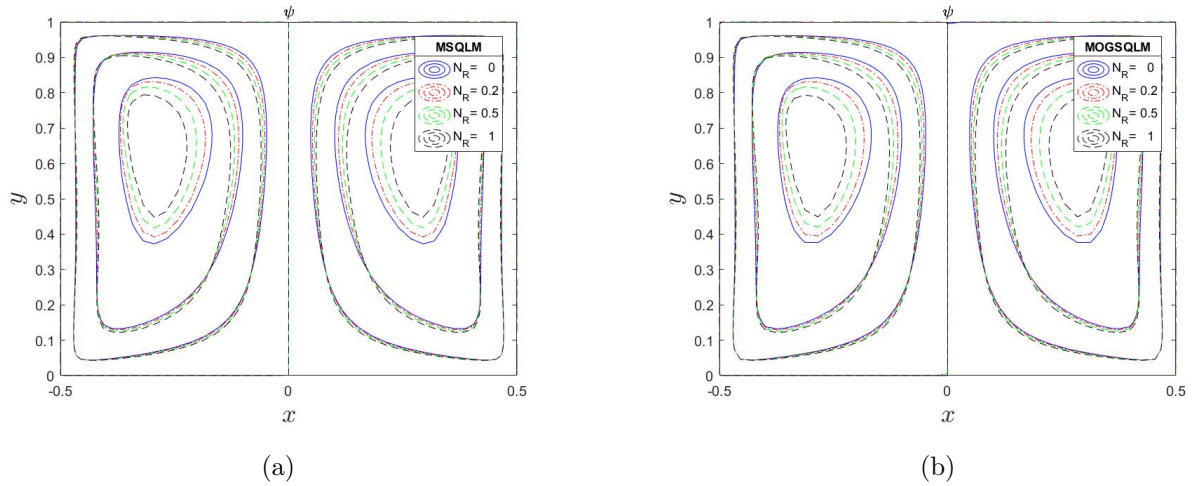

Figure 3.10: The effect of changes in the radiation parameter on the streamlines using (a) the MSQLM and (b) the MOGSQLM.

Figure 3.11(a) illustrates isotherms for the flow with changes in the radiation parameter produced by the MSQLM. An increase in radiation parameter increases the temperature distribution. In Figure 3.11(b) the isotherm pattern is qualitatively similar showing that the two methods produce near identical results.
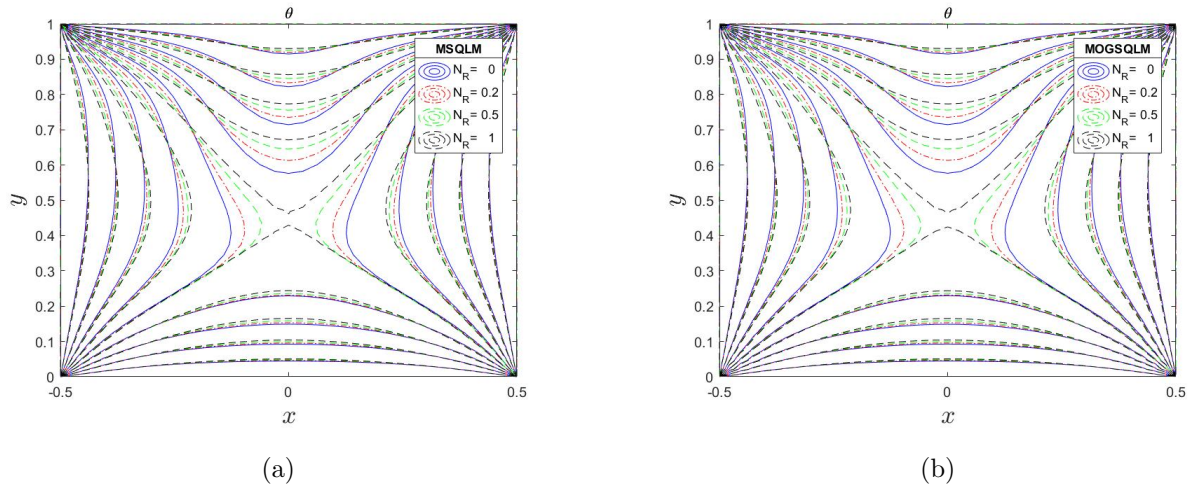
Figure 3.11: The effect of changes in the radiation parameter on the isotherms using (a) the MSQLM and (b) the MOGSQLM.

3.4 Summary

The MSQLM and MOGSQLM were compared in the solution of the equations describing natural convection in a porous square cavity with two heated walls and two cooled walls. The MSQLM and MOGSQLM were both found to be accurate, and to converge fast to the solution of the nonlinear system of equations. The MOGSQLM was found to give marginally better performance than the MSQLM in terms of accuracy, convergence and CPU time. The system has two symmetric and counter rotating flow circulations near each of the heated vertical walls. The Eckert number reduces the fluid speed while the Brownian motion and radiation parameters enhance the flow. The Eckert number increases the cooling and reduces concentration while the Brownian motion and radiation increases heat and concentration. Similar results were obtained in the study by Ducasse and Sibanda [59].

Chapter 4

On a sinusoidally heated lid-driven cavity flow in a porous medium

In Chapters 2 and 3 we solved cavity flow problems of different complexity using both the MSQLM and the MOGSQLM. We have shown that the MOGSQLM performs marginally better than the MSQLM although qualitatively the results are identical. In this chapter we use only the MOSQLM to investigate cavity flow in a porous medium saturated with a nanofluid. We determine how parameters such as the thermophoresis parameter, the chemical reaction parameter, Hartmann number and Lewis number affect the flow. We further consider the effects of a magnetic field, a chemical reaction and a moving wall. This problem was solved by Goqo et al. [7] in the case when one wall had a constant temperature. Here we assume that the two vertical walls are heated with a sinusoidally varying temperature.

4.1   Mathematical Formulation

We consider a square cavity of length L that is filled with a nanofluid and vertical walls that are heated with sinusoidally varying temperatures. The flow is incompressible and laminar. The concentration is $C = 0$ on the left vertical surface, while on the right hand surface the concentration is $C = C_0$. The top wall is moving with speed u_0 to the right. Figure 4.1 shows the geometry of the cavity, with $\bar{x}$ and $\bar{y}$ as the Cartesian coordinate system. A magnetic field is applied in the $\bar{x}$ direction, and the Darcy–Boussinesq approximation assumed without the inertia term. We consider a uniform permeability and porosity throughout the cavity. In this study we consider the effects of a thermophoresis, chemical reaction, Brownian motion, magnetic field, and heat generation. The following system of equations is obtained

with the above assumptions [7]:

$$\frac{\partial u}{\partial \bar{x}} + \frac{\partial v}{\partial \bar{y}} = 0, \tag{4.1}$$

$$\rho\left(u\frac{\partial u}{\partial \bar{x}} + v\frac{\partial u}{\partial \bar{y}}\right) = -\frac{\partial P}{\partial \bar{x}} + \left(\frac{\partial^2 u}{\partial \bar{x}^2} + \frac{\partial^2 u}{\partial \bar{y}^2}\right) - \frac{\mu}{k}u, \tag{4.2}$$

$$\rho\left(u\frac{\partial v}{\partial \bar{x}} + v\frac{\partial v}{\partial \bar{y}}\right) = -\frac{\partial P}{\partial \bar{y}} + \left(\frac{\partial^2 v}{\partial \bar{x}^2} + \frac{\partial^2 v}{\partial \bar{y}^2}\right) + gC(\rho_p - \rho_f) + g\rho_f(1 - \beta(T - T_c)(1 - C_0)) - \frac{\mu}{k}v - \frac{\sigma B_0^2}{\rho}v. \tag{4.3}$$

We eliminate the pressure P from equations (4.2) and (4.3) and apply equation (4.1) to the resulting equations to obtain the following system of equations.

$$\frac{\mu}{k}\left(\frac{\partial u}{\partial \bar{x}} - \frac{\partial v}{\partial \bar{y}}\right) = -(1 - C_0)\rho_f \beta g\frac{\partial T}{\partial \bar{x}} + g(\rho_p - \rho_f)\frac{\partial C}{\partial \bar{x}} - \frac{\sigma B_0^2}{\rho}\frac{\partial v}{\partial \bar{x}}, \tag{4.4}$$
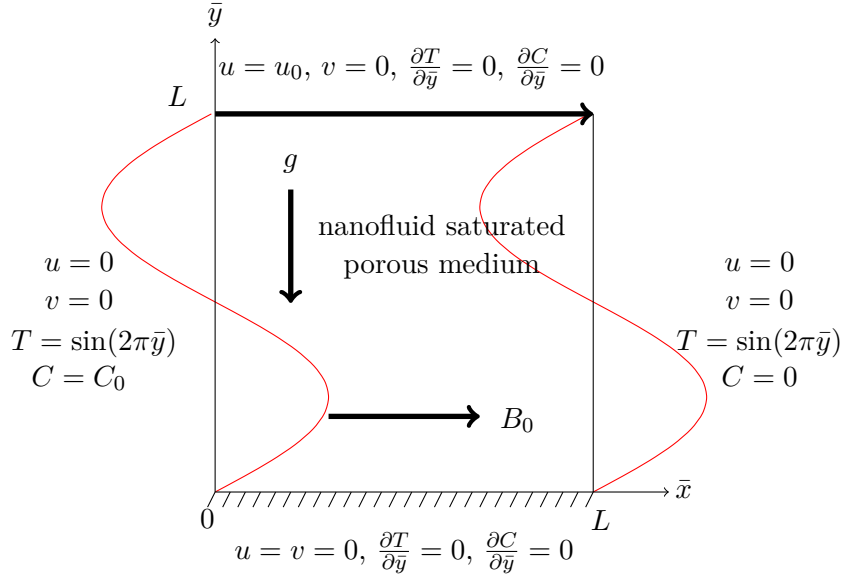

Figure 4.1: Geometry of the problem

The energy and concentration equations are given as

$$u\frac{\partial T}{\partial \bar{x}} + v\frac{\partial T}{\partial \bar{y}} = \alpha_m\left(\frac{\partial^2 T}{\partial \bar{x}^2} + \frac{\partial^2 T}{\partial \bar{y}^2}\right) + \delta D_B\left(\frac{\partial C}{\partial \bar{x}}\frac{\partial T}{\partial \bar{x}} + \frac{\partial C}{\partial \bar{y}}\frac{\partial T}{\partial \bar{y}}\right) + \delta\frac{D_T}{T_c}\left(\left(\frac{\partial T}{\partial \bar{x}}\right)^2 + \left(\frac{\partial T}{\partial \bar{y}}\right)^2\right)$$

$$+ \frac{16\sigma_{SB}T_\infty^3}{3\alpha_R}\left(\frac{\partial^2 T}{\partial \bar{x}^2} + \frac{\partial^2 T}{\partial \bar{y}^2}\right) + \frac{\mu}{k(\rho C_p)_f}(u^2 + v^2) + \frac{Q_0}{(\rho C_p)_f}\left(\frac{\partial T}{\partial \bar{x}} + \frac{\partial T}{\partial \bar{y}}\right), \tag{4.5}$$

$$\frac{1}{\varepsilon}\left(u\frac{\partial C}{\partial \bar{x}} + v\frac{\partial C}{\partial \bar{y}}\right) = D_B\left(\frac{\partial^2 C}{\partial \bar{x}^2} + \frac{\partial^2 C}{\partial \bar{y}^2}\right) + \frac{D_T}{T_c}\left(\frac{\partial^2 T}{\partial \bar{x}^2} + \frac{\partial^2 T}{\partial \bar{y}^2}\right) - R\left(\frac{\partial C}{\partial \bar{x}} + \frac{\partial C}{\partial \bar{y}}\right), \tag{4.6}$$

respectively where T is the temperature of the fluid, D_B is the Brownian diffusion coefficient, u and v are the velocity components along the $\bar{x}$ and $\bar{y}$ directions, C is the nanoparticle volume fraction, g is the gravity vector, D_T is the thermophoretic diffusion coefficient, ρ_f is the reference density of the fluid, α_m denote the effective thermal diffusivity of the porous medium, k is the average thermal conductivity

of the fluid, μ is the dynamic viscosity, and ρ_p is the nanoparticle mass density, respectively. C_p is the heat capacity at constant pressure, $(\rho C_p)_f$ is heat capacity of the base fluid, $(\rho C_p)_p$ is effective heat capacity of the nanoparticle material, β is the coefficient of thermal expansion, ε is the porosity, Q_0 is the heat generation parameter and R is the reaction parameter. The boundary conditions are shown on Figure 4.1.

The stream function (1.13) is introduced on the equations (4.1) and (4.4) - (4.6) then reduced to the following equations:

$$\frac{\mu}{k}\left(\frac{\partial^2 \Psi}{\partial \bar{y}^2}+\frac{\partial^2 \Psi}{\partial \bar{x}^2}\right) = -(1-C_0)\rho_f\beta g\frac{\partial T}{\partial \bar{x}}+g(\rho_p-\rho_f)\frac{\partial C}{\partial \bar{x}}-\frac{\sigma B_0^2}{\rho}\frac{\partial^2 \Psi}{\partial \bar{x}^2}, \tag{4.7}$$

$$\frac{\partial \Psi}{\partial \bar{y}}\frac{\partial T}{\partial \bar{x}}+\frac{\partial \Psi}{\partial \bar{x}}\frac{\partial T}{\partial \bar{y}} = \alpha_m\left(\frac{\partial^2 T}{\partial \bar{x}^2}+\frac{\partial^2 T}{\partial \bar{y}^2}\right)+\delta D_B\left(\frac{\partial C}{\partial \bar{x}}\frac{\partial T}{\partial \bar{x}}+\frac{\partial C}{\partial \bar{y}}\frac{\partial T}{\partial \bar{y}}\right)+\delta\frac{D_T}{T_c}\left(\left(\frac{\partial T}{\partial \bar{x}}\right)^2+\left(\frac{\partial T}{\partial \bar{y}}\right)^2\right)$$
$$+\frac{16\sigma_{SB}T_\infty^3}{3\alpha_R}\left(\frac{\partial^2 T}{\partial \bar{x}^2}+\frac{\partial^2 T}{\partial \bar{y}^2}\right)+\frac{\mu}{k(\rho C_p)_f}\left(\left(\frac{\partial \Psi}{\partial \bar{x}}\right)^2+\left(\frac{\partial \Psi}{\partial \bar{y}}\right)^2\right)+\frac{Q_0}{(\rho C_p)_f}\left(\frac{\partial T}{\partial \bar{x}}+\frac{\partial T}{\partial \bar{y}}\right), \tag{4.8}$$

$$\frac{1}{\varepsilon}\left(\frac{\partial \Psi}{\partial \bar{y}}\frac{\partial C}{\partial \bar{x}}+\frac{\partial \Psi}{\partial \bar{x}}\frac{\partial C}{\partial \bar{y}}\right) = D_B\left(\frac{\partial^2 C}{\partial \bar{x}^2}+\frac{\partial^2 C}{\partial \bar{y}^2}\right)+\frac{D_T}{T_c}\left(\frac{\partial^2 T}{\partial \bar{x}^2}+\frac{\partial^2 T}{\partial \bar{y}^2}\right)-R\left(\frac{\partial C}{\partial \bar{x}}+\frac{\partial C}{\partial \bar{y}}\right). \tag{4.9}$$

We introduce non-dimension variables as follows

$$x = \frac{\bar{x}}{l},\ y = \frac{\bar{y}}{l},\ \psi = \frac{\Psi}{\alpha_m},\ \theta = \frac{T-T_c}{\Delta T},\ \phi = \frac{C}{C_0}, \tag{4.10}$$

where $\Delta T = T_h-T_c$. We substitute equation (4.10) into equations (4.7) - (4.9) and obtain the following equations:

$$(1+H_a^2)\left(\frac{\partial^2 \psi}{\partial x^2}\right)+\frac{\partial^2 \psi}{\partial y^2} = -R_a\frac{\partial \theta}{\partial x}+R_aN_r\frac{\partial \phi}{\partial x}, \tag{4.11}$$

$$\frac{\partial \psi}{\partial y}\frac{\partial \theta}{\partial x}-\frac{\partial \psi}{\partial x}\frac{\partial \theta}{\partial y} = \left(1+\frac{4}{3}N_R\right)\left(\frac{\partial^2 \theta}{\partial x^2}+\frac{\partial^2 \theta}{\partial y^2}\right)+N_b\left(\frac{\partial \phi}{\partial y}\frac{\partial \theta}{\partial x}+\frac{\partial \phi}{\partial x}\frac{\partial \theta}{\partial y}\right)+N_t\left(\left(\frac{\partial \theta}{\partial x}\right)^2+\left(\frac{\partial \theta}{\partial y}\right)^2\right)$$
$$+E_c\left(\left(\frac{\partial \psi}{\partial x}\right)^2+\left(\frac{\partial \psi}{\partial y}\right)^2\right)+\gamma\left(\frac{\partial \theta}{\partial x}+\frac{\partial \theta}{\partial y}\right), \tag{4.12}$$

$$\frac{\partial \psi}{\partial y}\frac{\partial \phi}{\partial x}-\frac{\partial \psi}{\partial x}\frac{\partial \phi}{\partial y} = \frac{1}{L_e}\left(\frac{\partial^2 \phi}{\partial x^2}+\frac{\partial^2 \phi}{\partial y^2}\right)+\frac{1}{L_e}\frac{N_t}{N_b}\left(\frac{\partial^2 \theta}{\partial x^2}+\frac{\partial^2 \theta}{\partial y^2}\right)-R_1\left(\frac{\partial \phi}{\partial x}+\frac{\partial \phi}{\partial y}\right), \tag{4.13}$$

where $H_a = \sqrt{\frac{\sigma B_0^2 k}{\rho\mu}}$ is the Hartmann number, $R_a = \frac{(1-C_0)gk\rho_f\beta\Delta TL}{\mu\alpha_m}$ is the Rayleigh number for the porous medium, $L_e = \frac{\alpha_m}{\varepsilon D_B}$ is the Lewis number, $N_R = \frac{4\sigma_s BT_\infty^3}{\alpha_R\alpha_m}$ is the radiation parameter, $E_c = \frac{\mu\alpha_m}{k(\rho C_p)_f\Delta T}$ is the Eckert number for the porous medium, $N_r = \frac{(\rho_p-\rho_f)C_0}{\rho_f\beta\Delta T(1-C_0)}$ is the buoyancy ratio parameter, $N_b = \frac{\delta D_B C_0}{\alpha_m}$ is the Brownian motion parameter, $N_t = \frac{\delta D_T\Delta T}{\alpha_m T_c}$ is the thermophoresis parameter, $\gamma = \frac{Q_0L}{(\rho C_p)_f}$ is the heat generation parameter, and $R_1 = \frac{RC_0}{L}$ is the chemical reaction parameter.

The system of nonlinear equations is solved subject to the following boundary conditions

$$\psi(0,y)=0, \quad \theta(0,y)=\sin(2\pi y), \quad \phi(0,y)=1, \quad \psi(1,y)=0, \quad \theta(1,y)=\sin(2\pi y), \quad \phi(1,y)=0,$$

$$\psi(x,0)=0, \quad \frac{\partial\theta(x,0)}{\partial y}=0, \quad \frac{\partial\phi(x,0)}{\partial y}=0, \quad \psi(x,1)=1, \quad \frac{\partial\theta(x,1)}{\partial y}=0, \quad \frac{\partial\phi(x,1)}{\partial y}=0. \tag{4.14}$$

4.2 Numerical Solution

The MOGSQLM was used to solve equations (4.11) - (4.13) subject to the boundary conditions (4.14). As in Chapters 2-3, we assign the following variables to equations (4.11) - (4.13),

$$\Psi_3=(1+H_a^2)\psi_{xx}+\psi_{yy}+R_a\theta_x-R_aN_r\phi_x=0, \tag{4.15}$$

$$\Theta_3=\left(1+\frac{4}{3}N_R\right)(\theta_{xx}+\theta_{yy})+N_b[\phi_x\theta_x+\phi_y\theta_y]+N_t[\theta_x^2+\theta_y^2]+E_c[\psi_x^2+\psi_y^2]+\gamma[\theta_x+\theta_y]-\psi_y\theta_x+\psi_x\theta_y=0, \tag{4.16}$$

$$\Phi_3=\frac{1}{l_e}(\phi_{xx}+\phi_{yy})+\frac{1}{l_e}\frac{N_t}{N_b}(\theta_{xx}+\theta_{yy})-R_1(\phi_x+\phi_y)-\psi_y\phi_x+\psi_x\phi_y=0. \tag{4.17}$$

Equations (4.15) - (4.17) will be solved subject to the boundary conditions (4.14). The rectangular domain is discretized as in Chapter 2. The linearized equations are

$$a_{\psi_{xx},r}\psi_{xx,r+1}+a_{\psi_{yy},r}\psi_{yy,r+1}+a_{\theta_x,r}\theta_{x,r+1}+a_{\phi_x,r}\phi_{x,r+1}=R_{\psi,r}, \tag{4.18}$$

$$b_{\psi_x,r}\psi_{x,r+1}+b_{\psi_y,r}\psi_{y,r+1}+b_{\theta_{xx},r}\theta_{xx,r+1}+b_{\theta_x,r}\theta_{x,r+1}+b_{\theta_{yy},r}\theta_{yy,r+1}+b_{\theta_y,r}\theta_{y,r+1}+b_{\phi_x,r}\phi_{x,r+1}+$$

$$b_{\phi_y,r}\phi_{y,r+1}=R_{\theta,r}, \tag{4.19}$$

$$c_{\psi_x,r}\psi_{x,r+1}+c_{\psi_y,r}\psi_{y,r+1}+c_{\theta_{xx},r}\theta_{xx,r+1}+c_{\theta_{yy},r}\theta_{yy,r+1}+c_{\phi_{xx},r}\phi_{xx,r+1}+c_{\phi_x,r}\phi_{x,r+1}+c_{\phi_{yy},r}\phi_{yy,r+1}$$

$$+c_{\phi_y,r}\phi_{y,r+1}=R_{\phi,r}, \tag{4.20}$$

where

$$a_{\psi_{xx},r}=\frac{\partial\Psi_3}{\partial\psi_{xx,r}}=1+H_a^2, \ a_{\psi_{yy},r}=\frac{\partial\Psi_3}{\partial\psi_{yy,r}}=1, \ a_{\theta_x,r}=\frac{\partial\Psi_3}{\partial\theta_{x,r}}=R_a, \ a_{\phi_x,r}=\frac{\partial\Psi_3}{\partial\phi_{x,r}}=-R_aN_r,$$

$$b_{\psi_x,r}=\frac{\partial\Theta_3}{\partial\psi_{x,r}}=2E_c\psi_{x,r}+\theta_{y,r}, \ b_{\psi_y,r}=\frac{\partial\Theta_3}{\partial\psi_{y,r}}=2E_c\psi_{y,r}-\theta_{x,r}, \ b_{\theta_{xx},r}=\frac{\partial\Theta_3}{\partial\theta_{xx,r}}=1+\frac{4}{3}N_R,$$

$$b_{\theta_x,r}=\frac{\partial\Theta_3}{\partial\theta_{x,r}}=N_b\phi_{x,r}+2N_t\theta_{x,r}+\gamma-\psi_{y,r}, \ b_{\theta_{yy},r}=\frac{\partial\Theta_3}{\partial\theta_{yy,r}}=1+\frac{4}{3}N_R,$$

$$b_{\theta_y,r}=\frac{\partial\Theta_3}{\partial\theta_{y,r}}=N_b\phi_{y,r}+2N_t\theta_{y,r}+\gamma+\psi_{x,r}, \ b_{\phi_x,r}=\frac{\partial\Theta_3}{\partial\phi_{x,r}}=N_b\theta_{x,r}, \ b_{\phi_y,r}=\frac{\partial\Theta_3}{\partial\phi_{y,r}}=N_b\theta_{y,r},$$

$$c_{\psi_x,r}=\frac{\partial\Phi}{\partial\psi_{x,r}}=\psi_{y,r}, \ c_{\psi_y,r}=\frac{\partial\Phi}{\partial\psi_{y,r}}=-\psi_{x,r}, \ c_{\theta_{xx},r}=\frac{\partial\Phi}{\partial\theta_{xx,r}}=\frac{1}{L_e}\frac{N_t}{N_b}, \ c_{\theta_{yy},r}=\frac{\partial\Phi}{\partial\theta_{yy,r}}=\frac{1}{L_e}\frac{N_t}{N_b},$$

$$c_{\phi_{xx},r}=\frac{\partial\Phi}{\partial\phi_{xx,r}}=\frac{1}{L_e}, \ c_{\phi_x,r}=\frac{\partial\Phi}{\partial\phi_{x,r}}=-R_1-\psi_{y,r} \ c_{\phi_{yy},r}=\frac{\partial\Phi}{\partial\phi_{yy,r}}=\frac{1}{L_e}, \ c_{\phi_y,r}=\frac{\partial\Phi}{\partial\phi_{y,r}}=-R_1+\psi_{x,r},$$

$$R_{\psi,r}=a_{\psi_{xx},r}\psi_{xx,r}+a_{yy,r}\psi_{yy,r}+a_{\theta_x,r}\theta_{x,r}+a_{\phi_x,r}\phi_{x,r}-\Psi_3,$$

$$R_{\theta,r}=b_{\psi_x,r}\psi_{x,r}+b_{\psi_y,r}\psi_{y,r}+b_{\theta_{xx},r}\theta_{xx,r}+b_{\theta_x,r}\theta_{x,r}+b_{\theta_{yy},r}\theta_{yy,r}+b_{\theta_y,r}\theta_{y,r}+b_{\phi_x,r}\phi_{x,r}+b_{\phi_y,r}\phi_{y,r}-\Theta_3,$$

$$R_{\Phi,r}=c_{\psi_x,r}\psi_{x,r}+c_{\psi_y,r}\psi_{y,r}+c_{\theta_{xx},r}\theta_{xx,r}+c_{\theta_{yy},r}\theta_{yy,r}+c_{\phi_{xx},r}\phi_{xx,r}+c_{\phi_x,r}\phi_{x,r}+c_{\phi_{yy},r}\phi_{yy,r}+c_{\phi_y,r}\phi_{y,r}-\Phi_3. \tag{4.21}$$

Using multivariate overlapping grid Lagrange polynomials we rewrite equations (4.18) - (4.20) for the spectral collocation method with the unknown functions $\psi(x,y)$, $\theta(x,y)$ and $\phi(x,y)$. The equations can be rewritten as the following scheme:

$$[diag(a_{\psi_{xx},r})\boldsymbol{D_{xx}}]\boldsymbol{\psi}_{r+1}(x_i,y_j)+[diag(a_{\psi_{yy},r})\sum_{q=0}^{N_y}\boldsymbol{D_{yy}}_{j,q}]\boldsymbol{\psi}_{r+1}(x_i,y_q)+[diag(a_{\theta_x,r})\boldsymbol{D_x}]\boldsymbol{\theta}_{r+1}(x_i,y_j)$$

$$= \boldsymbol{R}_{\psi,r,j}, \tag{4.22}$$

$$[diag(b_{\psi_x,r})\boldsymbol{D_x}]\boldsymbol{\psi}_{r+1}(x_i,y_j)+[diag(b_{\psi_y,r})\sum_{q=0}^{N_y}\boldsymbol{D_y}_{j,q}]\boldsymbol{\psi}_{r+1}(x_i,y_q)+[diag(b_{\theta_{xx},r})\boldsymbol{D_{xx}}$$

$$+diag(b_{\theta_x,r})\boldsymbol{D_x}]\boldsymbol{\theta}_{r+1}(x_i,y_j)+[diag(b_{\theta_{yy},r})\sum_{q=0}^{N_y}\boldsymbol{D_{yy}}_{j,q}+diag(b_{\theta_y,r})\sum_{q=0}^{N_y}\boldsymbol{D_y}_{j,q}]\boldsymbol{\theta}_{r+1}(x_i,y_q)$$

$$+[diag(b_{\phi_{xx},r})\boldsymbol{D_{xx}}]\boldsymbol{\phi}_{r+1}(x_i,y_j)+[diag(b_{\phi_y,r})\sum_{q=0}^{N_y}\boldsymbol{D_y}_{j,q}]\boldsymbol{\phi}_{r+1}(x_i,y_q) = \boldsymbol{R}_{\theta,r,j}, \tag{4.23}$$

$$[diag(c_{\psi_x,r})\boldsymbol{D_x}]\boldsymbol{\psi}_{r+1}(x_i,y_j)+[diag(c_{\psi_y,r})\sum_{q=0}^{N_y}\boldsymbol{D_y}_{j,q}]\boldsymbol{\psi}(x_i,y_q)+[diag(c_{\theta_{xx},r})\boldsymbol{D_{xx}}]\boldsymbol{\theta}_{r+1}(x_i,y_j)$$

$$+[diag(c_{\theta_{yy},r})\sum_{q=0}^{N_y}\boldsymbol{D_{yy}}_{j,q}]\boldsymbol{\theta}(x_i,y_q)+[diag(c_{\phi_{xx},r})\boldsymbol{D_{xx}}+diag(c_{\phi_x,r})\boldsymbol{D_x}]\boldsymbol{\phi}_{r+1}(x_i,y_j)$$

$$+[diag(c_{\phi_{yy},r})\sum_{q=0}^{N_y}\boldsymbol{D_{yy}}_{j,q}+diag(c_{\phi_y,r})\sum_{q=0}^{N_y}\boldsymbol{D_y}_{j,q}]\boldsymbol{\phi}(x_i,y_q) = \boldsymbol{R}_{\phi,r,j}, \tag{4.24}$$

where the vectors $\boldsymbol{R}_{\psi,r,j}$, $\boldsymbol{R}_{\theta,r,j}$ and $\boldsymbol{R}_{\phi,r,j}$ are $\boldsymbol{R}_{\psi,r}$, $\boldsymbol{R}_{\theta,r}$ and $\boldsymbol{R}_{\phi,r}$ defined for each y_j for $j = 0,1,...,\sigma$ respectively. Equations (4.22) - (4.24) are then expressed using the following matrix:

$$\begin{bmatrix} \begin{bmatrix} A_{0,0}^{0,0} A_{0,1}^{0,0} A_{0,2}^{0,0} \\ A_{1,0}^{0,0} A_{1,1}^{0,0} A_{1,2}^{0,0} \\ A_{2,0}^{0,0} A_{2,1}^{0,0} A_{2,2}^{0,0} \end{bmatrix} & \begin{bmatrix} A_{0,0}^{0,1} A_{0,1}^{0,1} A_{0,2}^{0,1} \\ A_{1,0}^{0,1} A_{1,1}^{0,1} A_{1,2}^{0,1} \\ A_{2,0}^{0,1} A_{2,1}^{0,1} A_{2,2}^{0,1} \end{bmatrix} & \cdots & \begin{bmatrix} A_{0,0}^{0,\sigma} A_{0,1}^{0,\sigma} A_{0,2}^{0,\sigma} \\ A_{1,0}^{0,\sigma} A_{1,1}^{0,\sigma} A_{1,2}^{0,\sigma} \\ A_{2,0}^{0,\sigma} A_{2,1}^{0,\sigma} A_{2,2}^{0,\sigma} \end{bmatrix} \\ \begin{bmatrix} A_{0,0}^{1,0} A_{0,1}^{1,0} A_{0,2}^{1,0} \\ A_{1,0}^{1,0} A_{1,1}^{1,0} A_{1,2}^{1,0} \\ A_{2,0}^{1,0} A_{2,1}^{1,0} A_{2,2}^{1,0} \end{bmatrix} & \begin{bmatrix} A_{0,0}^{1,1} A_{0,1}^{1,1} A_{0,2}^{1,1} \\ A_{1,0}^{1,1} A_{1,1}^{1,1} A_{1,2}^{1,1} \\ A_{2,0}^{1,1} A_{2,1}^{1,1} A_{2,2}^{1,1} \end{bmatrix} & \cdots & \begin{bmatrix} A_{0,0}^{1,\sigma} A_{0,1}^{1,\sigma} A_{0,2}^{1,\sigma} \\ A_{1,0}^{1,\sigma} A_{1,1}^{1,\sigma} A_{1,2}^{1,\sigma} \\ A_{2,0}^{1,\sigma} A_{2,1}^{1,\sigma} A_{2,2}^{1,\sigma} \end{bmatrix} \\ \vdots & \vdots & \ddots & \vdots \\ \vdots & \vdots & \ddots & \vdots \\ \begin{bmatrix} A_{0,0}^{\sigma,0} A_{0,1}^{\sigma,0} A_{0,2}^{\sigma,0} \\ A_{1,0}^{\sigma,0} A_{1,1}^{\sigma,0} A_{1,2}^{\sigma,0} \\ A_{2,0}^{\sigma,0} A_{2,1}^{\sigma,0} A_{2,2}^{\sigma,0} \end{bmatrix} & \begin{bmatrix} A_{0,0}^{\sigma,1} A_{0,1}^{\sigma,1} A_{0,2}^{\sigma,1} \\ A_{1,0}^{\sigma,1} A_{1,1}^{\sigma,1} A_{1,2}^{\sigma,1} \\ A_{2,0}^{\sigma,1} A_{2,1}^{\sigma,1} A_{2,2}^{\sigma,1} \end{bmatrix} & \cdots & \begin{bmatrix} A_{0,0}^{\sigma,\sigma} A_{0,1}^{\sigma,\sigma} A_{0,2}^{\sigma,\sigma} \\ A_{1,0}^{\sigma,\sigma} A_{1,1}^{\sigma,\sigma} A_{1,2}^{\sigma,\sigma} \\ A_{2,0}^{\sigma,\sigma} A_{2,1}^{\sigma,\sigma} A_{2,2}^{\sigma,\sigma} \end{bmatrix} \end{bmatrix} \begin{bmatrix} \begin{bmatrix} \psi_{r+1}^0 \\ \theta_{r+1}^0 \\ \phi_{r+1}^0 \end{bmatrix} \\ \begin{bmatrix} \psi_{r+1}^1 \\ \theta_{r+1}^1 \\ \phi_{r+1}^1 \end{bmatrix} \\ \vdots \\ \vdots \\ \begin{bmatrix} \psi_{r+1}^\sigma \\ \theta_{r+1}^\sigma \\ \phi_{r+1}^\sigma \end{bmatrix} \end{bmatrix} = \begin{bmatrix} \begin{bmatrix} R_{\psi,r}^0 \\ R_{\theta,r}^0 \\ R_{\phi,r}^0 \end{bmatrix} \\ \begin{bmatrix} R_{\psi,r}^1 \\ R_{\theta,r}^1 \\ R_{\phi,r}^1 \end{bmatrix} \\ \vdots \\ \vdots \\ \begin{bmatrix} R_{\psi,r}^\sigma \\ R_{\theta,r}^\sigma \\ R_{\phi,r}^\sigma \end{bmatrix} \end{bmatrix},$$

where $i = j$

$A_{0,0}^{i,i} = diag(a_{\psi_{xx},r})\boldsymbol{D_{xx}}+diag(a_{\psi_{yy},r})\boldsymbol{D_{yy}}_{i,i}\boldsymbol{I}$, $\quad A_{0,1}^{i,i} = diag(a_{\theta_x,r})\boldsymbol{D}x$, $\quad A_{0,2}^{i,i} = diag(a_{\phi_x,r})\boldsymbol{D_x}$,

$A_{1,0}^{i,i} = diag(b_{\psi_x,r})\boldsymbol{D_x}+diag(a_{\psi_y,r})\boldsymbol{D_y}_{i,i}\boldsymbol{I}$, $\quad A_{1,1}^{i,i} = diag(b_{\theta_{xx},r})\boldsymbol{D_{xx}}+diag(b_{\theta_x,r})\boldsymbol{D_x}+$

$diag(b_{\theta_{yy},r})\boldsymbol{D_{yy}}_{i,i}\boldsymbol{I}+diag(b_{\theta_y,r})\boldsymbol{D_y}_{i,i}\boldsymbol{I}$, $\quad A_{1,2}^{i,i} = diag(b_{\phi_x,r})\boldsymbol{D_x}+diag(a_{\phi_y,r})\boldsymbol{D_y}_{i,i}\boldsymbol{I}$,

$A_{2,0}^{i,i} = diag(c_{\psi_x,r})\boldsymbol{D_x}+diag(c_{\psi_y,r})\boldsymbol{D_y}_{i,i}\boldsymbol{I}$, $\quad A_{2,1}^{i,i} = diag(c_{\theta_x,r})\boldsymbol{D_x}+diag(c_{\theta_y,r})\boldsymbol{D_y}_{i,i}\boldsymbol{I}$,

$A_{2,2}^{i,i} = diag(c_{\phi_{xx,r}})\boldsymbol{D_{xx}} + diag(c_{\phi_{x,r}})\boldsymbol{D_x} + diag(c_{\phi_{yy,r}})\boldsymbol{D_{yy}}_{i,i}\boldsymbol{I} + diag(c_{\phi_{y,r}})\boldsymbol{D_y}_{i,i}\boldsymbol{I},$

And for where $i \neq j$

$A_{0,0}^{i,j} = diag(a_{\psi_{yy,r}})\boldsymbol{D_{yy}}_{i,j}\boldsymbol{I}, \quad A_{0,1}^{i,j} = \boldsymbol{O}, \quad A_{0,2}^{i,i} = \boldsymbol{O},$

$A_{1,0}^{i,j} = diag(a_{\psi_{y,r}})\boldsymbol{D_y}_{i,j}\boldsymbol{I}, \quad A_{1,1}^{i,j} = diag(b_{\theta_{yy,r}})\boldsymbol{D_{yy}}_{i,j}\boldsymbol{I} + diag(b_{\theta_{y,r}})\boldsymbol{D_y}_{i,j}\boldsymbol{I}, \quad A_{1,2}^{i,j} = diag(a_{\phi_{y,r}})\boldsymbol{D_y}_{i,j}\boldsymbol{I},$

$A_{2,0}^{i,j} = diag(c_{\psi_{y,r}})\boldsymbol{D_y}_{i,j}\boldsymbol{I}, \quad A_{2,1}^{i,j} = diag(c_{\theta_{y,r}})\boldsymbol{D_y}_{i,j}\boldsymbol{I}, \quad A_{2,2}^{i,j} = diag(c_{\phi_{yy,r}})\boldsymbol{D_{yy}}_{i,j}\boldsymbol{I} + diag(c_{\phi_{y,r}})\boldsymbol{D_y}_{i,j}\boldsymbol{I},$

where $\boldsymbol{I}$ and $\boldsymbol{O}$ are the identity matrix and the zero matrix, both of size $(N_x'+1) \times (N_x'+1)$. We now impose the boundary conditions accordingly as follows:

$$at \quad x = 0, \quad \boldsymbol{\psi}(x_{N_x'}, y_j) = 0, \quad \boldsymbol{\theta}(x_{N_x'}, y_j) = \sin(\pi y), \quad \boldsymbol{\phi}(x_{N_x'}, y_j) = 1,$$

$$at \quad x = 1, \quad \boldsymbol{\psi}(x_0, y_j) = 0, \quad \boldsymbol{\theta}(x_0, y_j) = 0, \quad \boldsymbol{\phi}(x_0, y_j) = 0,$$

$$at \quad y = 0, \quad \boldsymbol{\psi}(x_i, y_{N_y'}) = 0, \quad \sum_{q=0}^{N_y'} \boldsymbol{D_y}_{j,q}\boldsymbol{\theta}(x_i, y_{N_y'}) = 0, \quad \sum_{q=0}^{N_y'} \boldsymbol{D_y}_{j,q}\boldsymbol{\phi}(x_i, y_{N_y'}) = 0,$$

$$at \quad y = 1, \quad \boldsymbol{\psi}(x_i, y_0) = 1, \quad \sum_{q=0}^{N_y} \boldsymbol{D_y}_{j,q}\boldsymbol{\theta}(x_i, y_0) = 0, \quad \sum_{q=0}^{N_y} \boldsymbol{D_y}_{j,q}\boldsymbol{\phi}(x_i, y_0 = 0, \qquad (4.25)$$

where 0 and 1 in the y conditions are respectively vectors of zeros and ones of size $N_x'+1$.

4.3 Results and discussion

In this section we discuss the results obtained numerically using the MOGSQLM. The following parameter values $N_t = 0.25$, $N_r = 0.5$, $N_R = 0.005$, $N_b = 0.5$, $E_c = 0.9$, $H_a = 1.9$, $\gamma = 3$, $R_a = 100$, $R_1 = 0.1$, and $L_e = 0.2$ were used unless otherwise stated. The parameters are similar to those used by Goqo et al. [7].

Figure 4.2 illustrates the effect of changing the thermophoresis parameter on streamlines, isotherms and isoconcentration. In Figure 4.2(a) we note three circulations near the bottom left, top right and the middle from the top left to the bottom right of the cavity. It can be seen that the primary vortex is created by the moving wall. The primary vortex has a clockwise circulation. The vortex on the left bottom corner has a clockwise flow circulation while the top right vortex has an anticlockwise circulation. Similar flow patterns exists in literature when three vortices were observed, see Esfe et al. [55]. Increasing the thermophoresis parameter increases the circulation pattern for the top right vortex and decreases the flow patterns for the bottom left vortex. Thus the top right vortex gains strength while the bottom left vortex becomes weak.

Figure 4.2(b) shows how the isotherm pattern changes with the thermophoresis parameter. It can be seen that isotherms are distributed throughout the cavity, although with greater concentration at the four corners near the vertical walls. Similar results for streamlines and isotherms have been obtained by Sheremet [30], Sivasankaran and Pan [36], Sivasankaran and Bhuvanerwari [41], Dend and Chang [42], and Wu et al. [43]. In Figure 4.2(c) the isoconcentration patterns for changing values of the thermophoresis parameter are illustrated. The isoconcentration curves are mainly concentrated along the middle from the left top corner to the bottom right corner with and less so along the bottom left and

upper right corners of the cavity. The two corner vortices are caused by heating from the sinusoidally varying temperature. The fluid concentration is observed to be pushed to the right vertical wall when the thermophoresis parameter increases. Similar results were obtained by Mondal and Sibanda [35] and Kefayati [32].
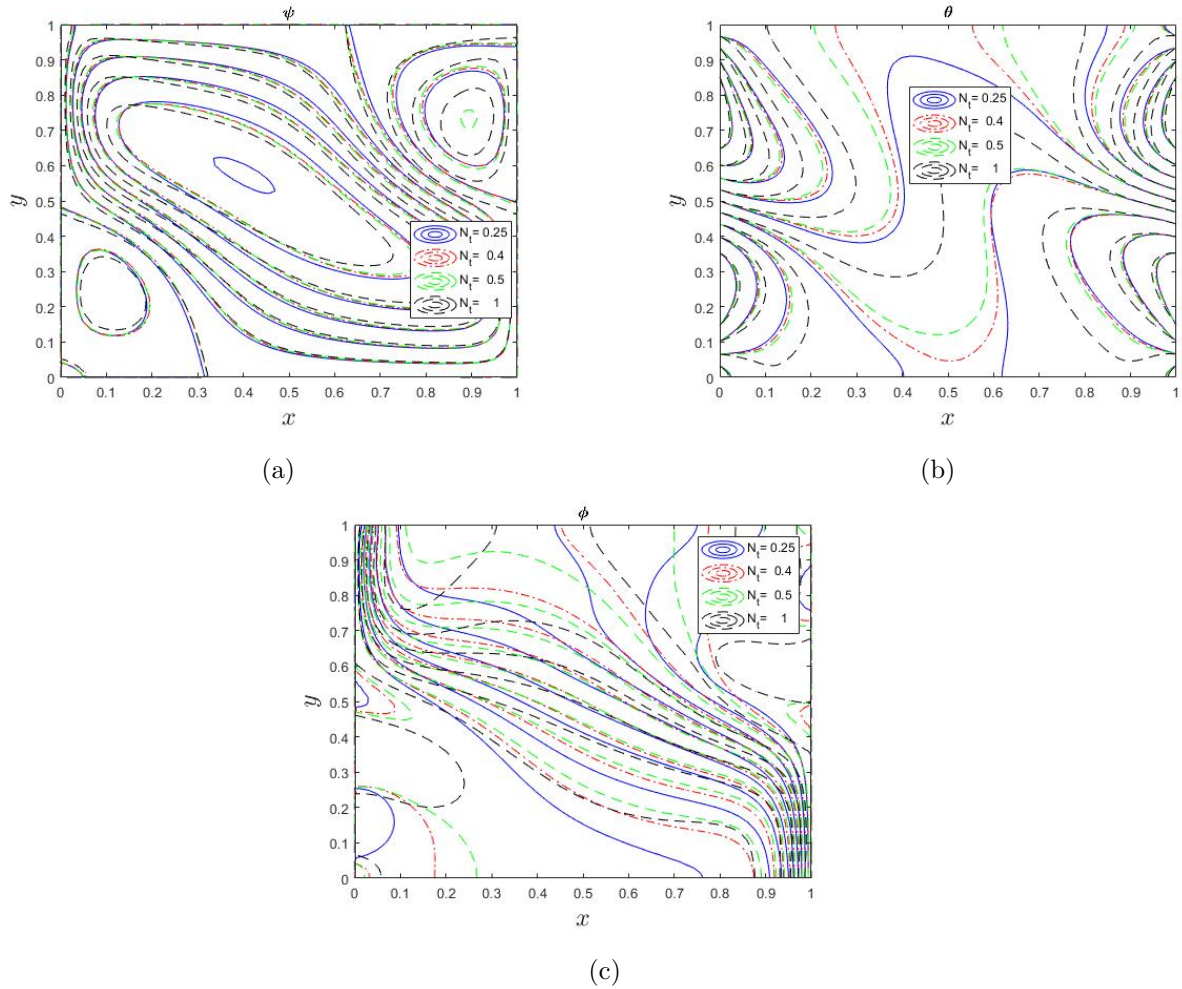

(a)

(b)

(c)

Figure 4.2: The effect of thermophoresis parameter on (a) streamlines, (b) isotherms and (c) isoconcentrations

Figure 4.3 shows the effect of increasing the chemical reaction parameter on streamlines, isotherms and isoconcentration. Figure 4.3(a) shows how the streamlines are affected by changes in the value of the chemical reaction parameter. Increasing the chemical parameter moves the primary, the top right and the bottom left vortices to the right; with a marginal increases in flow circulation in the bottom left vortex, and a marginal decrease in flow circulation in top right vortex. Thus increasing the reaction increases the velocity of the flow. Figure 4.2(b) shows isotherms are affected by the increase in chemical reaction parameter. We note that increasing the chemical reaction parameter has little impact on the isotherms. Figure 4.3(c) shows that increasing the thermophoresis parameter has the effect pushing the isoconcentration pattern towards the right vertical wall. An increase in the parameter increases the concentration.
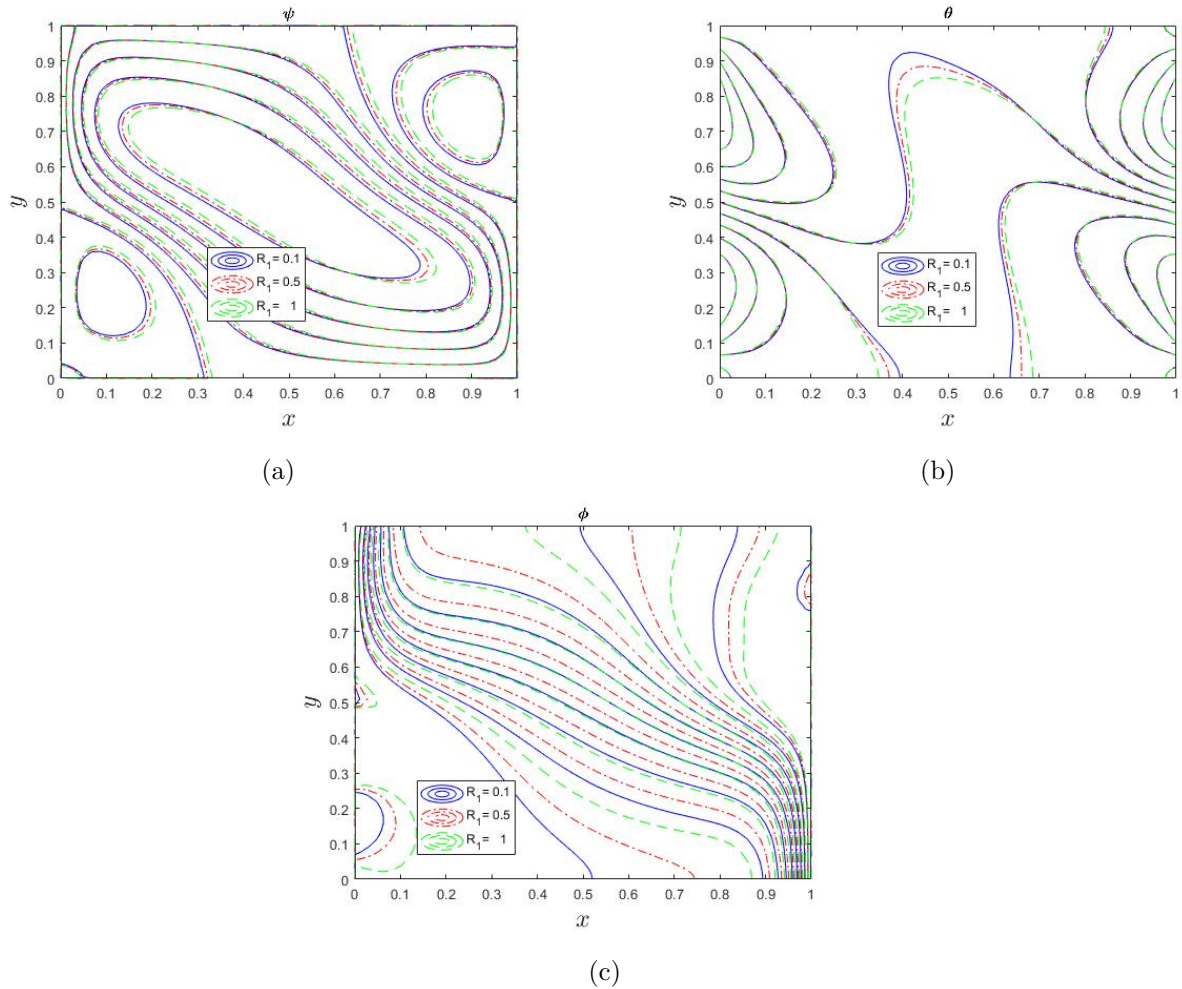
(a)

(b)

(c)

Figure 4.3: The effect of changes in the chemical reaction parameter on (a) streamlines, (b) isotherms and (c) isoconcentrations

Figure 4.4 illustrates the streamline pattern, isotherms and isoconcentration changes with the Hartmann number. Figure 4.4(a) shows changes in streamlines with changes in the Hartmann number. The increase in Hartmann number may be due to an increase in magnetic field strength or a decrease in fluid viscosity. The increase in the Hartmann number reduces the primary vortex while increasing the other two vortices. The increase in the Hartmann number eventually leads to the formation of two vortices inside the primary vortex. Figure 4.4(b) shows the change in isotherm patterns with changes in the Hartmann number. Increasing the Hartmann number increased the fluid temperature. Figure 4.4(c) shows the changes in isoconcentration pattern with changes in the Hartmann number. The increase in the Hartmann number leads to an even distribution of the isoconcentrations.

(a) streamlines

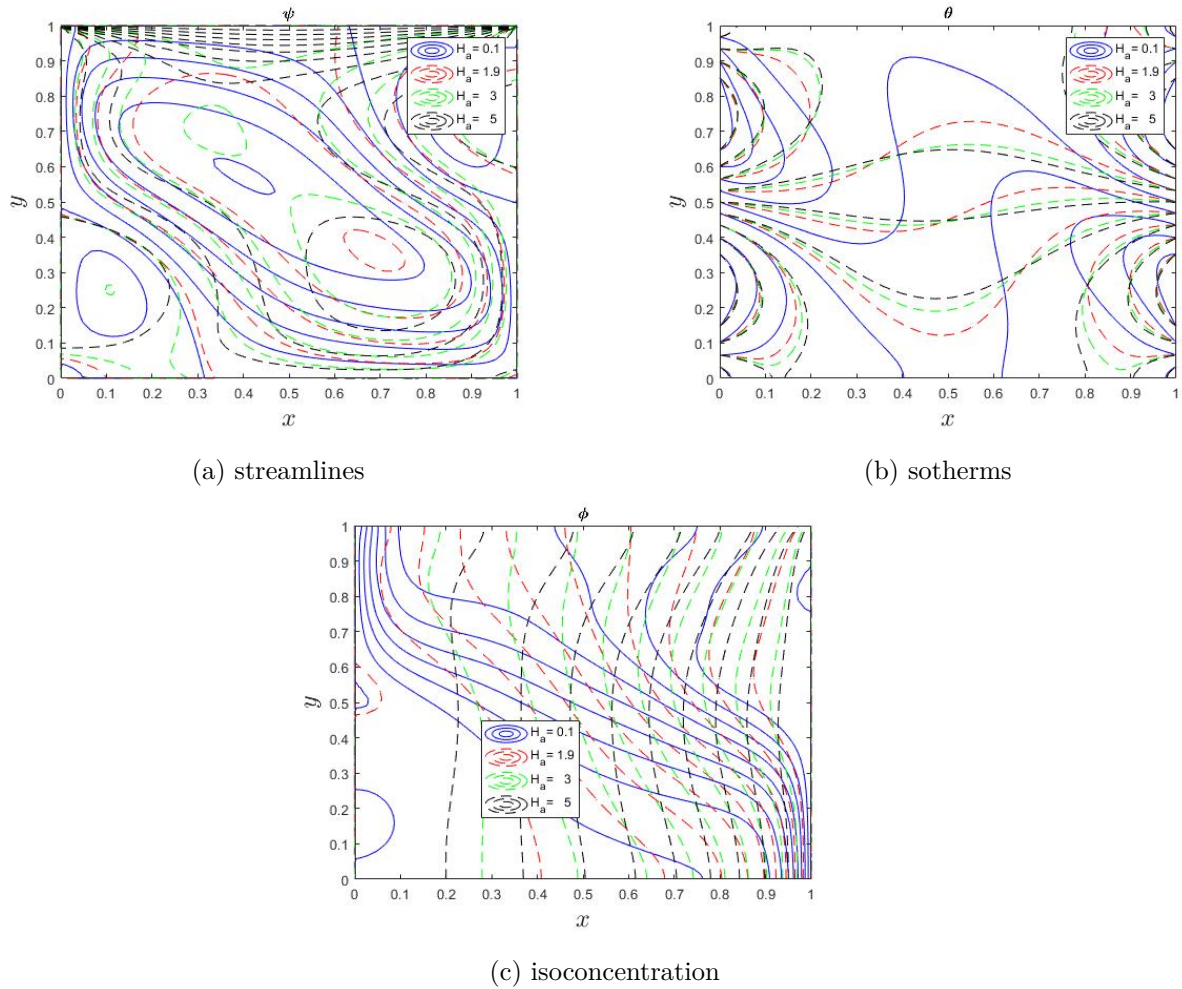(b) sotherms

(c) isoconcentration

Figure 4.4: The effect of changes in the Hartmann number on streamlines, isotherms and isoconcentrations

Figure 4.5 shows the local Nusselt number on the right vertical wall with changes in (a) the thermophoresis parameter and (b) the Hartmann number. It can be seen that the local Nusselt number varies sinusoidally with the temperature applied at the wall. A similar behaviour has been observed in Wang et al. [31], Kefayati [32], Mejri et al. [38], Elshehabey and Ahmed [58]. The increase in thermophoresis parameter increases the local Nusselt number throughout the right vertical wall. This leads to an increase in the temperature difference between the wall and the adjacent fluid. Increasing the Hartmann number increases the local Nusselt number on the below part of the right wall and increases it on the upper part. The temperature difference between the right wall and the fluid near the wall increases for the lower part and decreases for the upper part of the wall.
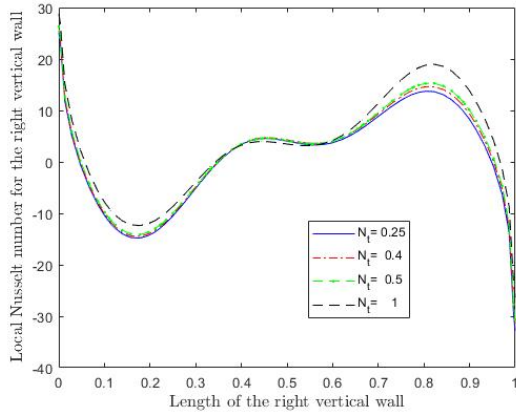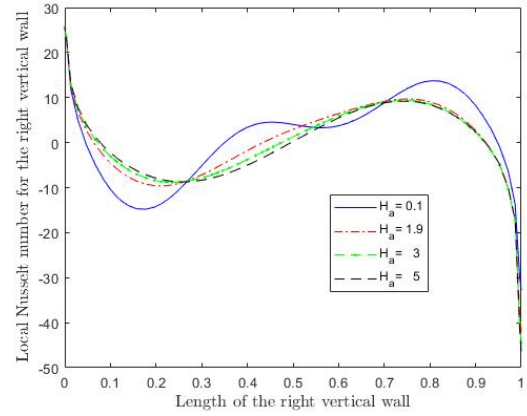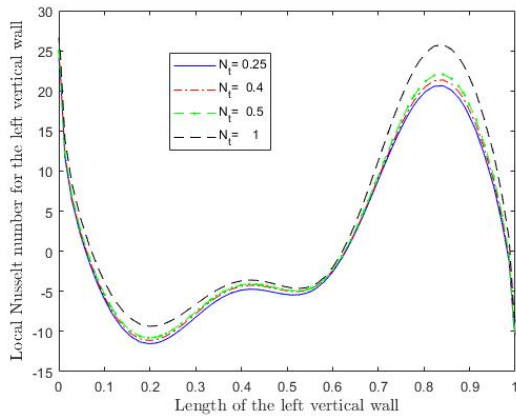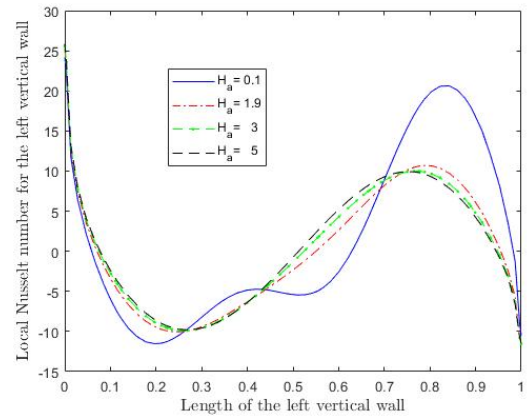
Figure 4.5: The effect of (a) the thermophoresis parameter and (b) the Hartmann number on local Nusselt number for the right vertical wall.

Figure 4.6 shows the effect of (a) the thermophoresis parameter and (b) the Hartmann number on the left side wall local Nusselt number. The local Nusselt number increases with an increase in thermophoresis parameter throughout the left side wall. The temperature difference between the wall and the adjacent fluid increases. Increasing the Hartmann number on the left side wall leads to changes in the local Nusselt number. The Nusselt number increases along the lower part of the wall and decreases on the upper part.

Figure 4.6: The effect of (a) thermophoresis parameter and (b) Hartmann number on local Nusselt number for the left vertical wall.

The local Sherwood number depending on (a) Hartmann number, (b) thermophoresis parameter, (c) Lewis number and (d) chemical reaction parameter on the left wall is illustrated in Figure 4.7. The Hartmann number increases the local Sherwood number on the below part of the left wall while increasing it on the upper part. This means the mass transfer is decreased by the Hartmann number on the left

wall. The increase in thermophoresis parameter decreases the local Sherwood number on the below part but increases the local Sherwood number on the upper part of the left side wall. The thermophoresis parameter increases the local Sherwood number on the left wall. The Lewis number increases the local Sherwood number; that is, on the below part of the left side wall mass transfer decreases, and on the upper part the mass transfer increases. The chemical reaction parameter decreases the local Sherwood number; that is, mass transfer increases on the below part of the left wall, and decreases on the top part of the left wall.
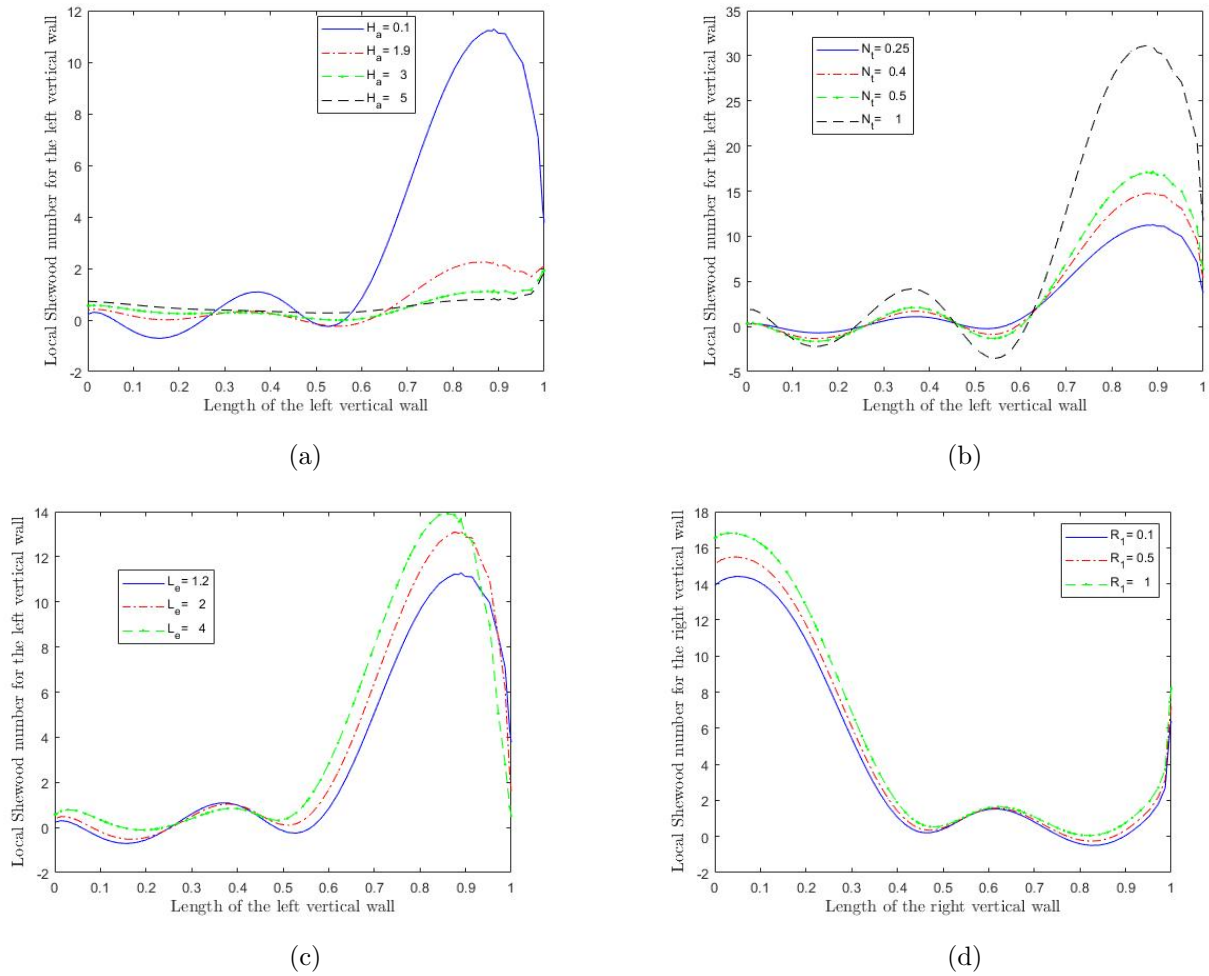
Figure 4.7: The effect of (a) the Hartmann number, (b) the thermophoresis parameter, (c) the Lewis number and (d) the chemical reaction parameter on local Sherwood number for the hot wall

4.4 Summary

A sinusoidally heated lid-driven square cavity filled with nanofluid and a horizontal moving magnetic field was investigated. The multivariate overlapping grid spectral method was used. The effects of the Hartmann number, themopheresis parameter, chemical reaction and Lewis number on streamlines, isorthems, isoconcentration, local Nusselt number and local Sherwood number were studied. The results were compared with the literature and were found to be in excellent agreement. The system produces

three circulations with the main vortex and the left bottom vortex moving in a clockwise direction with the top right vortex moving in an anticlockwise direction. Increasing the thermophoresis parameter weakens the bottom left vortex. The chemical reaction parameter moves the flow circulation to the right and gives strength to the top right vortex while decreasing the strength of left bottom vortex. Increasing the magnetic field leads to the main vortex separating into two vortices. The fluid temperature increase leads to the isoconcentration being evenly distributed. The increase in thermophoresis parameter increases the temperature difference between the wall and the fluid around it. The increase in the Lewis number increases the mass transfer on the lower part while the increase in the chemical reaction parameter increases mass transfer in the top part.

Chapter 5

Conclusion

Cavity flow problems of varying complexity and different boundary conditions were investigated. Two recent spectral methods, namely the MSQLM and MOGSQLM were used in this investigation to solve the flow equations. We compared the accuracy of the two methods on the first two problems and we used only the MOGSQLM to solve the third and last problem in Chapter 4. In Chapter 2, a square cavity flow with the left and right side walls heated and cooled, respectively, was investigated. In Chapter 3, the cavity consisted of two heated and two cooled walls. The study has shown the MOGSQLM to be more accurate, converges faster and takes less time than the MSQLM. It was found that using a large number of overlapping intervals improves the MOGSQLM in terms of accuracy, convergence and CPU time. The MSQLM and MOGSQLM solutions were compared to findings in the literature and the results were found to be in excellent agreement. In Chapter 2, increasing the Rayleigh number increased the residual and the solution errors. The circulation patterns changed from circular to elliptic and the core increased as the Rayleigh number increased. In Chapter 3, the problem gave two symmetric and counter rotating flow circulations. The fluid speed was reduced by increasing the Eckert number and increased by increasing the Brownian motion and the radiation parameter. The Brownian motion and radiation parameter increased heat and concentration while the Eckert number increased the cooling but decreased the concentration. In Chapter 4, a lid-driven cavity flow heated on both vertical walls with sinusoidal temperature was studied and the equations solved using the MOGSQLM. The cavity was filled with a nanofluid and had an applied magnetic field. It was found that the system produced three vortices, the main vortex and two smaller vortices, one on the top right corner and the other on the left bottom corner. The vortex on the left bottom corner and the main vortex were shown to move clockwise while the other vortex was found to move anticlockwise. The thermophoresis parameter was found to weaken the circulation of the bottom left vortex and increase the temperature difference between the wall and the adjacent fluid. The chemical reaction parameter pushed the flow to the right and gave strength to the top right vortex. The increase in the magnetic field led to the main vortex separating into two vortices. The local Nusselt number had a sinusoidal pattern that depended on the temperature applied at the boundaries. The Sherwood number declined with the Hartmann number while the thermophoresis parameter enhanced mass transfer.

References

[1] Trevena D.H, Cavitation and tension in liquids, Adam Hilger, Bristol, 1987.

[2] Trevena D.H, The pioneer work of François Donny on the existence of tension in liquids, Annals of Science, 1980, 37(4), 379-386.

[3] Trevena D.H, Cavitation and the generation of tension in liquids, Journal of Physics D: Applied Physics, 1984, 17(11), 2139.

[4] Franc J.P, Physics and control of cavitation, University of Grenoble, France, 2006, https://www.sto.nato.int/publications/STO%20Educational%20Notes/ RTO-EN-AVT-143/EN-AVT-143-02.pdf, accessed 11 November 2021

[5] Sreedhar B.K, Albert S.K, and Pandit A.B, Cavitation damage: Theory and measurements-A review, Wear, 2017, 372, 177-196.

[6] Binama M, Muhirwa A, and Bisengimana E, Cavitation effects in centrifugal pumps-A review, Journal of Engineering Research and Applications, 2016, 6(5), 52-63.

[7] Goqo S.P, Mondal H, Sibanda P, and Motsa S.S, A multivariate spectral quasilinearization method for entropy generation in a square cavity filled with porous medium saturated by nanofluid, Case Studies in Thermal Engineering, 2019, 14, 100415.

[8] Feldman Y, Theoretical analysis of three-dimensional bifurcated flow inside a diagonally lid-driven cavity, Theoretical and Computational Fluid dynamics, 2015, 29(4), 245-261.

[9] Shankar P.N, and Deshpande M.D, Fluid mechanics in the driven cavity, Annual Review of Fluid Mechanics, 2000, 32(1), 93-136.

[10] Giannetti F, Luchini P, and Marino L, Linear stability analysis of three-dimensional lid-driven cavity flow, In Atti del XIX Congresso AIMETA di Meccanica Teorica e Applicata, Aras Edizioni Ancona, Italy, 2009.

[11] Erturk E, Discussions on driven cavity flow, International Journal for Numerical Methods in Fluids, 2009, 60(3), 275-294.

[12] Moreau R, and Molokov S, Julius Hartmann and his followers: a review on the properties of the Hartmann layer, Magnetohydrodynamics, 2007, 80, 155-170.

[13] Cengel Y, Heat and mass transfer: fundamentals and applications, 5th Edition, McGraw-Hill Education, New York, 2015.

[14] Mahjabin S, and Alim M. A, Effect of Hartmann number on free convective flow of MHD fluid in a square cavity with a heated cone of different orientation, American Journal of Computational Mathematics, 2018, 8(04), 314.

[15] Incropera F.P, DeWitt D.P, Bergman T.L, and Lavine A.S, Fundamentals of heat and mass transfer, Wiley, Volume 6, New York, 1996.

[16] Richardson L.F, Weather prediction by numerical process, Cambridge University Press, Cambridge, 2007.

[17] White F. M, Fluid mechanics, seventh edition, McGraw-Hill, New York, 2011.

[18] Galsa A, Herein M, Lenkey L, Farkas M. P, and Taller G, Effective buoyancy ratio: a new parameter for characterizing thermo-chemical mixing in the Earth's mantle, Solid Earth, 2015, 6(1), 93-102.

[19] Aly A.M, and Mahmoud E. M, Effects of buoyancy ratio on diffusion of solid particles inside a pipe during double-diffusive flow of a nanofluid, International Journal of Numerical Methods for Heat and Fluid Flow, 2020, 31(6), 1951-1986.

[20] Hartnett J.P, and Irvine Jr, T.F, Ernst RG Eckert on the occasion of his sixtieth birthday, International Journal of Heat and Mass Transfer, 1964, 7(11), 1149.

[21] Sivasankaran S, Kandaswamy P, and Ng C.O, Double-diffusive convection of anomalous density fluids in a porous cavity, Transport in Porous Media, 2008, 71(2), 133-145.

[22] Garoosi F, Garoosi S, and Hooman K, Numerical simulation of natural convection and mixed convection of the nanofluid in a square cavity using Buongiorno model, Powder Technology, 2014, 268, 279-292.

[23] Sheremet M.A, Dinarvand S, and Pop I, Effect of thermal stratification on free convection in a square porous cavity filled with a nanofluid using Tiwari and Das' nanofluid model, Physica E: Low-Dimensional Systems and Nanostructures, 2015, 69, 332-341.

[24] Ghalambaz M, Sabour M, and Pop I, Free convection in a square cavity filled by a porous medium saturated by a nanofluid: Viscous dissipation and radiation effects, Engineering Science and Technology, an International Journal, 2016, 19(3), 1244-1253.

[25] Khadiri A, Amahmid A, Hasnaoui M, and Rtibi A, Soret effect on double-diffusive convection in a square porous cavity heated and salted from below, Numerical Heat Transfer, Part A: Applications, 2010, 57(11), 848-868.

[26] Kadri S, Mehdaoui R, and Elmir M, A vertical magneto-convection in square cavity containing a Al_2O_3+ water nanofluid: cooling of electronic compounds, Energy Procedia, 2012, 18, 724-732.

[27] Karimi-Fard M, Charrier-Mojtabi M.C, and Vafai K, Non-Darcian effects on double-diffusive convection within a porous medium, Numerical Heat Transfer, Part A: Applications, 1997, 31(8), 837-852.

[28] Bhuvaneswari M, Ganesan P.B, Sivasankaran S, and Viswanathan K.K, Effect of variable fluid properties on natural convection of nanofluids in a cavity with linearly varying wall temperature, Mathematical Problems in Engineering, 2015.

[29] Kandaswamy P, Eswaramurthi M, and Lee J, Density maximum effect on double-diffusive natural convection in a porous cavity with variable wall temperature, Transport in Porous Media, 2008, 73(2), 195-210.

[30] Sheremet M.A, Grosan T, and Pop I, Natural convection and entropy generation in a square cavity with variable temperature side walls filled with a nanofluid: Buongiorno's mathematical model, Entropy, 2017, 19(7), 337.

[31] Wang L, Huang C, Yang X, Chai Z, and Shi B, Effects of temperature-dependent properties on natural convection of power-law nanofluids in rectangular cavities with sinusoidal temperature distribution, International Journal of Heat and Mass Transfer, 2019, 128, 688-699.

[32] Kefayati G.R, Lattice Boltzmann simulation of MHD natural convection in a nanofluid-filled cavity with sinusoidal temperature distribution, Powder Technology, 2013, 243, 171-183.

[33] Sajjadi H, Delouei A.A, Mohebbi R, Izadi M, and Succi S, Natural convection heat transfer in a porous cavity with sinusoidal temperature distribution using Cu/water nanofluid: Double MRT lattice Boltzmann method, Communications in Computational Physics 2021, 29(1), 292-318.

[34] Parvin S, Nasrin R, Alim M.A, and Hossain N.F, Double-diffusive natural convective flow characteristics in a cavity, Procedia Engineering, 2013, 56, 480-488.

[35] Mondal S, and Sibanda P, Effects of buoyancy ratio on unsteady double-diffusive natural convection in a cavity filled with porous medium with non-uniform boundary conditions, International Journal of Heat and Mass Transfer, 2015, 85, 401-413.

[36] Sivasankaran S, and Pan K.L, Natural convection of nanofluids in a cavity with nonuniform temperature distributions on side walls, Numerical Heat Transfer, Part A: Applications, 2014, 65(3), 247-268.

[37] Malomar G.E, Gueye A, Mbow C, Traore V.B, and Beye A.C, Numerical study of natural convection in a square porous cavity thermally modulated on both side walls, American Journal of Engineering and Applied Sciences, 2016, 9, 591-598.

[38] Mejri I, Mahmoudi A, Abbassi M.A, and Omri A, Magnetic field effect on entropy generation in a nanofluid-filled enclosure with sinusoidal heating on both side walls, Powder Technology, 2014, 266, 340-353.

[39] Javaherdeh K, and Najjarnezami A, Lattice Boltzmann simulation of MHD natural convection in a cavity with porous media and sinusoidal temperature distribution, Applied Mathematics and Mechanics, 2018, 39(8), 1187-200.

[40] Bhuvaneswari M, Sivasankaran S, and Kim Y.J, Magnetoconvection in a square enclosure with sinusoidal temperature distributions on both side walls, Numerical Heat Transfer, Part A: Applications, 2011, 59(3), 167-184.

[41] Sivasankaran S, and Bhuvaneswari M, Natural convection in a porous cavity with sinusoidal heating on both sidewalls, Numerical Heat Transfer, Part A: Applications, 2013, 63(1), 14-30.

[42] Deng Q.H, and Chang J.J, Natural convection in a rectangular enclosure with sinusoidal temperature distributions on both side walls, Numerical Heat Transfer, Part A:Applications, 2008, 54(5), 507-524.

[43] Wu F, Zhou W and, Ma X, Natural convection in a porous rectangular enclosure with sinusoidal temperature distributions on both side walls using a thermal non-equilibrium model, International Journal of Heat and Mass Transfer, 2015, 85, 756-771.

[44] Sheremet M.A, and Pop I, Natural convection in a square porous cavity with sinusoidal temperature distributions on both side walls filled with a nanofluid: Buongiorno's mathematical model, Transport in Porous Media, 2014, 105(2), 411-429.

[45] Arani A.A, Kakoli E, and Hajialigol N, Double-diffusive natural convection of AL_2O_3-water nanofluid in an enclosure with partially active side walls using variable properties, Journal of Mechanical Science and Technology, 2014, 28(11), 4681-4691.

[46] Nik-Ghazali N, Badruddin I.A, Badarudin A, and Tabatabaeikia S, Dufour and Soret effects on square porous annulus, Advances in Mechanical Engineering, 2014, 6,209753.

[47] Botella O, and Peyret R, Benchmark spectral results on the lid-driven cavity flow., Computers and Fluids, 1998, 27(4), 421-433.

[48] Erturk E, Corke T.C, and Gökçöl C, Numerical solutions of 2D steady incompressible driven cavity flow at high Reynolds numbers, International Journal for Numerical Methods in Fluids, 2005, 48(7), 747-774.

[49] Bruneau C.H and Saad M, The 2D lid-driven cavity problem revisited, Computers and Fluids. 2006, 35(3), 326-348.

[50] Martinez J.D, and Esperança P.D, A Chebyshev collocation spectral method for numerical simulation of incompressible flow problems, Journal of the Brazilian Society of Mechanical Sciences and Engineering, 2007, 29(3), 317-328.

[51] Bognár G, and Csáti Z, Spectral method for time dependent Navier-Stokes equations, Miskolc Mathematical Notes, 2016, 17(1), 43-56.

[52] Poochinapan K, Numerical implementations for 2D lid-driven cavity flow in stream function formulation, International Scholarly Research Notices, 2012, https://doi.org/10.5402/2012/871538.

[53] Basak T, Roy S, Sharma P.K, and Pop I, Analysis of mixed convection flows within a square cavity with uniform and non-uniform heating of bottom wall, International Journal of Thermal Sciences, 2009, 48(5), 891-912.

[54] Jafari A, Rahimian M.H, and Saeedmanesh A, An unsteady mixed convection in a driven cavity filled with nanofluids using an externally oscillating lid, Journal of Electronics Cooling and Thermal Control, 2013, 3(2), 58-73.

[55] Esfe M.H, Ghadi A.Z, and Noroozi M.J, Numerical simulation of mixed convection within nanofluid-filled cavities with two adjacent moving walls, Transactions of the Canadian Society for Mechanical Engineering, 2013, 37(4), 1073-1089.

[56] Bhuvaneswari M, Sivasankaran S, and Kim Y.J, Numerical study on double-diffusive mixed convection with a Soret effect in a two-sided lid-driven cavity, Numerical Heat Transfer, Part A: Applications, 2011, 59(7), 543-560.

[57] Nithyadevi N, and Yang R.J, Double-diffusive natural convection in a partially heated enclosure with Soret and Dufour effects, International Journal of Heat and Fluid Flow, 2009, 30(5), 902-910.

[58] Elshehabey H.M, and Ahmed S.E, MHD mixed convection in a lid-driven cavity filled by a nanofluid with sinusoidal temperature distribution on the both vertical walls using Buongiorno's nanofluid model, International Journal of Heat and Mass Transfer, 2015, 88, 181-202.

[59] Ducasse D. S, and Sibanda P, On mixed convection in a cavity with sinusoidally heated moving lid and uniformly heated and cooled side walls, Boundary Value Problems, 2013, 83 (2013), https://doi.org/10.1186/1687-2770-2013-83.

[60] Aydin O, and Yang W.J, Mixed convection in cavities with a locally heated lower wall and moving sidewalls, Numerical Heat Transfer, Part A, Applications, 2000, 37(7), 695 - 710.

[61] Guo G, and Sharif M. A, Mixed convection in rectangular cavities at various aspect ratios with moving isothermal sidewalls and constant flux heat source on the bottom wall, International Journal of Thermal Sciences, 2004, 43(5), 465-475.

[62] Ducasse D.S, Analysis of mixed convection in an air filled square cavity, MSc Dissertation, University of KwaZulu-Natal, 2010.

[63] Mohammad U.H.J, Washim A, and Azharul K, Heat and Mass Transfer Modelling During Drying: Empirical to Multiscale Approaches, first Edition, Engineering and Technology, Food Science and Technology, Boca Raton, 2021.

[64] Murmura M.A, Cerbelli S, Annesini M.C, and Sheintuch M, Derivation of an enhanced Sherwood number accounting for reaction rate in membrane reactors, Steam reforming of methane as case study, Catalysis Today, 2021, 364, 285-293.

[65] Lienhard J.H.IV, and Lienhard J.H.V, A heat transfer textbook, Third edition, Phlogiston Press, Cambridge, 2005.

[66] Cengel Y, Heat and mass transfer a practical approach, second edition, McGraw-Hill, New York, 2003.

[67] Motsa S.S, Magagula V.M, and Sibanda P, A bivariate Chebyshev spectral collocation quasilinearization method for nonlinear evolution parabolic equations, The Scientific World Journal, 2014, https://doi.org/10.1155/2014/581987.

[68] Dlamini P.G, On spectral relaxation and compact finite difference schemes for ordinary and partial differential equations, Ph.D, thesis, University of Johannesburg, 2014.

[69] Lawson S. J, Barakos G. N, and Simpson A, Understanding cavity flows using proper orthogonal decomposition and signal processing, Journal of Algorithms and Computational Technology, 2010, 4(1), 47-69.

[70] Brezinski C, and Wuytack L(Editors), Numerical Analysis: historical developments in the 20th century, North–Holland, Amsterdam, 2001, 1-40.

[71] Laplace P, and Courant R, The finite difference method, `chrome-extension://efaidnbmnnnibpcajpcglclefindmkaj/viewer.html?pdfurl=http%3A%2F%2Fisoz.eu%2Fteaching%2Fmats%2FMCHI%2FsemSODRIII%2FFDM_TEXT.pdf&clen=350153&chunk=true`, accessed 11 November 2021.

[72] Li Z, Finite difference methods basics, Center for Research in Scientific Computation and Department of Mathematics, North Carolina State University. 2009. `chrome-extension://efaidnbmnnnibpcajpcglclefindmkaj/viewer.html?pdfurl=http%3A%2F%2Fcdn.worldcolleges.info%2Fsites%2Fdefault%2Ffiles%2Fenggnotes%2Fnotes1.pdf&clen=178533&chunk=true`, accessed 11 November 2021.

[73] Wang S, and Lin Y, A finite-difference solution to an inverse problem for determining a control function in a parabolic partial differential equation, Inverse Problems, 1989, 5(4), 631.

[74] Tayakout M, Bernauer B, Touré Y, and Sanchez J, Modelling and simulation of a catalytic membrane reactor, Simulation Practice and Theory, 1995, 2(4-5), 205-219.

[75] Singer I, and Turkel E, High-order finite difference methods for the Helmholtz equation, Computer Methods in Applied Mechanics and Engineering, 1998, 163(1-4), 343-358.

[76] Kalis H, Efficient finite-difference scheme for solving some heat transfer problems with convection in multilayer media, International Journal of Heat and Mass Transfer, 2000,

43(24), 4467-4474.

[77] Yuste S.B, and Acedo L, An explicit finite difference method and a new von Neumann-type stability analysis for fractional diffusion equations, Society for Industrial and Applied Mathematics Journal on Numerical Analysis, 2005, 42(5), 1862-1874.

[78] Meerschaert M.M, and Tadjeran C, Finite difference approximations for two-sided space-fractional partial differential equations, Applied Numerical Mathematics, 2006, 56(1), 80-90.

[79] Martino L.A, Osella A, Dorso C, and Lanata J.L, Fisher equation for anisotropic diffusion: Simulating South American human dispersals, Physical Review E, 2007, 76(3), 031923.

[80] Chen C.M, Liu F, and Burrage K, Finite difference methods and a Fourier analysis for the fractional reaction–subdiffusion equation, Applied Mathematics and Computation, 2008, 198(2), 754-769.

[81] Zhuang P, Liu F, Anh V, and Turner I, New solution and analytical techniques of the implicit numerical method for the anomalous subdiffusion equation, Society for Industrial and Applied Mathematics Journal on Numerical Analysis, 2008, 46(2), 1079-1095.

[82] Cui M, Compact finite difference method for the fractional diffusion equation, Journal of Computational Physics, 2009, 228(20), 7792-804.

[83] Wong Y.S, and Li G, Exact finite difference schemes for solving Helmholtz equation at any wavenumber, International Journal of Numerical Analysis and Modeling, Series B, 2011, 2(1), 91-108.

[84] Hickson R.I, Barry S.I, Mercer G.N, and Sidhu H.S, Finite difference schemes for multilayer diffusion, Mathematical and Computer Modelling, 2011, 54(1-2), 210-220.

[85] Sweilam N.H, Khader M.M, and Nagy A.M, Numerical solution of two-sided space-fractional wave equation using finite difference method, Journal of Computational and Applied Mathematics, 2011, 235(8), 2832-2841.

[86] Sousa E, A second order explicit finite difference method for the fractional advection diffusion equation, Computers and Mathematics with Applications, 2012, 64(10), 3141-3152.

[87] Nowamooz H, Nikoosokhan S, Lin J, and Chazallon C, Finite difference modeling of heat distribution in multilayer soils with time-spatial hydrothermal properties, Renewable Energy, 2015, 76, 7-15.

[88] Wang H, Shi B, Liang H, and Chai Z, Finite-difference lattice Boltzmann model for nonlinear convection-diffusion equations, Applied Mathematics and Computation, 2017, 309, 334-349.

[89] De Weck O, and Kim I.Y, Finite element method, Massachusetts Institute of Technology, Engineering Design and Rapid Prototyping, 2004, https://stuff.mit.edu/afs/athena.mit.edu/course/16/16.810/www/16.810_L4_CAE.pdf , accessed 11 November 2021.

[90] Nikishkov G. P, Introduction to the finite element method, University of Aizu, 2009,

`chrome-extension://efaidnbmnnnibpcajpcglclefindmkaj/viewer.html?pdfurl=`
`http%3A%2F%2Fnliebeaux.free.fr%2Fressources%2Fintrofem.pdf&clen=216754&`
`chunk=true`, accessed 11 November 2021.

[91] Goldstein C.I, A finite element method for solving Helmholtz type equations in waveguides and other unbounded domains, Mathematics of Computation, 1982, 39(160), 309-324.

[92] Ludwig R, and Lord W, A finite-element formulation for the study of ultrasonic NDT systems, IEEE Transactions on Ultrasonics, Ferroelectrics, and Frequency Control, 1988, 35(6), 809-820.

[93] Hiltunen K, A stabilized finite element method for particulate two-phase flow equations laminar isothermal flow, Computer Methods in Applied Mechanics and Engineering, 1997, 147(3-4), 387-399.

[94] Chowdhury S.R, and Narasimhan R, A cohesive finite element formulation for modelling fracture and delamination in solids, Sadhana, 2000, 25(6), 561-587.

[95] Tezduyar T.E, Finite element methods for flow problems with moving boundaries and interfaces, Archives of Computational Methods in Engineering, 2001, 8(2), 83-130.

[96] Boncut M, Finite element approximation of the Navier-Stokes equation, General Mathematics, 2004, 12(2), 61-68.

[97] Nagrath S, Jansen K.E, and Lahey Jr R.T, Computation of incompressible bubble dynamics with a stabilized finite element level set method, Computer Methods in Applied Mechanics and Engineering, 2005, 194(42-44), 4565-4587.

[98] Marchandise E, and Remacle J.F, A stabilized finite element method using a discontinuous level set approach for solving two phase incompressible flows, Journal of Computational Physics, 2006, 219(2), 780-800.

[99] Ammar K, Appolaire B, Cailletaud G, Feyel F, and Forest S, Finite element formulation of a phase field model based on the concept of generalized stresses, Computational Materials Science, 2009, 45(3), 800-805.

[100] Mantari J.L, and Canales F.G, Finite element formulation of laminated beams with capability to model the thickness expansion, Composites Part B: Engineering, 2016, 101, 107-115.

[101] Roy S, Juha M, Shephar, M.S, and Maniatty A.M, Heat transfer model and finite element formulation for simulation of selective laser melting, Computational Mechanics, 2018, 62(3), 273-284.

[102] Canuto C, Hussaini M.Y, Quarteroni A and Zang T.A, Spectral methods: fundamentals in single domains, Springer Science and Business Media, New York, 2007.

[103] Canuto C, Hussaini M.Y, Quarteroni A, and Thomas J, A, Spectral methods in fluid dy-

namics. Springer Science and Business Media, Springer Series in Computational Physics, Springer-Verlag, Berlin, 2012, https://doi.org/10.1155/2015/391786.

[104] Motsa S.S, Dlamini P.G, and Khumalo M, Spectral relaxation method and spectral quasi-linearization method for solving unsteady boundary-layer flow problems, Advances in Mathematical Physics. 2014, https://doi.org/10.1155/2014/341964.

[105] RamReddy C, Pradeepa T, and Srinivasacharya D, Numerical study of mixed convection flow of a micropolar fluid towards permeable vertical plate with convective boundary condition, Journal of Applied Analysis and Computation, 2015, 6(2), 254-270.

[106] Muzara H, Shateyi S, and Marewo G.T, Spectral quasilinearization method for solving the Bratu problem, Advances and Applications in Fluid Mechanics, 2018, 21(4), 449-463.

[107] Mondal H, and Sibanda P, Spectral quasilinearization method for entropy generation using the Cattaneo–Christov heat flux model, International Journal of Computational Methods, 2020, 17(5), 1940002.

[108] Alharbey R.A, Mondal H, and Behl R, Spectral quasilinearization method for non-darcy porous medium with convective boundary condition, Entropy, 2019, 21(9), 838.

[109] Ibrahim W, Spectral quasilinearization method for solution of convective heating condition, Engineering Transactions, 2020, 68(1), 69-87.

[110] Oyelakin I.S, Mondal S, and Sibanda P, Unsteady mixed convection in nanofluid flow through a porous medium with thermal radiation using the Bivariate Spectral Quasilinearization method. Journal of Nanofluids, Journal of Nanofluids, 2017, 6(2), 273-281.

[111] Muzara H, Shateyi S, and Marewo G.T, On the bivariate spectral quasilinearization method for solving the two-dimensional Bratu problem, Open Physics, 2018, 16(1), 554-562.

[112] Goqo S.P, Oloniiju S.D, Mondal H, Sibanda P, and Motsa S.S, Entropy generation in MHD radiative viscous nanofluid flow over a porous wedge using the bivariate spectral quasilinearization method, Case Studies in Thermal Engineering, 2018, 12, 774-788.

[113] Goqo S.P, Mondal S, Sibanda P, and Motsa S.S, Efficient multi-domain bivariate spectral collocation solution for MHD laminar natural convection flow from a vertical permeable flat plate with uniform surface temperature and thermal radiation, International Journal of Computational Methods, 2019, 16(6), 1840029.

[114] Magagula V.M, Motsa S.S, and Sibanda P, On the bivariate spectral quasilinearization method for nonlinear boundary-layer partial differential equations, In Applications of Heat, Mass and Fluid Boundary-Layers, 2020, 177-190. Woodhead Publishing.

[115] Magagula V.M, Motsa S.S, and Sibanda P, A multi-domain bivariate pseudospectral method for evolution equations, International Journal of Computational Methods, 2017, 14(04), 1750041.

[116] Oyelakin I.S, Mondal S, and Sibanda P, A multi-domain spectral method for non-Darcian mixed convection flow in a power-law fluid with viscous dissipation, Physics and Chemistry of Liquids, 2018, 56(6), 771-789.

[117] Goqo S.P, Mondal S, Sibanda P, and Motsa S.S, Efficient multi-domain bivariate spectral collocation solution for MHD laminar natural convection flow from a vertical permeable flat plate with uniform surface temperature and thermal radiation, International Journal of Computational Methods, 2019, 16(6), 1840029.

[118] Oyelakin I.S, Mondal S, Sibanda P, and Motsa S.S, A multi-domain bivariate approach for mixed convection in a Casson nanofluid with heat generation, Walailak Journal of Science and Technology, 2019, 16(9), 681-699.

[119] Ayano M.S, Otegbeye O, and Goqo S.P, Natural convection MHD radiative flow on a sphere through porous medium considering Ohmic dissipation, International Journal of Heat and Technology, 2019, 37(4), 999-1008.

[120] Samuel F.M, and Motsa S.S, Solving hyperbolic partial differential equations using a highly accurate multidomain bivariate spectral collocation method, Wave Motion, 2019, 8, 57-72.

[121] Dlamini P.G, and Magagula V.M, A multivariate spectral quasilinearization method for the solution of (2+ 1) dimensional Burgers' equations, International Journal of Nonlinear Sciences and Numerical Simulation, 2020, 21(7-8), 683-91.

[122] Mkhwatshwa, M.P, Overlapping grid spectral collocation method for nonlinear differential equations modelling fluid flow problems, PhD Dissertation, University of KwaZulu-Natal, 2020.

[123] Mkhatshwa M.P, Motsa S, and Sibanda P, Overlapping multi-domain bivariate spectral method for systems of nonlinear PDEs with fluid mechanics applications, In Advances in Fluid Dynamics, 2021, 685-699. Springer, Singapore.

[124] Mkhatshwa M.P, Motsa S.S, and Sibanda P, Overlapping multi-domain bivariate spectral method for conjugate problems of conduction and MHD free convection flow of nanofluids over flat plates, Mathematical and Computational Applications, 2021, 18(5), https://doi.org/10.1142/S0219876221500043.

[125] Mkhwatshwa M.P, Motsa S.S, Ayona M.S, and Sibanda P, MHD mixed convective nanofluid flow about a vertical slender cylinder using overlapping multi-domain spectral collocation approach, Case Studies in Thermal Engineering, 2020, https://doi.org/10.1016/j.csite.2020.100598.

[126] Mkhatshwa M.P, Motsa S.S, and Sibanda P, Overlapping multi-domain spectral method for MHD mixed convection slip flow over an exponentially decreasing mainstream with nonuniform heat source/sink and convective boundary conditions, International Journal of Computational Methods, 20, https://doi.org/10.1142/S0219876221500043.

[127] Mkhatshwa M.P, Motsa S.S, and Sibanda P, Numerical solution of time-dependent Emden-Fowler equations using bivariate spectral collocation method on overlapping grids, Nonlinear Engineering, 2020, 9(1), 299-318.

[128] Mkhatshwa M.P, Motsa S.S, and Sibanda P, MHD mixed convective radiative flow of Eyring-Powell fluid over an oscillatory stretching sheet using bivariate spectral method on overlapping grids, Heat Transfer, 2021, 50(1), 655-687.

[129] Mkhatshwa M.P, Motsa S.S, and Sibanda P, MHD bioconvective radiative flow of chemically reactive Casson nanofluid from a vertical surface with variable transport properties, International Journal of Ambient Energy, 2020, 1-9.

[130] Samuel F.M, Computation and numerical analysis of differential equations using dpectral based collocation methods, PhD thesis, University of KwaZulu-Natal, 2019.

[131] Samuel F.M, and Motsa S.S, A highly accurate trivariate spectral collocation method of solution for two-dimensional nonlinear initial-boundary value problems, Applied Mathematics and Computation, 2019, 360, 221-235.

[132] Samuel F.M, and Motsa S.S, Highly accurate overlapping grids based spectral collocation method of solution for boundary-layer equations, Applied Mathematics and Computation, 2019, 360, 221-235.

[133] Mburu Z.M, Mondal S, and Sibanda P, Numerical study on combined thermal radiation and magnetic field effects on entropy generation in unsteady fluid flow past an inclined cylinder, Journal of Computational Design and Engineering, 2021, 8(1), 149-169.

[134] Mburu Z.M, Mondal S, Sibanda P, and Sharma R, A numerical study of entropy generation on Oldroyd-B nanofluid flow past a riga plate, Journal of Thermal Engineering, 2021, 7(4), 845-866.